T-3840

EFFECT OF TEMPERING CONDITIONS ON THE FATIGUE AND TOUGHNESS OF 5160H STEEL

BY
NELSON MERLANO GAITAN

T-3840

A Thesis submitted to the Faculty and Board of Trustees of the Colorado School of Mines in partial fulfillment of the requirements for a degree of Master of Science, Metallurgical Engineering.

Signed: ______________________
Nelson Merano Gaitan

Golden, Colorado
Date: Nov/13/89

Approved: ______________________
David K. Matlock
Thesis Advisor

____
John J. Moore
Department Head

Golden, Colorado
Date: Nov/15/89

ABSTRACT

The influence of heat treatment conditions and residual alloy content on the fatigue and toughness of 5160H steel has been studied. Two steels with compositions within the specification for 5160H steel, but with two different levels of residual alloying elements were tempered at temperatures between 200°C and 600°C; two post-tempering cooling rates, water quenching and air cooling, were used. The susceptibility of thin sections of 5160H steel to temper embrittlement and its effect on the fatigue endurance limit, impact toughness, and fracture toughness were evaluated.

For all tempering temperatures except 500°C, the fatigue endurance limit of the material are not significantly affected by tempering temperature, post-tempering cooling rate, and residual alloy content. At 500°C the endurance limit is significantly reduced in both the low- and the high-residual material. The endurance limit is lower for the high-residual material, and further decreased by air cooling after tempering.

The effect of loading rate on fracture behavior were evaluated by compering Charpy V-notch impact data with data obtained on standard compact tension samples. The toughness, as measured with the compact tension sample, continuously increases with an increase in tempering temperature and was independent of post-tempering cooling rate. In contrast, the impact data were independent of post-tempering cooling rate but depended sensitively on residual alloy content. With an increase in residual alloy content the transition temperature increased, the upper shelf energy decreased, and the room-temperature impact energy was significantly reduced at tempering temperatures of 304°C and 500°C. This reduction of impact toughness indicates embrittlement by temper martensite and by temper embrittling mechanisms. The results were correlated with analysis of fracture surfaces.

Based on an analysis of the fatigue and fracture data several suggestions to optimize the behavior of 5160H steel were discussed.

TABLE OF CONTENTS

(Continued)

LIST OF FIGURES

(Continued)

Page.

(Continued)

(Continued)

(Continued)

LIST OF TABLES

ACKNOWLEDGMENTS

I wish to acknowledge the INSTITUTO COLOMBIANO DEL PETROLEO in Bucaramanga; Colombia, and the ADVANCED STEEL PROCESSING AND PRODUCTS RESEARCH CENTER for providing financial support during the development of my Masters of science program, and to STELCO INC. for providing the steels for this investigation.

I wish to thank Professors G. Krauss and S. Thomson for their assistance and instruction as members of Thesis-committee, and to students and personnel of the Metallurgical department for their friendship.

In particular I want to thank Proffesor D. K. Matlock, my thesis advisor, for his teaching and guidance during the development of my graduate program.

Finally, I wish to thank my parents, and to Victor D. and Sonia for their support.

1 INTRODUCTION

1.1 General Background

The service life of spring steels is, in general, limited by a combination of fatigue and fracture properties and reflects complex interactions of surface finish, environmental interactions, and base steel properties. Steels with the same chemical composition may have different properties and metallurgical characteristics, thus having different performance. Those mechanical properties and metallurgical characteristics are developed by thermomechanical processing and heat treatment schedules.

One of the main requirements for spring steel is high yield strength, required to prevent sagging during service due to the effect of plastic deformation. In addition, high yield strength is required to retard fatigue crack nucleation, which during the first stage of fatigue is controlled by the resistance of surfacegrains to plastic deformation.

In quenched steels, tempering is used to obtain the required balance between yield strength and toughness. However, tempering may cause various embrittlement phenomena including: Tempered Martensite Embrittlement

(TME) after tempering at around 350°C, and Temper Embrittlement (TE) after tempering at temperatures above 425°C (1). In this project only temper embrittlement will be considered. Medium- and high-carbon steels containing alloy elements such as manganese, chromium, and nickel as well as residual elements such as phosphorus, arsenic, tin and antimony are susceptible to TE (2, 3, 4, 5, 6). One steel which may be susceptible to TE is the low-alloy chromium steel 5160H (7), which is considered in this thesis.

In quenched and tempered steels, as the tempering temperature increases the yield strength at first increases and then decreases, and thus reducing the fatigue limit. During the production of leaf springs in the automotive industry, 5160H steel is typically subjected to a tempering treatment in the temperature range between 425 and 500°C (797-932°F).

1.2 Purpose of the Investigation

The purpose of this study is to examine the influence of heat treatment conditions and residual alloy content on the fatigue, toughness and fracture of 5160H steel. The project determines the susceptibility of this material to temper embrittlement, and its effect on mechanical properties. Experiments to evaluate the properties and microstructure of the material include: high cycle fatigue, impact toughness, fracture toughness, light microscopy, and electron microscopy.

1.3 Temper Embrittlement

Temper embrittlement is an embrittlement phenomena which reduces impact toughness of steels (1). This embrittlement is caused by segregation of impurity elements during the tempering process (1). Microstructural changes are dictated by the heat treatment conditions and by the compositional characteristics of the material (1-10). In this section the effect of alloy content and heat treatment on mechanical properties, with emphasis on temper induced embrittlement, are reviewed to provide a basis for the heat treatment study of this thesis.

This review on temper embrittlement is divided into two parts: the first part is a description of the main features of temper embrittlement phenomena; the second part reviews the development of the present state of understanding of the problem. Precipitation of carbides and cosegregation of impurity solute atoms and alloying elements are thought to be at the root of this embrittling phenomenon. Precipitation and segregation in temper embrittlement will be discussed in a separate section in this review.

1.3.1 General aspects. Temper embrittlement can occur during tempering at temperatures between 375 to 575°C (707 - 1070 F), on slow cooling through this temperature range, or on reheating to around 500°C (932°F). In the latter case, embrittlement is independent of post-tempering cooling rate (2). The amount of embrittlement, however, has been shown to increase with holding time at the embrittling temperature (1, 2).

Figure 1.1 shows isothermal curves of embrittlement, plotted as a function of time and embrittling temperature. The time and temperature dependence of TE can be described by a "C-curve" relationship typical of precipitation type reactions (3, 10), as shown in the figure. It has been established that the temperature range at which the rate of embrittlement is maximum is between 475 (887°F) and

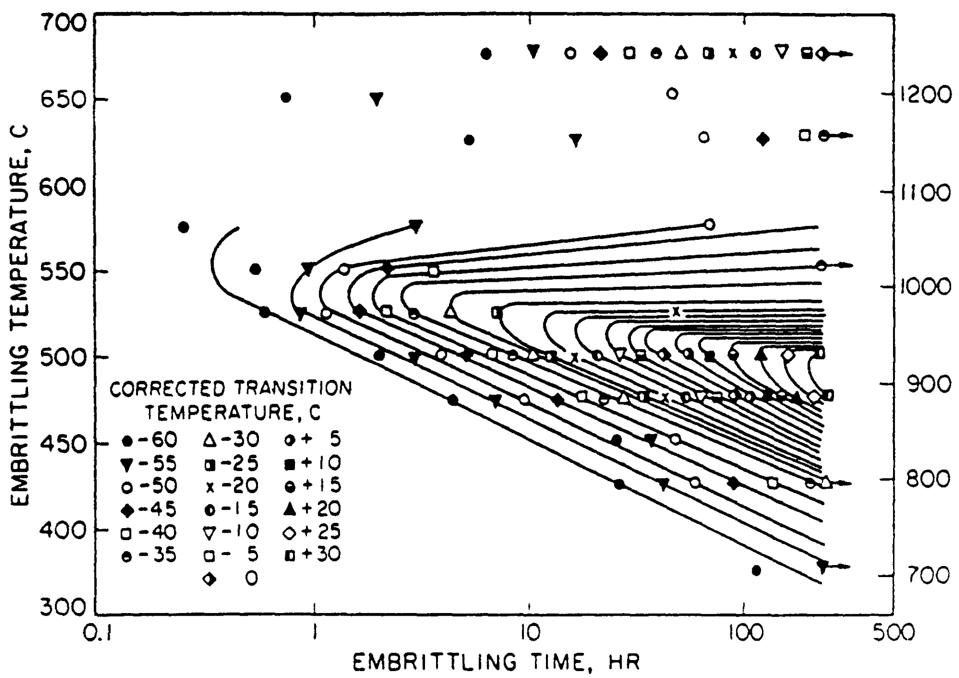

Figure 1.1 Isoembrittlement curves plotted as a function of time and temperature. Each line represents a specific transition temperature measured in a Charpy test for a Ni-Cr steel. The data cover the range, in 5°C increments, from a transition temperature of -60°C (observed for the shortes embrittling time) to one of +30°C. (Ref. 5)

550°C (1066°F). Furthermore, embrittlement at temperatures above 630°C (1166°F) is barely detectable (3, 11).

The amount of embrittlement also depends on the time at high tempering and austenitising temperature (3, 12, 13). The amount of embrittlement is reduced by prolonged tempering at temperatures above 630°C (1166°F) (3), and increased by high austenitizing temperatures (2, 12, 13). The effect of austenitizing temperature is through control of the austenite grain size; the degree of embrittlement increases with an increase in austenite grain size (12, 13).

Temper embrittlement affects a variety of mechanical properties including impact transition temperature, brittle- fracture strength, fracture toughness, room temperature tensile properties and fatigue strength. Figure 1.2 shows fracture energy as a function of test temperature for a non-embrittled (a) and for an embrittled (b) steel. Temper embrittlement is associated with a shift, to higher temperatures, of the transition curve for the embrittled condition (1, 2, 5). Figure 1.3 is a plot of room temperature Charpy impact energy versus tempering temperature in the TME range for two steels with different phosphorus content. Embrittlement of a steel is also

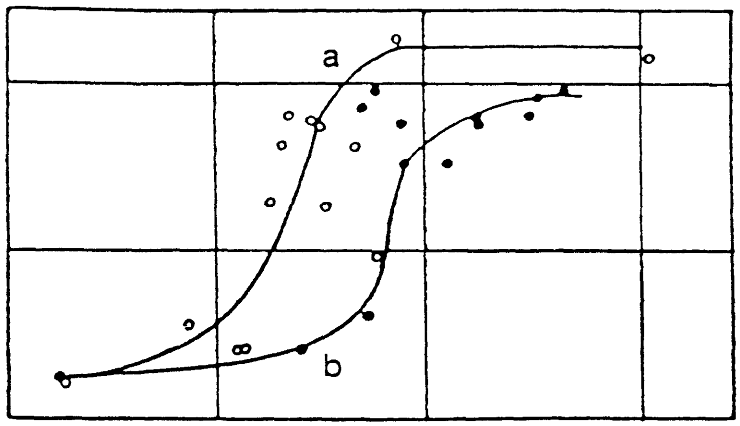

Figure 1.2 Shift in notched-bar impact energy curve due to temper embrittlement. a) non-embrittled steel, b) embrittled curve (Ref. 11).

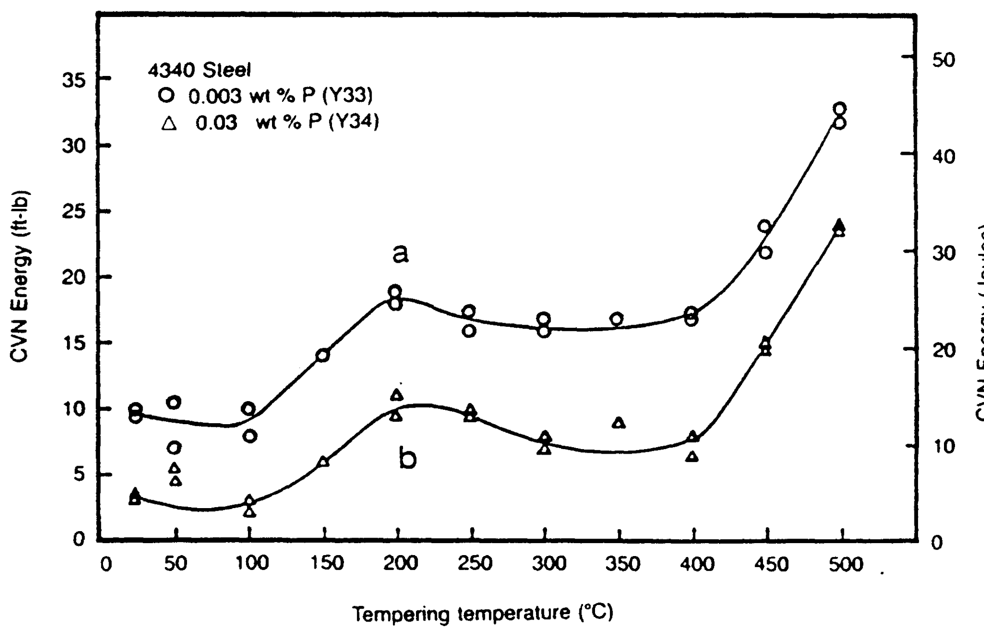

Figure 1.3 Room temperature Charpy impact energy as a function of tempering temperature in the TME range. a) low phosphorus, b) high phosphorus (Ref. 1).

characterized by a reduction of fracture energy (1, 2, 6, 10) as is shown in the figure for embrittlement after tempering at 350°C. This reduction of impact energy is larger for the steel with the larger phosphorus content.

During initial stages of TE investigations, it was believed that mechanical properties other than impact toughness were not affected by TE (10). However, subsequent investigations have proven this assumption to be wrong. For instance, results from low temperature tensile tests indicate that TE reduces the brittle-fracture strength (11). Furthermore, Key and Porr (6) and Carr (14) indicate that fracture surface analysis of samples tested in tension, at low temperature, can yield fracture-appearance-transition curves similar to those from impact samples.

Temper embrittlement also affects room temperature tensile properties and fatigue behavior (14, 15). From room temperature tensile testing, Carr et al. (14) indicated that there are measurable differences in the stress-strain curves of embrittled and non-embrittled materials. A difference in tensile flow and fracture behavior reveals a general deterioration of strength and ductility due to temper embrittlement (14). Observations by McMahon (15) on the fatigue behavior of Si-steels, indicate that fatigue properties are affected bt TE, by a reduction of the fatigue strength of the material. Fatigue crack initiation and propagation in notched-fatigue specimens are also enhanced in embrittled steels (15, 16).

Fracture appearance is an important indication of embrittlement. Intergranular brittle fracture is a characteristic feature in fracture surfaces of temper embrittled steels (1, 3, 10, 11). It was proposed (11) that intergranular fracture will be observed when, as the result of TE or another grain boundary phenomena, the intergranular fracture strength is decreased below that for cleavage fracture; thus, the temperature for brittle fracture is increased, but the flow properties themselves may remain constant. Schulz and McMahon (58) describe an "intergranular dimpled rupture" as an indication of a weak embrittlement. They attributed this type of fracture appearance to a process of void formation during brittle fracture, due to a decreased cohesion along carbide-ferrite interfaces. This decrease of cohesion is believed to be caused by the presence of embrittling elements at the interfaces. Segregation of embrittling elements will be discussed in Section 1.3.2.

The effects of TE on mechanical properties as discussed above are very dependent on composition (1, 2, 3, 10). Greaves (2) and Woodfine (3) pointed out a strong influence of chromium, manganese, and nickel, (listed in decreasing order of importance) on the susceptibility of TE in steels containing phosphorus. It is recognized that phosphorus levels as low as 0.008 % could increase temper embrittlement susceptibility (3). Low (5) indicates that in low chromium steels (< 0.6 %) high phosphorus contents (~0.1 %) do not have a strong embrittling effect, but that for higher chromium contents (> 1.5 %) even small quantities (~0.01 %) of phosphorus produce large effects. Key and Porr (6) strongly state that trace elements, such as phosphorus, are directly related to TE.

Susceptibility to temper embrittlement is considered negligible in high purity steels (15). Steven and Balajiva (4), working with high purity steels, demonstrated that major alloying elements, such as carbon, nickel, chromium, and molybdenum, are not directly responsible for TE; but traces of impurity elements like antimony, tin, phosphorus, and arsenic, (listed in decreasing order of importance) (3, 4, 15), promote embrittlement in the presence of such major alloying elements. Manganese and sulfur are also found to induce embrittlement (4). Steven and Balajiva (4) also indicate that the effect of impurity elements seems to depend on the embrittling temperature, the prior austenite grain size (4, 12), and content of major alloying elements.

Further investigations by McMahon (15) on the role of the major alloying elements mentioned previously, yield important concepts: a) the combination of chromium and nickel enhances embrittlement and, b) no embrittlement takes place in the absence of the major alloying elements. He also shows that the combination of chromium and manganese produces more embrittlement than that of chromium and nickel. Finally, Hollomon (10) indicates that steels alloyed with chromium, manganese, and nickel to produce the same hardenability exhibit the same susceptibility to TE.

Further investigations on the effect of molybdenum on TE has shown a beneficial effect of this element (2, 3, 10, 17). Addition of molybdenum reduces the susceptibility of a steel to TE (2, 10). This reduction of susceptibility to TE seems to have a maximum for additions of approximately 0.4 % (10). Qu and McMahon (17) concluded that molybdenum lowers the solubility of phosphorus in iron, and, correspondingly, molybdenum retards embrittlement caused by phosphorus as well as the embrittlement caused by antimony and tin. They also state that the effect of molybdenum seems to disappear after long periods at elevated temperatures. Other elements such as oxygen, silicon, nitrogen, aluminum, boron, titanium, and zirconium appear not to have a strong effect on embrittlement (3). Woodfine (3) states that sulfur up to a level of 0.37 % does not have an strong effect on embrittlement, contrary to what was stated previously by Steven and Balajiva (4).

Temper embrittlement phenomena has been investigated on plain carbon steels and in different types of microstructures (2, 10). Plain carbon steels, with a manganese content less than 0.6 %, are not susceptible to TE (10). It has also been shown that a specific steel, due to differences in microstructure and austenite grain size (2, 3), may exhibit different degrees of TE susceptibility under similar embrittling conditions. For example, embrittlement is most severe in tempered martensitic steels and least severe in pearlitic steels, with bainitic steels being in between (3). The effect of austenite grain size is significant only when trace elements are present (12).

Another important feature of TE is that it is a reversible embrittlement (1, 2). Reheating embrittled steels at temperatures slightly above the embrittling temperature (~550 C), restores the toughness of the material (2).

Temper embrittlement is a complex phenomena shown to be the result of segregation of alloy elements as well as of impurity elements such as phosphorus, antimony, tin or arsenic to grain boundaries and interfaces (18, 19). Temper embrittled steels are known to fracture along prior austenite grain boundaries, and the actual path of fracture has been shown to follow carbide-ferrite interfaces (18, 19, 15). The role of carbide precipitation and solute segregation in temper embrittlement is discussed in following sections.

1.3.2 Precipitation in Temper Embrittlement. It was first proposed that temper embrittlement was due to a precipitation phenomena in alpha iron mostly at prior austenite grain boundaries (10, 3). Hollomon (10) proposed that the precipitates were nitrides and, thus, that the effect of elements on TE was due to the change of nitrogen solubility in ferrite. However, no such precipitates were revealed at grain boundaries (3, 5).

Successive studies concentrated on the precipitation of cementite at prior austenite grain boundaries. This aspect became an important factor in temper embrittlement (15), since a considerable amount of thin platelets of cementite were found on intergranular fracture surfaces of embrittled steels (15); it was fairly clear that fracture had taken place along ferrite-cementite interfaces.

Restaino and McMahon (19), in order to corroborate the observation of fracture along ferrite-cementite interfaces, studied the behavior of these interfaces in the presence of an embrittling element such as antimony. Results from their investigation led them to propose a theory which suggested is that antimony segregates upon cooling to internal interfaces between ferrite and cementite, and upon heating it segregates away from these interfaces. Antimony, when present at an interface, acts as a decohesive agent in the interface, thus producing an easy path for fracture propagation. Restaino and McMahon predicted that a similar model would apply for other embrittling elements such as phosphorus, arsenic and tin, since the solubility in gamma and alpha iron is similar for these elements (19).

Restaino-and-McMahon's theory on temper embrittlement is then based on four main aspects. First, embrittling elements (Sb, P, Sn, As) segregate to ferrite-cementite interfaces and weaken these interfaces (15, 18, 19, 20). Second, due to the fact that these elements are ferrite stabilizers, thus having a lower solubility in gamma than in alpha iron, they segregate to austenite grain boundaries during austenitizing and remain there upon quenching (15, 19). Third, when tempering at temperatures above 600°C, the embrittling element goes easily into solution in ferrite, away from the prior austenite grain boundary but remaining in the vicinity of the grain boundary. Then during tempering within the embrittling range (350 to 575 C), embrittling elements mainly segregate to those ferrite-ferrite and ferrite-cementite interfaces which are in the vicinity of prior austenite grain boundaries (region where the concentration of impurity elements is highest). It is important to note that segregation of embrittling elements to ferrite-cementite interfaces is more damaging than segregation at ferrite-ferrite interfaces due to the low plasticity of cementite which favors fracture (19). The final aspect in the model is the presence of enough cementite-platelets covering a large fraction of prior austenite grain boundaries. The presence of cementite platelets has been demonstrated by several investigators by techniques such as Debye-Scherrer X-ray methods (19), Auger Electron Microprobe (18), Auger Electron Spectroscopy (20), extraction replica techniques (15) and carbide extraction by electrolysis (21).

Restaino and McMahon (19) pointed out that temper embrittlement should occur even in the absence of cementite platelets at prior austenite grain boundaries; this observation agrees with Low's findings (22), which demonstrate the possibility of embrittlement in the absence of carbon. Thus, the presence of cementite only accentuates the embrittling phenomena. The amount of embrittlement should increase with an increase of cementite present at boundaries (19).

This model, however, does not account for the effect of major alloying elements (19, 15) discussed in previous section of this review. Restaino and McMahon proposed that alloying elements may affect the diffusivity of embrittling elements in ferrite and/or gamma iron (19), affect the development of platelet-like cementite at grain boundaries (19), promote a cosegregation process of alloy and impurity elements to grain boundaries, or promote scavenging of embrittling elements (15). The role of segregation of major alloying and impurity elements in TE will be reviewed in the following section.

1.3.3 Solute Segregation in Temper Embrittlement.

Temper embrittlement was shown above to be enhanced by a precipitation reaction at prior austenite grain boundaries. However, it was also stated that temper embrittlement can occur in the absence of carbon, which suggests that TE involves some type of solute segregation to those grain boundaries, so that the characteristic intergranular fracture of temper-embrittled steels is promoted.

Since early stages of the study of TE, attention has been focused on analysis of composition and structure of prior austenite grain boundaries of embrittled steels. McMahon (15), Capus (12) and Low (5) indicated that TE mechanisms are based on a phenomena of reversible segregation of impurity elements to grain boundaries. It had to be a reversible type of segregation in order to account for the reversible nature of TE.

The first evidence of solute segregation to prior austenite grain boundaries was the preferential etching attack of those boundaries (3, 11). Since then, different models have been proposed to explain the nature of solute segregation involved in TE phenomena. An initial model, based on equilibrium segregation, has been constantly reviewed to include new observations on the complexity of the segregation behavior of solute elements at the vicinity of prior austenite grain boundaries. Major aspects of the preferential etching attack of prior austenite grain boundaries and the five models proposed to explain TE phenomena will be presented in the remainder of this section. The models include the following concepts concepts: equilibrium segregation, double segregation, non-equilibrium segregation, mixed mode segregation, and cosegregation.

The concept of the effect of grain-boundary cementite-platelets on temper embrittlement, discussed in Section 1.3.2, was first proposed in 1967. A brief discussion on a possible correlation between carbide precipitation and solute segregation will be included at the end of the section.

Preferential attack of a picric-acid solution to prior austenite grain boundaries was found to be useful to differentiate tough and embrittled steels containing phosphorus (3, 12). This preferential attack develops grooves along prior austenite grain boundaries in embrittled steels, an effect which is intensified as the amount of embrittlement present in the steel increases, or as the etching time increases (11).

Based on etching studies, Woodfine (11) first proposed that TE may be due to the segregation of solute atoms such as chromium, manganese, molybdenum, tungsten and phosphorus to austenite and ferrite grain boundaries. This segregation of atoms was believed to reduce the cohesive forces along the grain boundaries, which in turn would explain the lowering of the intergranular brittle fracture stress below that for cleavage fracture (11, 23, 24).

Before reviewing the different models proposed to explain segregation phenomena in TE, it is important to point out the main aspects which characterize the segregation of solute elements in TE. Joshi and Stein (25) analyzed the chemical composition of fracture surfaces of embrittled and unembrittled specimens with Auger electron microscopy. This technique provided a mean to study the minute quantities of solute segregation involved in TE phenomena. Their observations on chemical composition gradients at grain boundaries documented the interaction of alloying and impurity elements and role of this interaction in the problem. A brief summary of their results (25) includes: 1) Antimony (as an example of impurity elements), nickel and chromium are observed to segregate to grain boundaries. 2) Segregation of nickel and chromium does not occur in nonembrittled steels. 3) No segregation of antimony is observed in the absence of nickel or chromium, as well as no segregation of nickel or chromium in the absence of antimony. 4) Segregation of antimony and tin is limited to few atomic layers (between 5 and 20 layers), while segregation of nickel and, less evident, of chromium is observed beyond 100 atomic layers. 5) Segregation of antimony, nickel and chromium occur almost simultaneously. 6) The nickel concentration profile exhibits a "hump" in the vicinity of the grain boundary. 7) Segregation of carbon is also observed in many steels.

In the model of equilibrium segregation, solute segregation is favored by thermodynamic considerations (Gibbsian adsorption)(25). The driving force for segregation of solute atoms to grain boundaries is a reduction of the free energy of the system by reducing the energy of the grain boundaries. The misfit strain of the impurity atoms in the lattice of the solvent is also believed to favor the segregation process (23). This model, however, does not account for the effect of alloying elements (23), the interaction between impurity and alloying elements, the total amount of observed segregation, or the concentration profile of nickel (25), among others other factors. Thus, segregation in temper embrittlement is not likely to be defined by a simple mechanism like equilibrium segregation.

In a double segregation model (23), the major driving force for impurity-element segregation to prior austenite grain boundaries is a chemical interaction between the impurity elements and the alloy elements which had previously segregated to prior austenite grain boundaries during austenitizing (17). This theory accounts for the effect of alloy elements in temper embrittlement, the concentration of impurity atoms at prior austenite grain boundaries and not at ferrite grain boundaries, and based on this model the reversibility of embrittlement could be explained in terms of the difference of diffusion rates of impurity and major alloy elements. With this model, however, a high concentration of chromium at prior austenite grain boundaries would be expected even in the nonembrittled condition (23), such concentration is not observed in TE segregation as indicated previously. Furthermore, the beneficial effect of molybdenum on decreasing embrittlement is contradictory to the theory, since molybdenum is a strong segregating element and strong carbide former. Thus, based on the double segregation model, molybdenum additions would be expected to enhance embrittlement (23). A model based on nonequilibrium segregation is then proposed to account for the behavior of molybdenum.

The model of nonequilibrium segregation (25) is based on segregation due to interaction of solute elements with vacancies, dislocations, or any other type of defect which can serve as sinks for solute atoms. It is stated that steels containing molybdenum have a large dislocation density to which impurity elements segregate, thus reducing the amount of impurity elements segregating to grain boundaries and in turn reducing the amount of embrittlement. This influence of dislocation density on temper embrittlement agrees with observations by Keh and Porr (6) from their study of the effect of cold work on temper embrittlement.

Keh and Porr (6) found that cold work, after quenching and tempering, reduces susceptibility to TE. The larger the amount of cold work the less susceptible the steel becomes. Also, impact toughness of an embrittled steel can be partially restored by cold working and reannealing in the embrittling-temperature range (6). Based on these observations they proposed that cold working introduces defect-sites and dislocations which interact with solute atoms during subsequent annealing. With the nonequilibrium segregation model segregation of nickel and chromium would be expected at grain boundaries even in the absence of impurities (23), which does not agree with the characteristics of segregation in temper embrittlement described earlier.

In the combined-segregation model (25), the complex distribution of solute elements at grain boundaries is explained based on a combination of the effects of equilibrium and non-equilibrium segregation. Figure 1.4a is a representation of the solute concentration at grain a

b

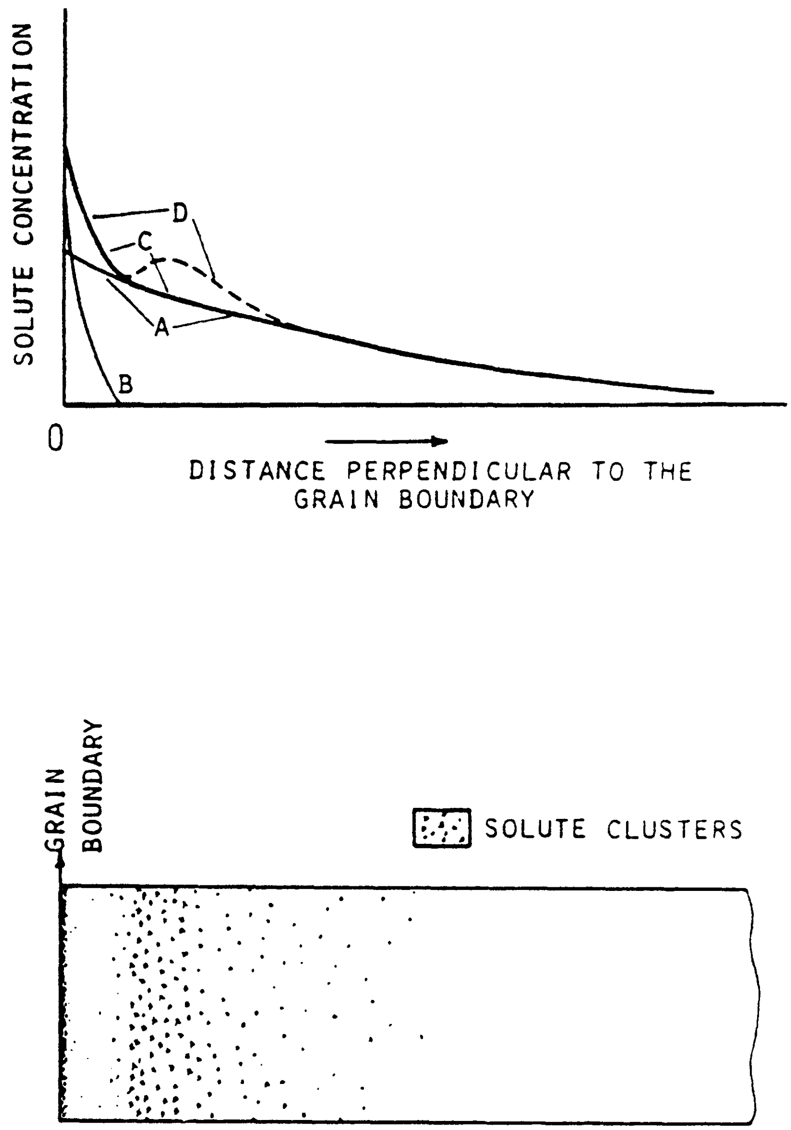

Figure 1.4 a) Composition profile which develop during segregation (The curves as identified in text). b) Schematic showing the distribution of clusters and segregation near the grain boundary (Ref. 25).

boundaries used to explain the double segregation model. In this theory a complex alloying elements-impurity-vacancy interaction is believed to explain the large distance from the boundary at which solute gradient is observed, as shown by curve A in Figure 1.4a, and the formation of stable clusters at certain distance from the boundary as shown in Figure 1.4b. The segregation at the boundary by Gibbsian adsorption is shown by curve B in Figure 1.4a. The chemical composition determined by Auger spectroscopy is shown by curve D in the same figure. The "hump" observed in curve D is believed to be evidence of clusters; thus a combination of nonequilibrium and equilibrium segregation (curve C) is thought to describe the solute distribution found by Auger microscopy techniques (25).

The last model to explain temper embrittlement is based on a concept of cosegregation (26, 27) of alloy and impurity atoms. Guttmann et al. (27) explain the phenomena of reversible temper embrittlement (RTE) on the bases of preferential attractive interactions between metallic elements (M) and nonmetallic impurities atoms (I), in which attractive interactions at the grain boundary enhance segregation and thus embrittlement; the same attractive interactions in the bulk hinders segregation to grain boundaries, due to the scavenging of I by M atoms in the matrix. The cosegregartion model seems to agree with observations by Joshi and Stein from Auger microscopy, discussed previously, and with observations by Marcus (19) and Schulz (20) who state that diffusion of embrittling elements to grain boundaries happens during the embrittlement treatment (on tempering).

Guttmann et al. (27) state that metallic elements have a weak tendency to segregate to grain boundaries; the segregation, then, of metallic elements to grain boundaries is enhanced by the segregation P, segregation which in turn is amplified by the presence of metallic elements at grain boundaries. In this model a build-up of molybdenum at grain boundaries is attributed to a strong driving force developed by the segregation of carbon at those grain boundaries. This interactive cosegregation model provides means for a quantitative analysis of intergranular segregation of phosphorus and alloy element molybdenum (27).

Moulder and Joshi (26) point out that recent data shows that cosegregation occurs selectively with larger amounts of segregated elements at certain grain boundaries. They also indicate that statistical analysis shows that crack propagates through nickel and antimony-rich zones rather than along the interface of nickel and antimony-rich zone and the matrix.

The characteristic behavior of molybdenum discussed in previous sections is explained by Qu and McMahon (17) based on a cosegregation theory. Their explanation is based on a molybdenum-phosphorus scavenging reaction at short aging times, which is then followed by the precipitation of molybdenum carbides what leaves phosphorus free to segregate and produce embrittlement. Vanadium is thought to interfere with the molybdenum-carbide formation making even slower the embrittling phenomena (17).

In summary, the segregation in temper embrittlement has been a phenomena difficult to completely identify. Temper embrittlement may involve one or more of the models reviewed, and may be enhanced by carbide precipitation at prior austenite grain boundaries. Carbide platelets at grain boundaries provide sites for impurity segregation and the resulting embrittled interfaces provide an easier path for crack propagation.

1.4 High Cycle Fatigue

Cyclic loading of metallic components can cause failures at nominal stress levels well below the yield strength of the material (28). Reliability is an important requirement in engineering materials and components. Thus, considerations of fatigue behavior are needed to select materials and to design structural components (29). Fatigue constitutes 70 % of failures of mechanical components (30). During this type of failure the component supports full load up to the last cycle (31), which makes fatigue failures sudden and some times catastrophic events.

1.4.1 General Aspects of Fatigue. Failure by fatigue is a progressive phenomena in which a cyclic stress acting on a component produces microstructural changes, which lead to microcrack initiation; then progressive propagation of the cracks cause complete fracture of the component (29). The number of cycles spent to final fracture depends on the applied stresses and in particular on the stress ratio. The process of failure by fatigue may be divided into four steps: a) surface plastic deformation, b) crack initiation, c) crack propagation, andn c) final fracture (32, 33). The stress ratio below which the material is able to withstand infinite number of cycles is the endurance limit of the material (30).

1.4.1.1 Initial Plastic Deformation and Crack Initiation. An important aspect in fatigue is a cyclic hardening or softening of the component (34). This saturation hardening or softening occurs at an early stage during the fatigue life of the part, if the strain range is maintained constant. The microstructural changes related with cyclic softening and hardening can lead to the initiation of fatigue cracks (34).

Slip bands provide evidence for initial plastic deformation during cyclic loading (35, 31). Slip bands, "persistent bands", etc. can be classified as cumulative damage at the surface layers of the component (34), and lead to the formation of extrusions and intrusions (11, 33, 35). The resulting surface damage leads to crack nucleation on planes parallel to the operating slip bands. Formation of intrusions and extrusions is enhanced in alloy systems which promote planar slip (32, 35).

Figure 1.5 shows a schematic representation of fatigue crack growth zones in a medium carbon steel. The first period of fatigue crack initiation and growth, in which the crack develops on planes parallel to slip planes, is known as stage I of crack propagation. This stage extends only a few grains deep into the material and is characterized by a slow crack growth rate (34).

Environmental conditions influence crack initiation processes (34), but are not included in this literature review.

Notch sensitivity also plays a role in fatigue crack

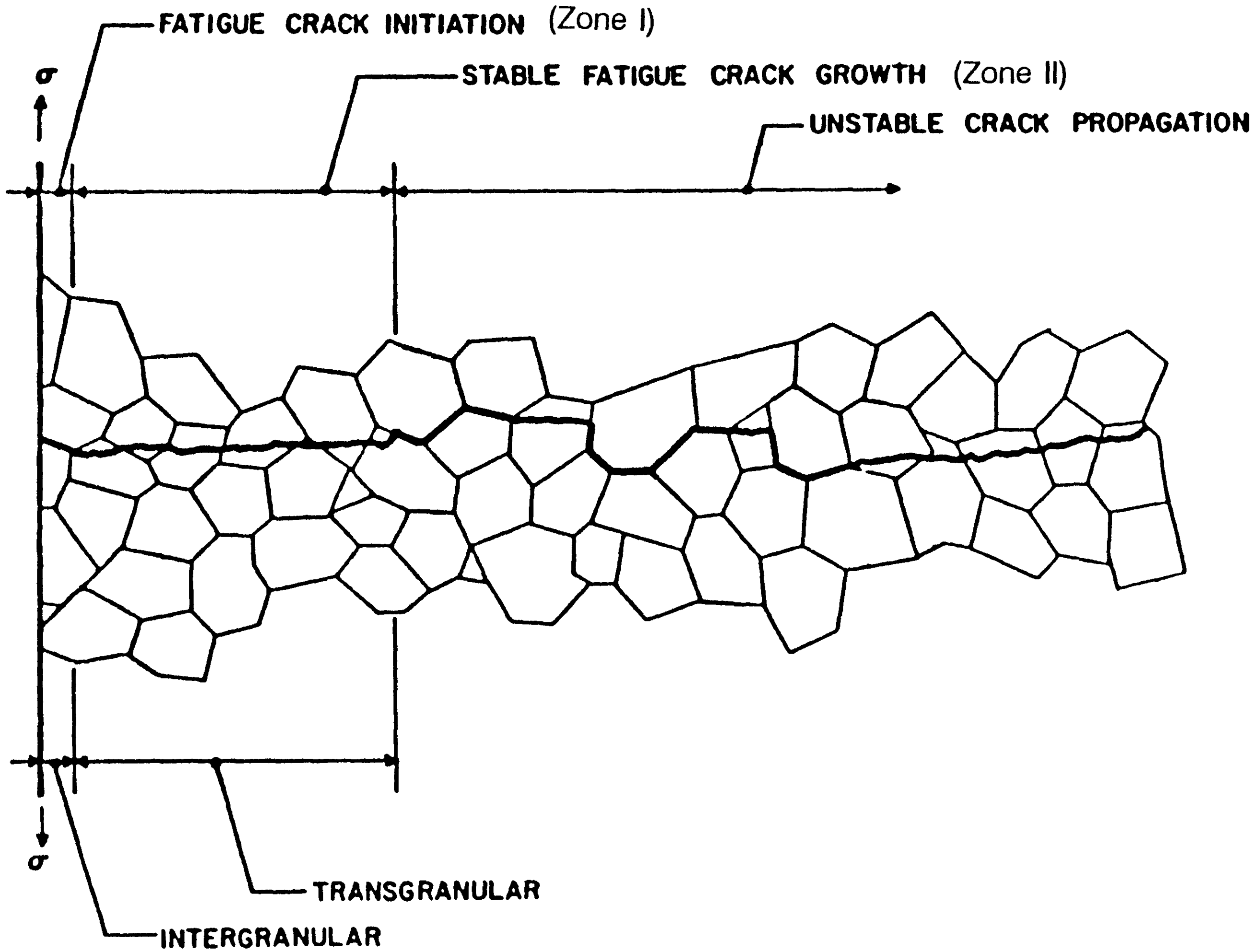

Figure 1.5 Schematic of the fracture path during fatigue crack propagation in medium carbon steel (Ref. 57).

initiation (32). The local-critical plastic strain required to initiate a crack depends on the notch sensitivity (32). In a material with a high notch sensitivity (low toughness) even small intrusions on the surface will provide the required stress concentration to initiate a crack (31). Further discussion on toughness is presented in section 1.5.

During high cycle fatigue a large percentage of the fatigue life is spent in crack initiation (34). Manson (34) points out that during crack initiation, an important factor controlling the fatigue life of a part is its tendency to deform. Thus in high-cycle fatigue, where the capacity of elastic deformation is a controlling factor of crack initiation, high yield strengths are required for high fatigue lives.

1.4.1.2 Growth and Final Failure. As the crack grows into the material, where conditions of higher constraint exist, the crack propagation mode changes from one in which the crack grows along planes with high resolved shear stresses (stage I), to a mode in which the crack propagates in a plane perpendicular to the maximum principal tensile stress (stage II) (see Figure 1.5) (35). During this stage the fracture mode is transcrystaline

(34), and striations are a characteristic feature of the fracture surface.

Formation of fatigue striations is thought to be related to plastic deformation at the tip of the crack as it progresses (35). During crack propagation the tip of the crack is subjected to a process of blunting and resharpening which causes the crack to grow different lengths in each cycle (34). Plumbridge (33) indicates that high strength materials may not show striations on their fracture surfaces due to the low ductility at the tip of the crack. He also indicates that stage II mode of crack growth comprises a large area on the fracture surface.

Manson (34) states that crack growth is a process in which cracks merge instead of a process of single crack growth, and that this growth is a function of crack length and plastic strain. He also points out that growth in stage II does not follow a linear damage rule (34). Final fracture during fatigue failure is a complex phenomena in which large plastic strains exist and the crack reaches a critical crack length for the imposed stress amplitude.

<u>1.4.1.3 Crack Growth Rate</u>. The ability to predict the fatigue life of a component depends on the understanding of the fatigue-crack growth process. Fatigue

life of a component is determined by the number of cycles spent during initiation and propagation of a crack to a critical size (28). The growth rate of the propagating crack is determined by the change per cycle in the imposed stress intensity factor, K_I (28). The stress intensity factor defines the magnitude of the elastic stress field around the crack tip. The magnitude of this factor may be changed by the size, orientation and geometry of the part, by the crack shape, and by the applied stress; however, the distribution of the elastic strain field at the tip of the crack is invariant for mode I loading (tensile loading) (28).

When the stress intensity factor K_I reaches the critical value, K_{Ic}, total failure of the component takes place by unstable crack growth through the remaining cross section of the part (28). Evaluation of K_{Ic} values is discussed in section 1.4.2.

Fracture mechanics analysis (28) indicates that the fatigue life (for constant-amplitude loading), of components with initial cracks or those which develop cracks early in life, depends on the crack propagation rate. Therefore, under conditions of constant-amplitude stress-range, a large percentage of the fatigue life is spent when the crack is still very small. The fluctuation of the stress intensity factor (ΔK_I) represents the mechanical driving force for crack growth. ΔK_I includes the effect of changing crack length and of cyclic-loading (28).

In steels the main factor which affects the crack growth rate in region II (region above the threshold region I) is the range of fluctuation of the stress intensity factor (ΔK). Experimental data on fatigue-crack-growth rate in high-yield-strength martensitic steels (with yield strength above 552 MN/m^2 (80 ksi)) has shown that this growth rate is not significantly affected by mechanical or metallurgical properties of a steel. The crack growth rate for the different steels fall within a band.

1.4.2 Factors Affecting Fatigue Behavior. Fatigue damage starts at regions of a part where stress raisers increase the local stress to values above the yield strength of the part (28). Cracks initiate and propagate in this plastically deformed zone, affecting the fatigue life of the component (28). The effect of metallurgical features, and of test and surface conditions on the initiation of fatigue cracks will be discussed in the following sections.

1.4.2.1 Metallurgical and test conditions. Plastic deformation due to dislocation motion is affected by the free-slip distance, which in turn depends on the grain size or on the presence of second phase particles or other dislocations. Grain boundaries and second-phase particles restrict dislocation motion (35). The fatigue strength increases with decreasing grain size and by increasing the number of strengthening dislocation-particle interactions. Plumbridge (33) indicates that crack propagation can be hindered by grain or subgrain boundaries, when the region across the boundary does not have a favorable orientation for crack propagation. The positive effect of fine grain size on fatigue life can also be explained in terms of compatibility requirements for plastic deformation. With a large number of grains per unit area, compatibility requirements are easily satisfied so that the probability of producing discontinuities is lower (33). Thus, fatigue life is increased since the number of potential crack initiation sites is reduced.

Inclusions may be harmful to fatigue strength. Evidence indicates that silicate and nitride inclusions are notably harmful if present in stress concentration zones (35). The shape of the inclusion also is an important factor, since elongated or needle like inclusions constitute stress raisers (35, 37). Forsyth (11) emphasized that, in most cases, the important particles affecting fatigue behavior are those close to the surface which concentrate plastic strain and become crack initiation sites. Thomson (38) presents evidence of a strong effect of non-metallic inclusions on the fatigue life of a component and points out the importance of alumina as well as that of silicate and nitride. Sulfides do not have an important effect on fatigue life (38).

Microstructure also plays an important role in fatigue life. Chapman et al. (39) showed that a small amount of nonmartensitic products at the surface of a fatigue specimen reduces the fatigue strength. Borik et al. (37) attribute better fatigue properties in a bainitic microstructure than in a tempered-martensitic microstructure of the same hardness (above 40 Rc), to the absence of residual microstresses, rather than to metallographic differences between the two microstructures. He also states that austempering, for the same reason, enhances fatigue strength of a steel.

It has been shown that fatigue crack initiation often occurs at stress raisers which lie on or just below the surface. The stress raisers include, embrittled grain boundaries (33), inclusions (31), hard oxide particles (1), nonmartensitic products, etc. However, crack initiation can take place in the absence of such stress concentrators (33), and the fatigue life is increased. It is important to emphasize that microstructural features affect stage I (few surface grains) of crack growth, but that such effects on stage II (transgranular fracture) of crack growth are small (33).

Test conditions, such as moisture content in the test atmosphere or a corrosive environment, strongly affect fatigue life (38, 31). However, variations in the test temperature (between 21-121°C (70- 250 °F)) in non-aggressive environments do not seem to have a strong influence on fatigue (31).

1.4.2.2 Surface Condition. It is generally believed that surface layers play an important role in fatigue crack initiation in metals and alloys (40). Takemoto et al. (40) indicate that the endurance limit and the fatigue life in a precycled component is adversely affected by an accumulation of fatigue damage in a surface layer of about 25 micrometers thick. Removal of such a layer restores the initial fatigue properties of the component (40).

Surface hardness is then expected to influence fatigue life. It has been shown in previous sections, that surface grains may behave as soft material, where cracks initiate by reverse strain cycling. Frankel (41) indicates that the fatigue strength is a linear function of hardness to a certain value, after which endurance limit rapidly decreases. Maximum value of hardness depends on steel carbon content.

Frankel (41) also indicates that the surface finish strongly influences the fatigue life and endurance limit. Surface discontinuities reduce fatigue life. It is important to point out that surface finishing by grinding can develop residual tensile stresses in the grinding direction which can adversely affect fatigue life. The magnitude of these stresses depend on the cutting depth and speed (42) during grinding.

1.5 Notch-toughness

Notch toughness is another important mechanical property, in addition to yield and fatigue strength. Notch toughness is the ability of a material with a notch to absorb energy during dynamic loading (28). Stress raisers (28), such as those discussed in previous sections, can make a material fracture in a brittle manner.

Notch-toughness of steels which contain bcc or bct iron is characterized by the transition from ductile to brittle fracture during impact testing. The fracture mode of a material can change from a ductile to a brittle manner depending on service conditions such as temperature, loading rate and constraint (28). In an absorbed energy versus test temperature plot, the zone of the curve in which the material is considered to fail by a combined mode of ductile and brittle fracture is referred to as the mixed-mode region (28). A brittle material has this mixed-mode region shifted to higher temperatures (11) compared with an unembrittled material. In a brittle material large amounts of brittle fracture can take place at room temperature. Notch-toughness is evaluated by impact and fracture toughness tests, as summarized in following sections.

1.5.1 Notched bar impact toughness. The Charpy V-notch impact test gives the amount of energy absorbed during impact loading of a notched sample (43). The amount of energy absorbed during the impact is a function of the amount of ductile fracture present in the fracture surface of the broken sample.

Impact toughness is a means to analyze the behavior of a material subjected to a single application of load, which results in a triaxial tensile stress at the root of the notch (43). Performance of this test at different testing temperatures allows the determination of the ductile to brittle transition temperature and the susceptibility of the material to brittle fracture (43).

It was indicated in previous sections that temper embrittlement is associated with a shift of the impact-transition temperature to higher temperatures, and with a reduction of the impact energy at room temperature, when the material is tempered at temperatures above 425°C (797°F) (1). As discussed earlier, the impact toughness is strongly affected by composition when impurity elements are present in the steel.

1.5.2 Fracture Toughness. Plain-strain fracture toughness tests give the critical stress-intensity factor, K_{Ic} (44). This factor describes the resistance of the material to fracture in the presence of a sharp crack and in a benign environment (44). In order to obtain valid values, the stress state near the crack tip must be a triaxial-tensile stress state in plane strain, and the plastic zone around the crack tip must be small compared to the crack and the sample size. The value of toughness obtained with this method is regarded as a minimum value of toughness (44). K_{Ic} can be related to the maximum stress that a component can withstand during service in the presence of a flaw of a given size when high constraints are expected in the component.

Fracture toughness specimens need to be of a certain size in order to provide the required plane strain condition. When only material which is too thin to produce plain strain conditions is available, side-grooved specimens can be used to obtain valid (or close to valid) K_{Ic} values (45) (This technique is utilized in some of the fracture tests considered in this thesis). It has been reported (45, 46, 47) that K_{Ic} values obtained with this method are basically the same as those obtained from specimens meeting ASTM standard E-399. This method is being evaluated and the possibility of including it as an specimen alternative in the E-399 ASTM standard procedure is being considered (48). The method is based on the fact that thin specimens exhibit a considerable amount of stable crack growth prior to unstable crack propagation. If the stress intensity factor is calculated at this crack growth initiation point, the value obtained will be basically the same as those obtained following the E-399 standard.

Side-Groove depth and radius have an effect on the stress state at the crack front (45). More uniformly distributed stresses develop and the crack front is straighter. Correspondingly, better K_{Ic} values are obtained. It is reported (45) that side groove depth should be less than 10% of the thickness of the sample so that compliance is virtually unaffected. The relative effect of groove depth and radius may change depending on the plasticity of the material.

Correction of the stress intensity value obtained with a side grooved specimen is made by multiplying the K_{Ic} value calculated for the nominal thickness (B) of the CT specimen by $(B/B_n)^{1/2}$ where B is the nominal thickness and B_n is the reduced thickness at the notch root (see Figure 2.5).

It has been reported (45) that basically the same K_{Ic} value has been obtained for aluminum specimens 63.5 mm thick meeting the ASTM standard, and for smooth specimens 19.1 mm thick when the stress intensity factor has been calculated at the crack initiation point. Even thinner specimens (12.5 mm thick) yield the same value when when tested with side grooves.

Fracture toughness is a material property independent of specimen geometry (49), provided the requirements of constraint are met. Thus the purity of the material is expected to influence the K_{Ic} value of the material (49). Carman (49) in a study of the effect of purity on fracture properties of materials, found that high purity 4340 steel had higher K_{IC} values than those of a 4340 steel with higher content of phosphorus and sulfur. This was reflected in a larger critical crack size in pure materials (49).

Since both the fracture toughness and the impact toughness are improved as the degree of purity is improved (50), Cotrell (50) carried out experiments to determine if impurity elements in steels affected fracture toughness as they do affect impact toughness (4). From this study Cotrell (50) concludes that additions of sulfur, phosphorus, arsenic and tin reduce the fracture toughness compared with the pure steel (steel without impurities). He also observes that the effect of two impurity elements combined is stronger than that of a single impurity. This effect is stronger when the steel is tempered in the temper embrittlement range (400°C (752 F)). He also points out that fracture toughness in pure steels is higher when tempered at 400°C (752°F) than when tempered at lower temperatures.

It has been shown that TE is an embrittling phenomena which can develop in steels containing chromium, manganese and nickel, when impurity elements are present in the steel. This embrittlement can deteriorate several mechanical properties of embrittled steels. The experimental procedure of this thesis evaluates the susceptibility of thin sections of 5160H steel to TE, and its effect on the fatigue and toughness of the steel. The experimental procedure is described in the following chapter.

2 EXPERIMENTAL PROCEDURE

2.1 Materials and Heat Treatment

Two 5160H steels were received from Stelco, Inc. and their compositions are summarized in Table 2.1. This table also shows the specification range for 5160H steel; both steels satisfy the specified composition. For reference in this thesis the steels are referred to as either the "high-residual" or "low-residual" steel. The high-residual steel has a higher content of phosphorus, nickel, manganese and tin, elements which potentially make the material more susceptible to embrittlement.

The experimental steels were received in the form of hot-rolled plate with cross-sectional dimensions of 7.4 mm x 64 mm (.29 in x 2.5 in.) for the low-residual steel and 9.2 mm x 64 mm (.36 in. x 2.5 in.) for the high-residual steel.

All samples used in this study were austenitized at 830°C (1526) for 30 minutes and quenched to room temperature in oil. Table 2.2 indicates the five tempering temperatures between 200 and 600°C (392-1112 °F), and the two post-tempering cooling rates (Air Cool (A.C.) and Water Quench (W.Q.)) studied. The samples were held at the tempering temperatures for one hour. Barium salt-pots

TABLE 2.1: Compositions of Experimental 5160H Spring Steels (Weight Percent).

Identification	C	Mn	Cr	Si	Ni	Mo	Cu	Cb	P	S	N
Low Residual	.57	.79	.80	.23	.058	.002	.17	.05	.008	.0018	.008
High Residual	.58	.95	.78	.26	.08	.014	.25	.04	.022	.022	---
AISI SPEC	0.55/0.65 C, 0.65/1.00 Mn, 0.035 P_{max}, 0.040 S 0.15/0.30 Si, 0.6/1.00 Cr										

TABLE 2.2: Tempering Conditions for 5160H Spring

Tempering Temperature	Post-Tempering Cooling Rate A.C.	W.Q.
203°C		X
304°C		X
420°C	X	X
500°C	X	X
595°C	X	X

baths were used for the heat treatments.

Fatigue tests were performed for each condition summarized in Table 2.2 except for samples air cooled after tempering at 595°C (1103°F). The as-quenched condition of the low-residual material was also evaluated in fatigue. A total of sixteen test conditions (i.e., material plus thermal history) were evaluated in this study.

2.2 Specimen Preparation

Flex-beam fatigue samples (Krause Type) were machined to the dimensions shown in Figure 2.1. The tapered sample has an extended section which is subjected to a constant stress in bending. Thus, in contrast with a rectangular sample, the geometry evaluates a larger test area allowing the effects of microstructure on fatigue behavior to be systematically evaluated. The specimens were surface ground to final dimensions after tempering. To avoid grinding-induced residual stresses, the last two grinding passes were limited to 0.0127 mm (0.0005 in.). After surface grinding, a radius of 0.127 mm (0.005 in.) was ground on the sharp corners of the tapered test area on each sample.

One fatigue sample was prepared as a calibration

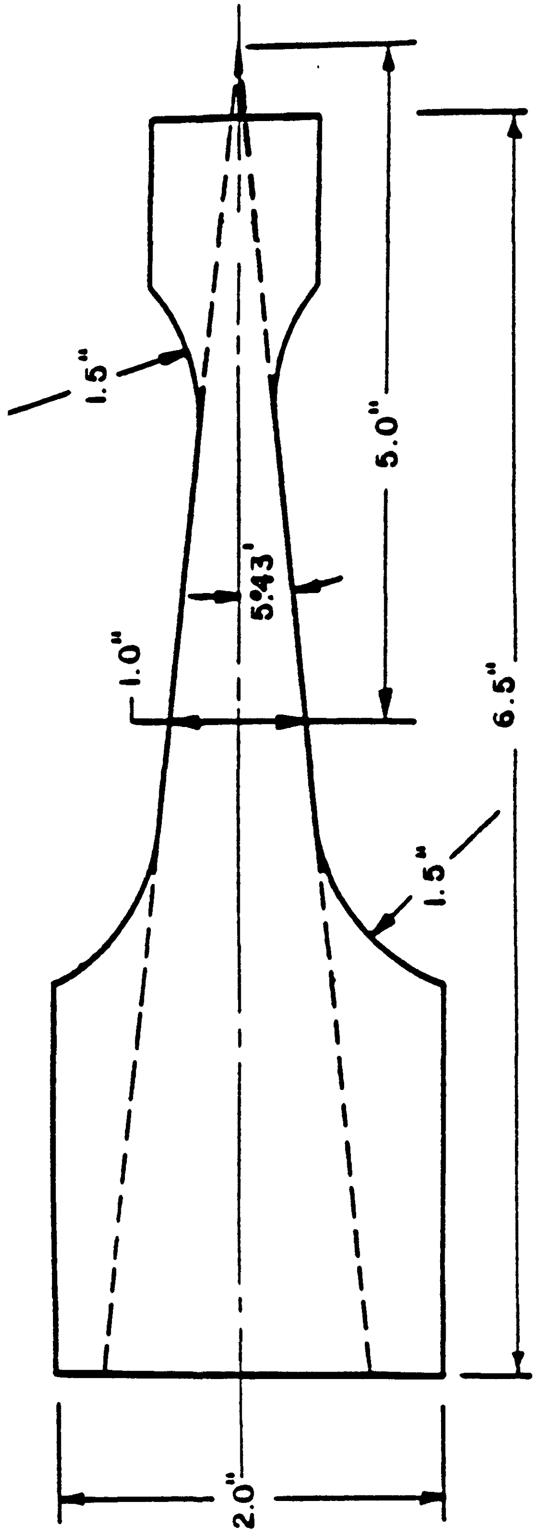

Figure 2.1 Krause type sample for flex-beam bending fatigue testing.

sample with three strain gages equally spaced on the 6.9 cm (2.75 in.) tapered gage section. The strain gage output, which was monitored with a BLH Electronics-1200 strain indicator, was used to develop a calibration curve for setting the imposed stress amplitude. Strain readings from the calibration sample indicated that the imposed stress was essentially constant throughout the gage section.

Examination of broken-test samples showed that the crack nucleation occurred at locations randomly distributed throughout the gage section. No cracks nucleated at the sample corners or at the fillets on the ends of the tapered section. Samples tested at high stress levels showed multiple cracking. This observation indicates that the fatigue samples provide a constant-stress test zone.

Transverse sub-size Charpy V-notch impact samples were machined in the L-T orientation, as indicated in Figure 2.2. Samples with a thickness of 7.2 mm (0.28 in.) were machined to the dimensions shown in Figure 2.3. The maximum sample thickness was limited by the plate thickness. Other dimensions meet E-23 ASTM standard (43).

Compact-tension (CT) fracture-toughness samples were also machined in the L-T orientation as shown in Figure 2.2 and according to the dimensions shown in Figure 2.4. A maximum thickness of 7.2 mm (0.28 in.) was limited by the

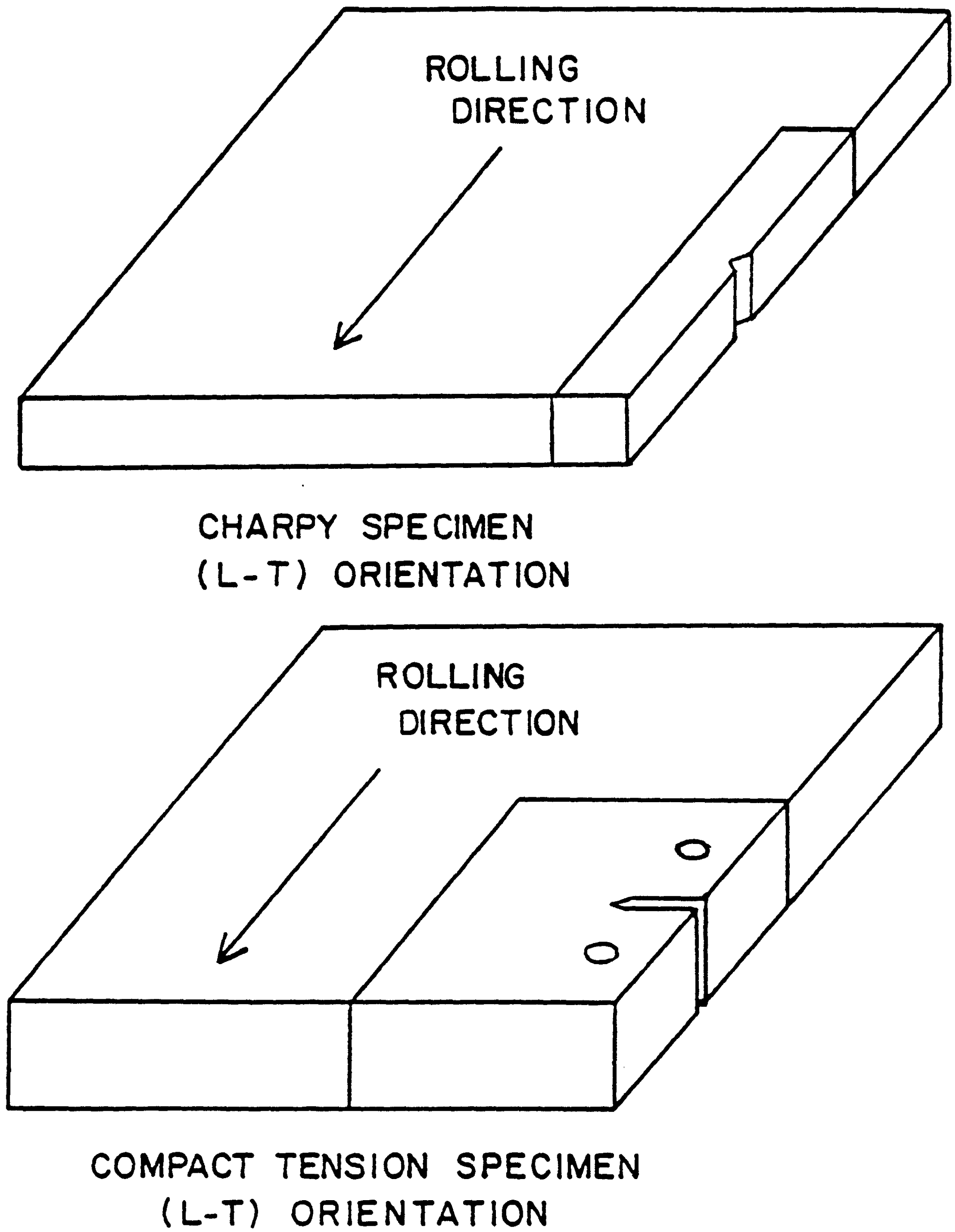

Figure 2.2. Crack orientation code for the Charpy-impact and for the CT specimens.

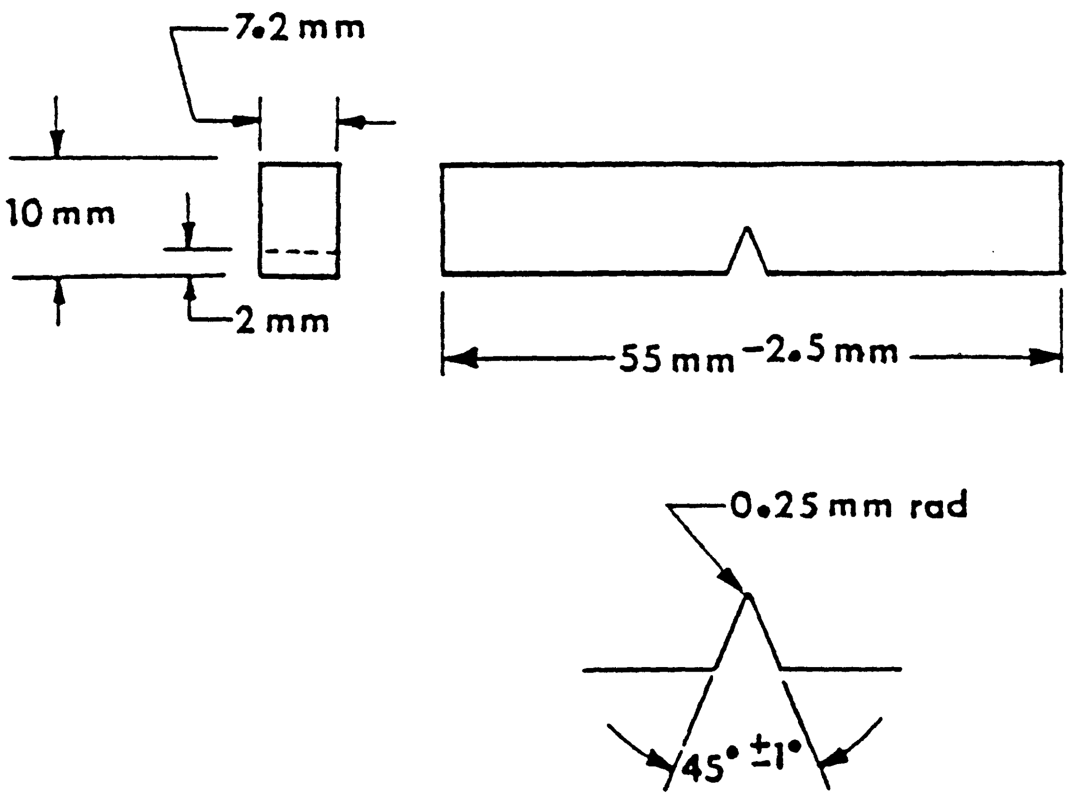

Figure 2.3 Substandard Charpy-impact test specimen.

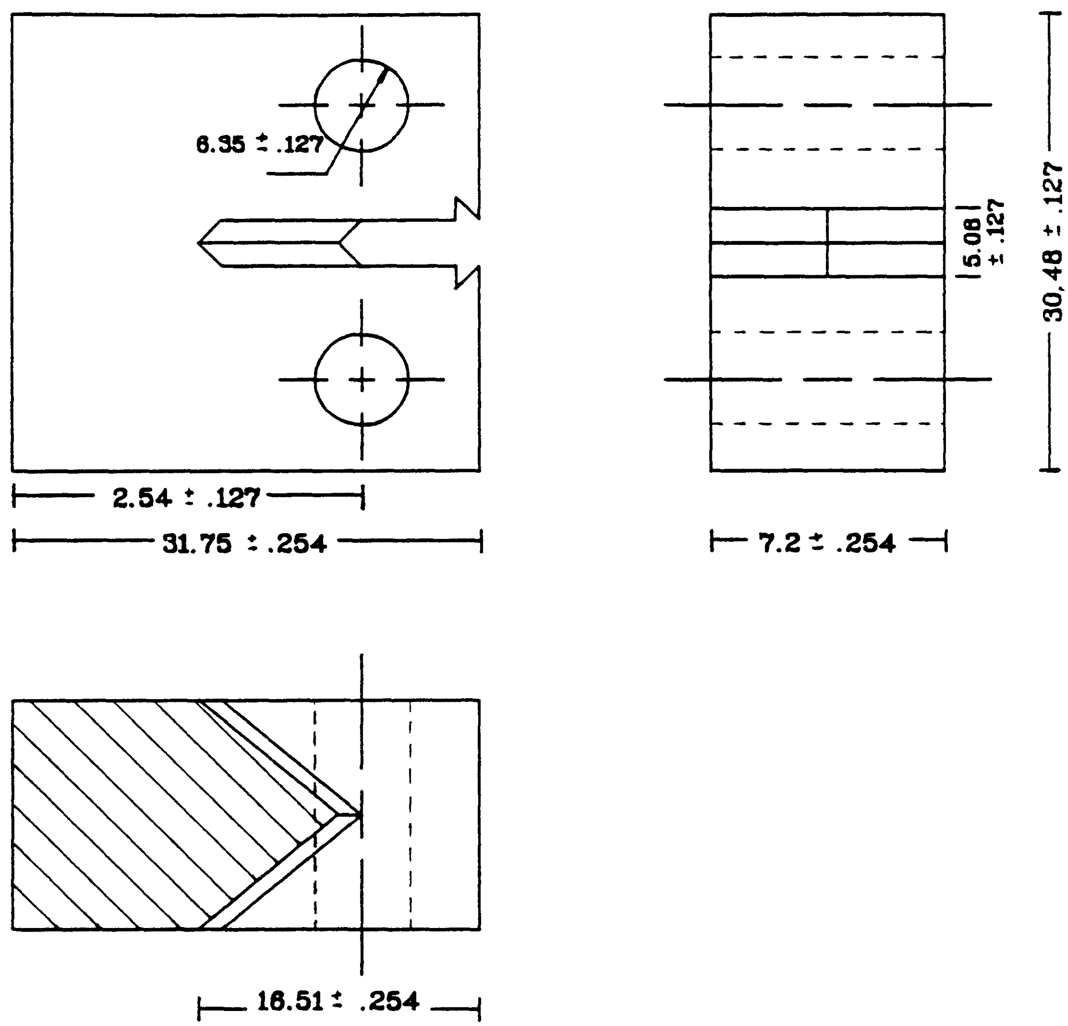

Figure 2.4 Compact specimen C(T) dimensions and tolerances. Dimensions in millimeters.

plate thickness; the other dimensions and tolerances meet requirements established in the E-399 ASTM standard (44). To facilitate obtaining valid K_{IC} values, all samples were modified after precracking by the introduction of side grooves to a depth of 0.065 mm (0.026 in.) on each side as shown in Figure 2.5. The notch-included angle and the tip radius are 45 and 0.25 mm (0.01 in.), respectively.

2.3 Mechanical Testing

2.3.1 Hardness. Standard Rockwell C hardness testing was performed on a Leco R-600 digital hardness tester. Calibration of the machine was confirmed with standard calibration samples. Through-thickness microhardness traverses on several fatigue samples were obtained with a Micromet Microhardness tester with a load of 100 g. Rockwell C hardness values were obtained from both ends of the fatigue samples, and from one compact tension-fracture sample for each heat treatment.

2.3.2 Fatigue. A Budd-VSP-150 flex beam machine (Krause type) was used for fatigue testing. It is a constant-strain type machine operated at 1800 RPM (30 Hz). The deflection is applied to the specimen by the cam action of the machine linkage arm. The applied deflection to produce a specified surface stress is determined from the

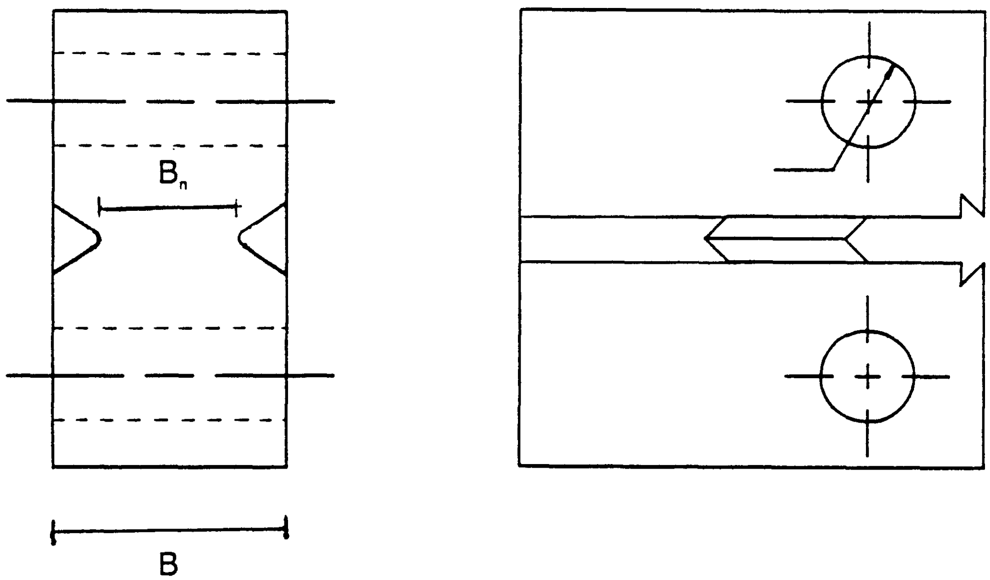

Figure 2.5 Side grooved compact specimen used to determine K_{Ic} values. B is the specimen thickness, and B_n is the distance between the apexes of side grooves.

strain gage calibration curve and controlled by adjusting the maximum vertical displacement of the machine arm. The fatigue tests were performed under tensile-tensile stress at the upper surface of the sample (resembling a leaf-spring stress state during service) and at a constant minimum stress of 158 MPa (2300 psi). The tests were run in ambient atmosphere and at room temperature.

It is important to bear in mind that the objective of the project was to determine the general trend of changes in the endurance limit with tempering conditions and residual alloy content. The fatigue testing program was designed to optimize the use of available samples to test a large number of tempering temperatures. Many more specimens than available would be required to more accurately establish valid endurance limits.

2.3.3 Notch-Toughness. A Tinius Olsen impact-testing machine was used for Charpy V-notch impact tests. The machine has a maximum capacity of 358 joules (264 ft-lb) and a pendulum velocity at impact of 3.5 m/sec (11.5 ft/sec).

Test temperatures were -94°C, -70°C,-20°C, 22°C, 100°C and 135°C. Sample temperature was controlled in isothermal baths for 10 minutes at temperature. Methanol cooled with liquid nitrogen was used for test temperatures below room temperature (22 C). Heated oil was used for the high test temperatures. Less than 5 seconds were allowed after removing the sample from the bath and before impact. This follows E-23 86 ASTM standard recommendations (43).

A model 810 MTS servo-hydraulic machine with a 89 kN (20000 lbs.) capacity was used for fracture toughness testing. Fatigue precracking was done in load-control, with a cyclic tensile-tensile stress between 1.7 and 8.3 MPa (250 - 1200 Psi) at 45 Hz. Fracture toughness testing was performed in stroke-control at a displacement rate of 1.9 mm/min (0.075 in/min). Tests were performed at 22°C (72°F) and -26°C (-79°F); load displacement plots were obtained on an x-y recorder. ASTM standard E-399 (44) was followed for both fatigue precracking and fracture toughness testing.

2.4 Microscopy

A Leco Neophot 21 metallograph was used for metallographic analysis. Samples were etched with 2 % nital, and 4 % nital / 4 % picral etchants to reveal the microstructures of the different tempering conditions. A saturated solution of picric acid in distilled water was used to reveal prior austenite grain boundaries and temper embrittlement in the different material conditions tested.

To determine temper embrittlement, the samples were first lightly etched with 2 % nital, and then lightly polished before submerging the samples for 30 and 40 minutes in the picric-acid solution. Light polishing slightly was also required before the metallographic analysis.

Fractographic analysis of broken fatigue, Charpy and CT samples was carried out with a JOEL JXA-840 scanning electron microscope (SEM). All specimens were ultrasonically cleaned before the analysis. Fatigue specimens were inspected in the three characteristic zones during fatigue crack propagation (stage I, stage II and overload zones), placing special attention on the crack initiation sites. Charpy and CT samples were inspected at an specific location within the fracture surface area, this ensures a similar stress state at the region analyzed, and a better comparison between the fracture surfaces of the different material conditions. Chemical composition of particles on the fracture surfaces of fatigue samples was performed on the SEM with the Standardless Quantitative Analysis Program.

3 RESULTS AND DISCUSSION

Experimental results from the mechanical testing program and from the microscopic analysis of test samples are presented in this chapter. Mechanical test results are divided in four sections: hardness, fatigue, impact toughness, and fracture toughness. The microscopy section is divided into metallography and fractography: metallographic analysis includes light micrographs, while the fractographic analysis includes macrographs, and scanning electron micrographs.

3.1 Mechanical Testing

Variation of hardness with tempering temperature is summarized in Table 3.1 and is presented in Figure 3.1 for both materials. The hardness decreases from an as-quenched hardness of 62 HRc to 38 HRc for the sample tempered at 595°C. This trend of decreasing hardness with increasing tempering temperature corresponds with a similar variation of the yield strength with tempering temperature (51), as shown in Figure 3.2. As indicated in Figure 3.1, the hardness values are the same for the high and low-residual material. Furthermore, the cooling rate after tempering does not affect hardness values in either material.

For each tempering condition the hardness values

TABLE 3.1: Hardness and Endurance Limit Values for Low and High Residual 5160H Steel.

Tempering Condition °C/Cooling	Hardness (HRc) Low	Hardness (HRc) High	Fatigue Limit Low MPa	Fatigue Limit Low Ksi	Fatigue Limit High MPa	Fatigue Limit High Ksi
As-Quenched	62.0	-	600	87	---	---
204/WQ	57.0	57.0	1075	156	1040	151
304/WQ	53.0	53.0	1040	151	1075	156
426/WQ	48.0	47.0	1075	156	1075	156
426/AC	48.0	47.0	1040	151	1013	147
500/WQ	44.0	43.0	930	135	841	122
500/AC	42.5	43.0	930	135	841	122
595/WQ	38.0	38.0	1013	147	958	139
595/AC	37.5	38.0	---	---	896	130

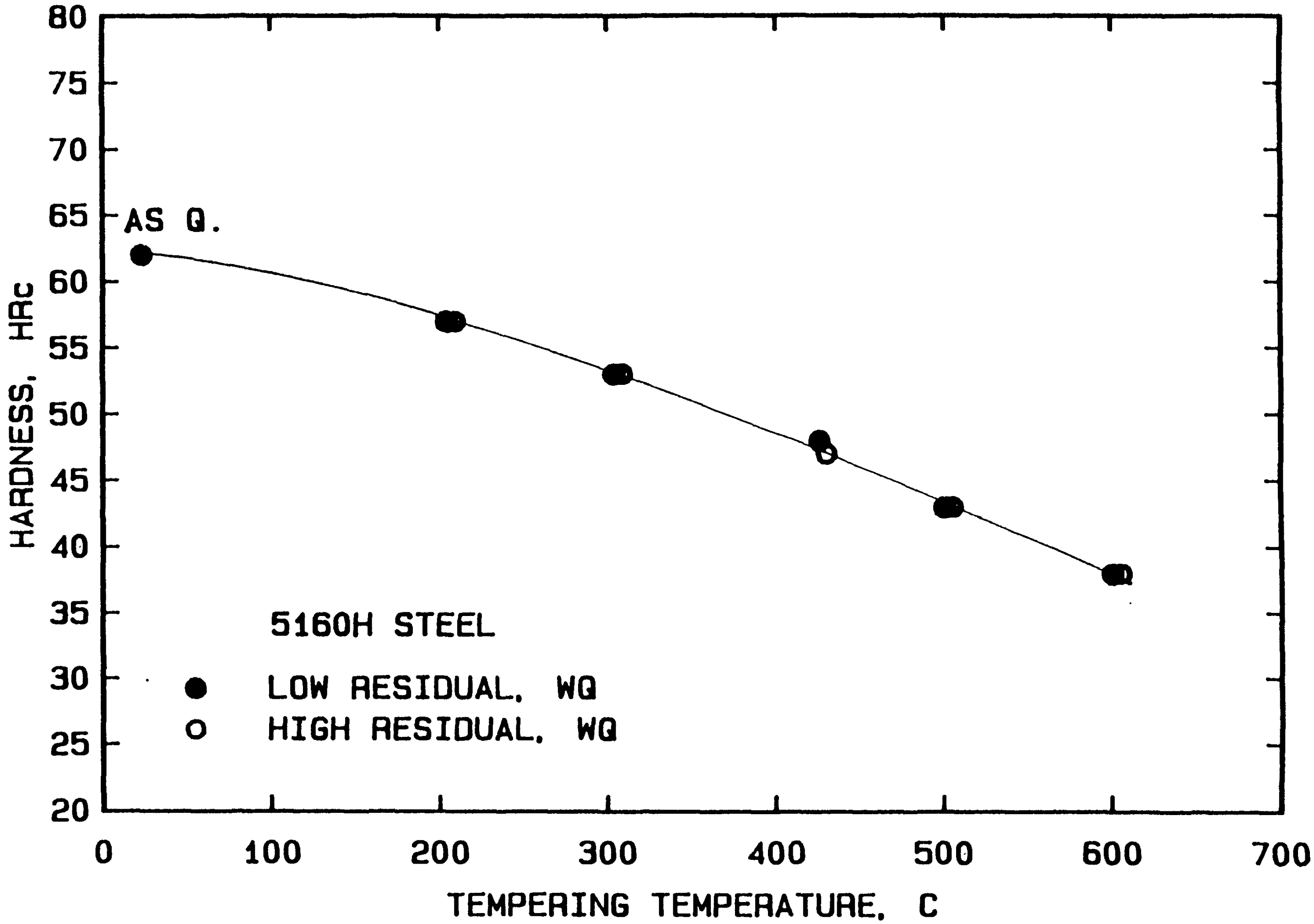

Figure 3.1 Influence of tempering temperature on hardness of 5160H steel.

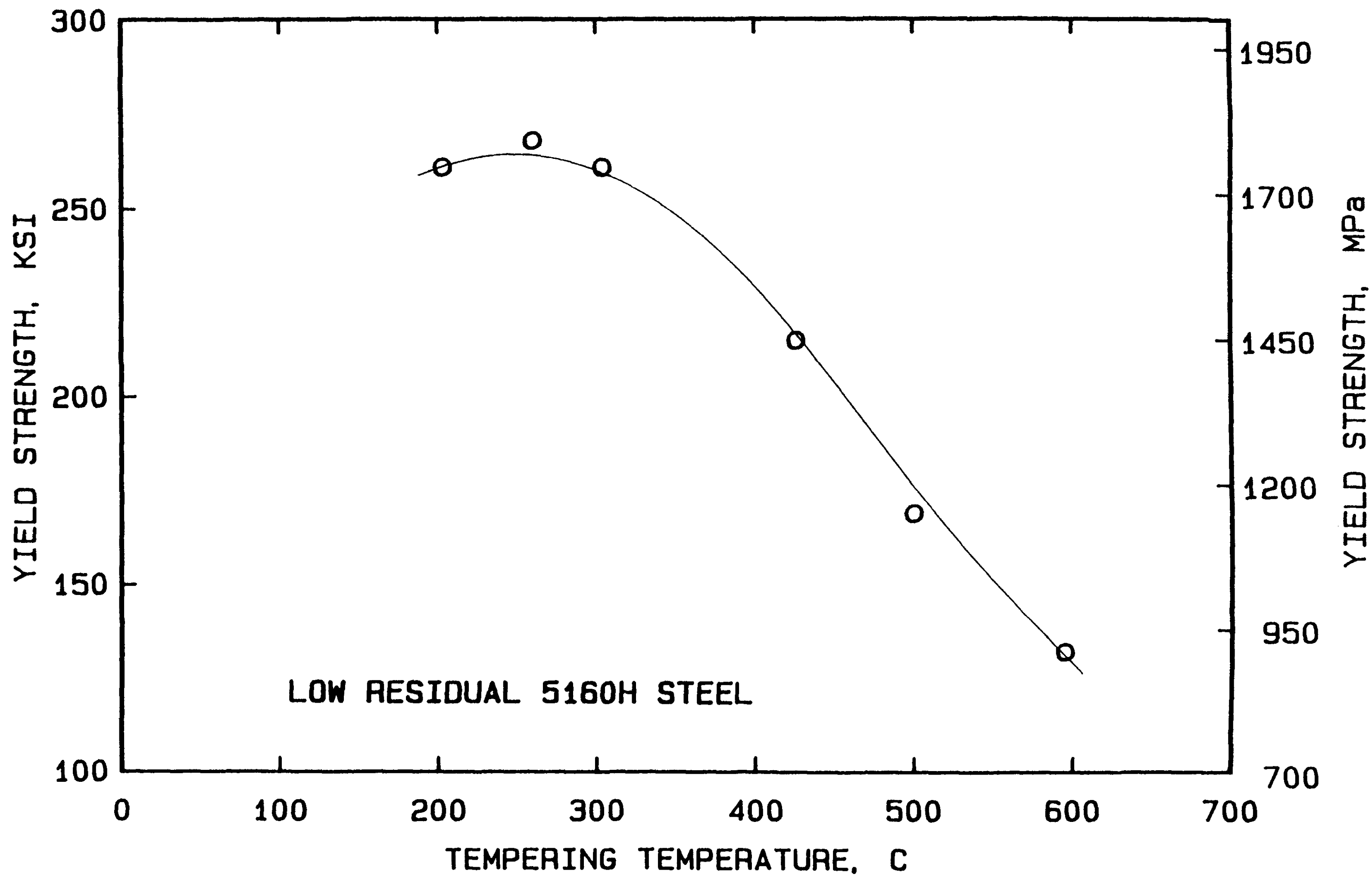

Figure 3.2 Yield strength as a function of tempering temperature for 5160H steel.

obtained from the fatigue and the CT specimens were within 1 to 2 points. This observation indicates that the heat treatment conditions for the different specimens were basically the same for each tempering temperature.

Fatigue test data for the sixteen experimental conditions are summarized in the series of figures presented as Appendix A. From each figure an approximate endurance limit was obtained, and an analysis of the effect of alloying and tempering on the observed endurance limits is presented below.

To illustrate the range of fatigue data obtained in this study, fatigue test data for three tempering conditions are presented in Figure 3.3. This figure shows the low-residual material in the as-quenched condition and in the 426 °C/AC and 500 °C/WQ conditions. All conditions exhibited well-defined endurance limits, where the endurance limit is defined as the highest tested stress level at which the sample did not fail after 10^6 cycles. The figure shows that although the as-quenched material has a high yield strength, it exhibits a low endurance limit. This observation emphasizes the importance of finding a balance between hardness and toughness in order to increase fatigue life of the material. High hardness increases the number of cycles

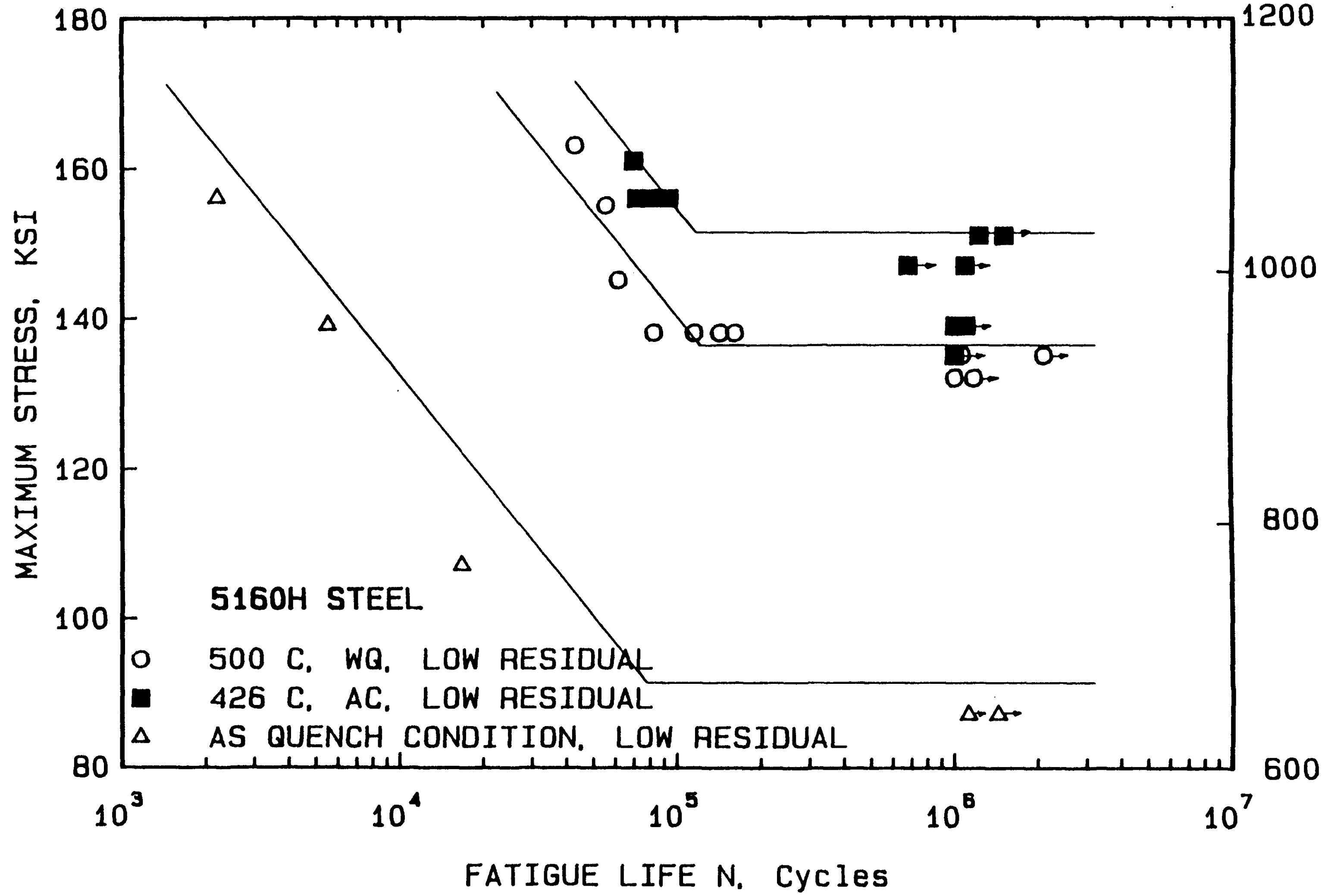

Figure 3.3 Maximum stress versus fatigue life curve for 5160H steel in the as quenched condition, and in two tempered conditions.

required to nucleate a crack (as discussed in Section 1.4.2.2), but this benefit of hardness is off-set by a low toughness which is an indication of high notch sensitivity and of a small critical crack size to cause failure; the overall effect of extremely high hardness values is detrimental as the endurance limit rapidly decreases for samples heat treated to hardness above a certain value (41).

The effect of tempering conditions on the fatigue behavior of the steel is summarized in Figure 3.4, and tabulated in Table 3.1. This figure presents the variation of endurance limit with tempering temperature. The figure includes data for the low- and high-residual materials, and for the two post-tempering cooling rates. The endurance limits are essentially constant at 1075 MPa (156 Ksi) for tempering at temperatures up to 426°C. These data are essentially independent of the postempering cooling rate. At 500°C the endurance limit decreases significantly to approximately 930 MPa (135 Ksi) for the low-residual steel and to 841 MPa (122 Ksi) for the high-residual steel. Above 500°C the endurance limit increases and is essentially independent of residual alloy content.

This decrease of endurance limit of 5160H steel, at a tempering temperature of 500°C, agrees with findings on

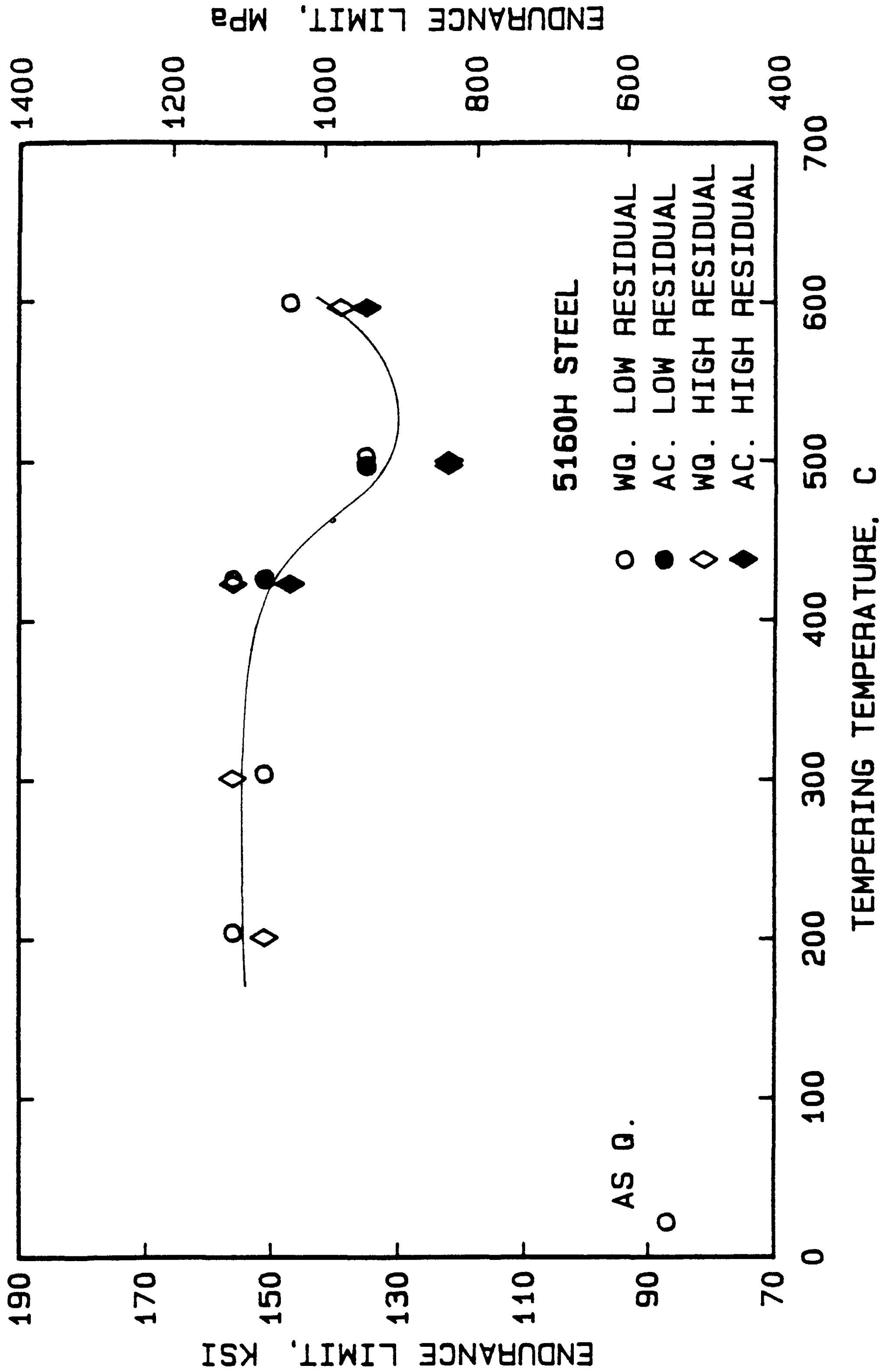

Figure 3.4 Influence of tempering temperature on the endurance limit of 5160H steel with low-residual alloy content.

a SS52 steel (52). Tempering at 500°C is a temperature of interest to industry, since a temperature range between 400 and 500°C is used during the thermo-mechanical forming of leaf springs. A reduction of endurance limit at 500°C may be related to temper embrittlement. At this tempering temperature the rate of embrittlement and the reduction of impact toughness have maximum values as shown in Section 1.3.1. In order to determine a correlation between fatigue behavior, toughness, and a possible temper embrittlement phenomena the fracture toughness of the two 5160H steels were evaluated. Results on toughness are presented in the following paragraphs.

Impact toughness was evaluated for the different tempering conditions and for the low- and high-residual materials and the results are summarized in Table 3.2 and 3.3. Figures 3.5 and 3.6 show the sub-size Charpy V-notch impact energy as a function of test temperature for the low- and the high-residual materials, respectively. The transition curves for the low-residual material, shown in Figure 3.5, exhibit the sigmoidal-shape curve expected; the impact energy increases as the test temperature increases, and the transition curves are shifted to higher temperatures as the tempering temperature decreases. As shown in the figure, post-tempering cooling rate has an

TABLE 3.2: Impact toughness values for Low Residual 5160H steel

Tempering Conditions °C/Cooling	Sub-Size Charpy V-Notch Impact Energy J (ft-lb) Test Temperature (°C) -94	-70	-20	22	100	135
204/WQ	---	3.4	---	5.2	8.4	10.2
	---	(2.5)	---	(3.8)	(6.2)	(7.5)
304/WQ	---	5.6	---	7.9	8.4	9.5
	---	(4.1)	---	(5.8)	(6.2)	(7.0)
426/WQ	13.6	12.9	12.5	11.5	16.3	---
	(10.0)	(9.5)	(9.2)	(8.5)	(12.0)	---
426/AC	6.1	11.3	12.9	12.2	18.3	---
	(4.5)	(8.3)	(9.5)	(9.0)	(13.5)	---
500/WQ	11.5	14.0	14.9	21.7	25.8	---
	(8.5)	(10.3)	(11.0)	(16.0)	(19.0)	---
500/AC	10.2	14.9	16.3	20.3	23.7	---
	(7.5)	(11.0)	(12.0)	(15.0)	(17.5)	---
595/WQ	12.2	14.0	23.7	32.5	33.2	---
	(9)	(10.3)	(17.5)	(24.0)	(24.5)	---
595/AC	14.0	14.0	24.4	29.7	36.6	---
	(10.3)	(10.3)	(18.0)	(21.9)	(27.0)	---

TABLE 3.3 Impact Toughness Values for High Residual 5160H Steel

Tempering Conditions °C/Cooling	Sub-Size Charpy V-Notch Impact Energy J (ft-lb) Test Temperature (°C) -94	-70	-20	22	100	135
204/WQ	---	3.8	---	5.4	7.5	6.1
	---	(2.8)	---	(4.0)	(5.5)	(4.5)
304/WQ	---	2.6	---	2.7	7.5	6.8
	---	(1.9)	---	(2.0)	(5.5)	(5.0)
426/WQ	5.7	5.4	9.1	10.9	14.9	---
	(4.2)	(4.0)	(6.7)	(8.0)	(11.0)	---
426/AC	4.8	7.1	10.9	9.5	15.6	---
	(3.5)	(5.2)	(8.0)	(7.0)	(11.5)	---
500/WQ	6.1	10.6	13.6	12.9	21.0	---
	(4.5)	(7.8)	(10.0)	(9.5)	(5.5)	---
500/AC	11.1	8.5	13.6	12.2	21.7	---
	(8.2)	(6.3)	(10.0)	(9.0)	(16.0)	---
595/WQ	12.9	13.8	16.3	21.7	27.1	---
	(9.5)	(10.2)	(12.0)	(16.0)	(20.0)	---
595/AC	9.5	13.4	17.0	23.1	31.2	---
	(7.0)	(9.9)	(12.5)	(17.0)	(23.0)	---

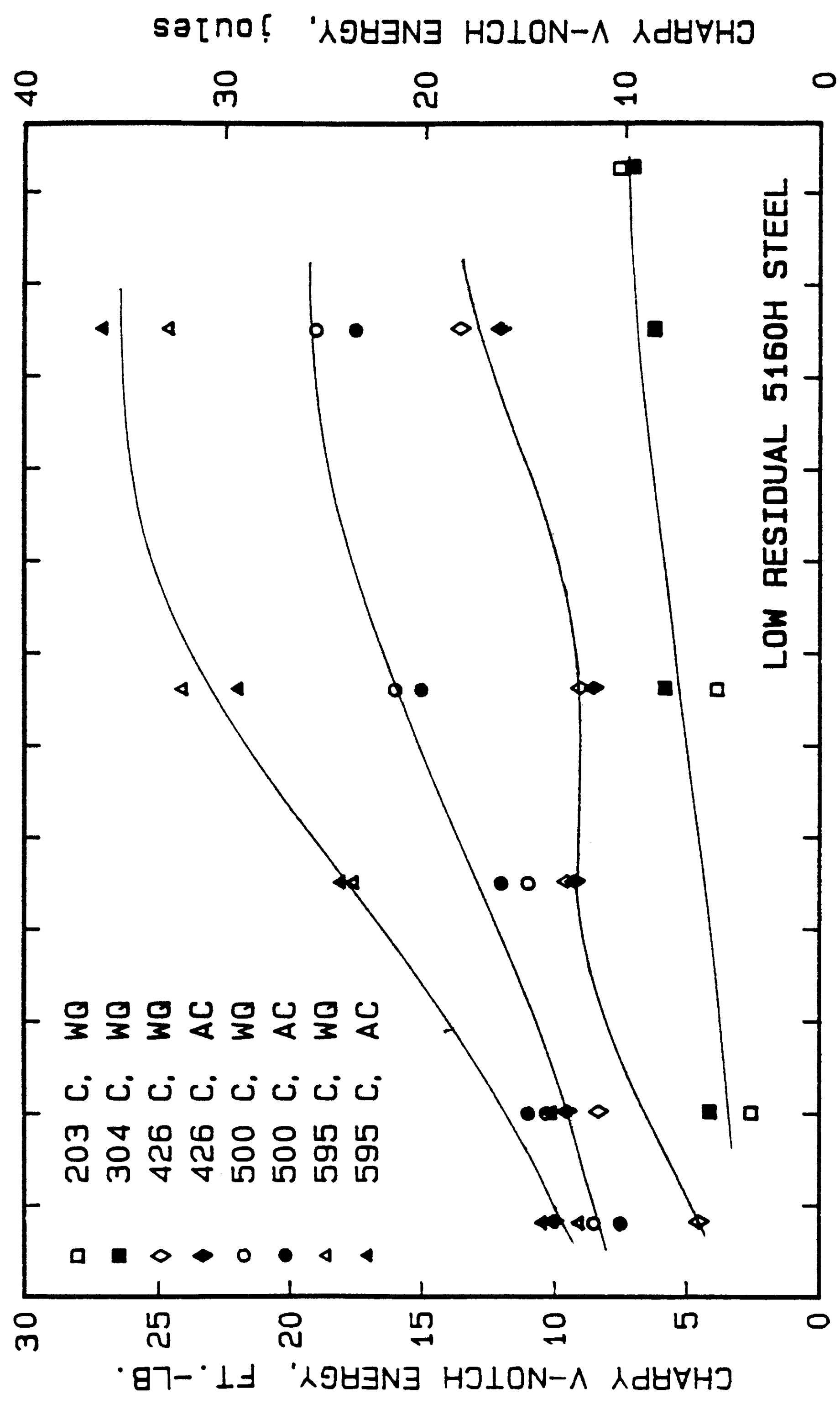

Figure 3.5 Subsize Charpy V-notch impact energy as function of testing temperature for different tempering conditions for low-residual 5160H steel.

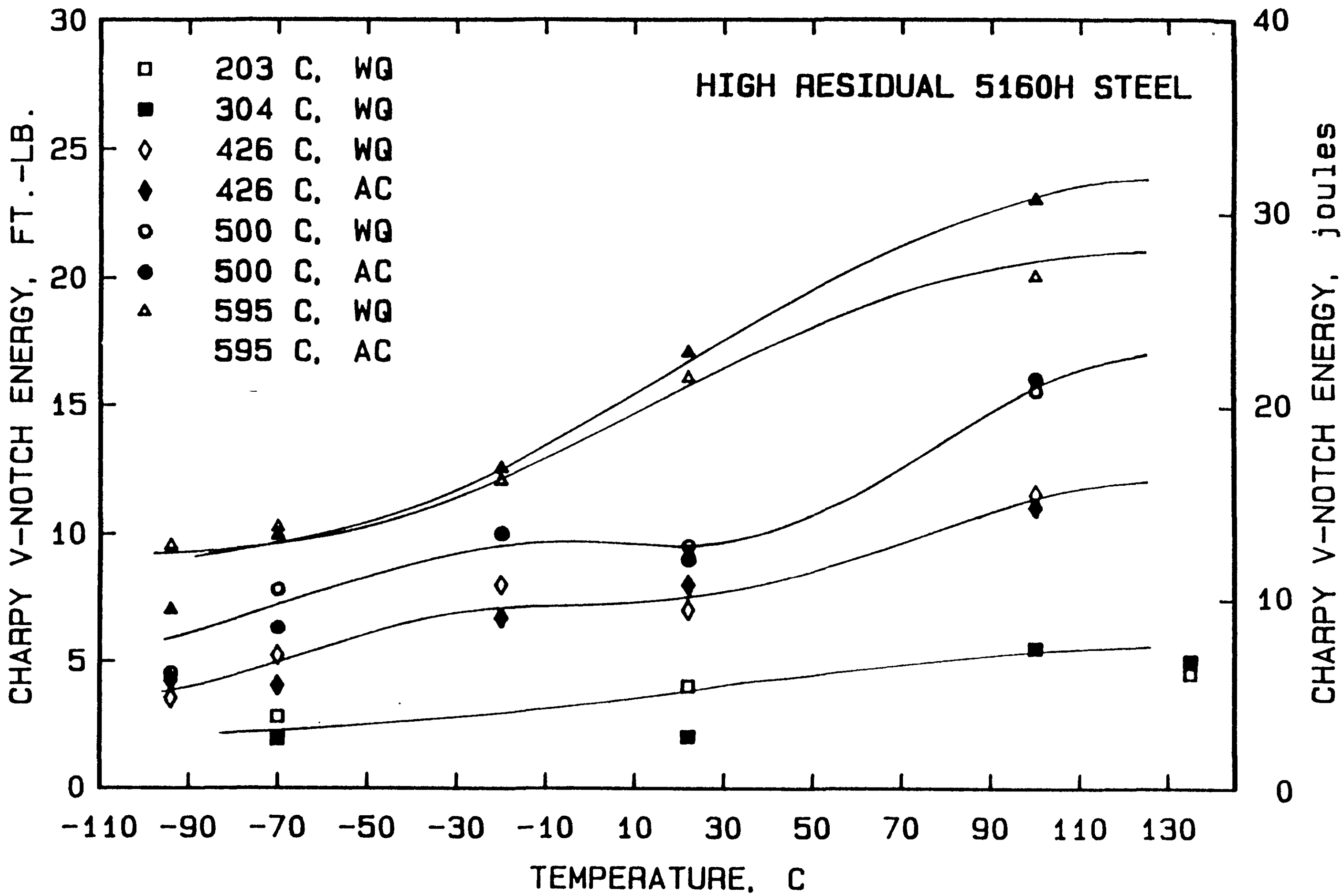

Figure 3.6 Subsize Charpy V-notch impact energy as a function of testing temperature for different tempering conditions for high-residual 5160H steel.

insignificant effect on impact toughness. The effect of the residual alloy content is observed by comparing Figures 3.5 and 3.6.

Figure 3.6 presents the corresponding transition curves for the high-residual material. This material shows transition curves similar to those presented in Figure 3.5. However, the upper-shelf energy levels and the room temperature impact energy values for the high- residual material are lowered for a specific tempering condition. For example, for a tempering condition of 595 °C/WQ the low-residual material has an upper-shelf energy level of 36.6 J (27 ft-lb), and a room temperature impact energy of 29.7 J (21.9 ft-lb); while the corresponding values for the high-residual material are 31.2 J (23 ft-lb) and 23.1 J (17 ft-lb), respectively. The same applies for the other tempering temperatures. These observations, indicate that as the residual alloy content increases the transition curves shift to higher temperatures (higher transition temperature), which in turn implies an embrittlement of the material as shown in the Charpy V-notch data discussed in Section 1.3.

Impact toughness as measured by the sub-size Charpy impact energy at room temperature is tabulated in Table 3.4 and is plotted as function of tempering temperature in

TABLE: 3.4 Room Temperature Sub-Size Charpy V-Notch Impact Toughness for Low and High Residual 5160H Steel.

Tempering Condition °C/Cooling	Low Residual J	Low Residual ft-lb	High Residual J	High Residual ft-lb
204/WQ	5.2, 5.4	3.8, 4.0	5.4, 6.1	4.0, 4.5
304/WQ	7.9, 9.5	5.8, 7.0	2.7, 3.2	2.0, 2.3
426/WQ	11.5, 13.6	8.5, 10.0	10.9, 11.5	8.0, 8.5
426/AC	12.2, 12.2	9.0, 9.0	9.5, 13.6	7.0, 10.0
500/WQ	21.7, 21.0	16.0, 15.5	12.9, 13.6	9.5, 10.0
500/AC	20.3, 21.0	15.0, 15.5	12.2, 13.7	9.0, 10.1
595/WQ	32.5, 29.8	24.0, 22.0	23.1, 21.8	17.0, 16.1
595/AC	29.7, ---	21.9, ---	21.7, ---	16.0, ---

Figures 3.7 and 3.8 for the low- and high-residual, respectively. The impact energy for the low-residual steel in Figure 3.7 shows a continuously increasing trend with tempering temperature. There is no observed variation in the curve at 500°C which would be expected in temper embrittled materials. However, the high-residual material exhibits a decrease of impact energy at 304 and at 500°C as shown in Figure 3.8. In this figure, a general reduction of impact toughness, compared with the low-residual material, is observed, i.e., for a tempering condition of 500 °C/WQ, the impact energy for the low-residual steel is 20.3 J (15 ft-lb) while that one of the high-residual steel is 12.2 J (9 ft-lb). A similar reduction of impact energy is observed for the other tempering conditions.

Reduction of the impact toughness values discussed above suggests that steel 5160H with a high-residual content is susceptible to temper embrittlement. It is important to note that the residual content is within the AISI specifications range for this grade of steel. On the other hand, the low-residual steel seems not to show TE.

The fracture toughness of each material was also evaluated and the results are summarized in Tables 3.5 and

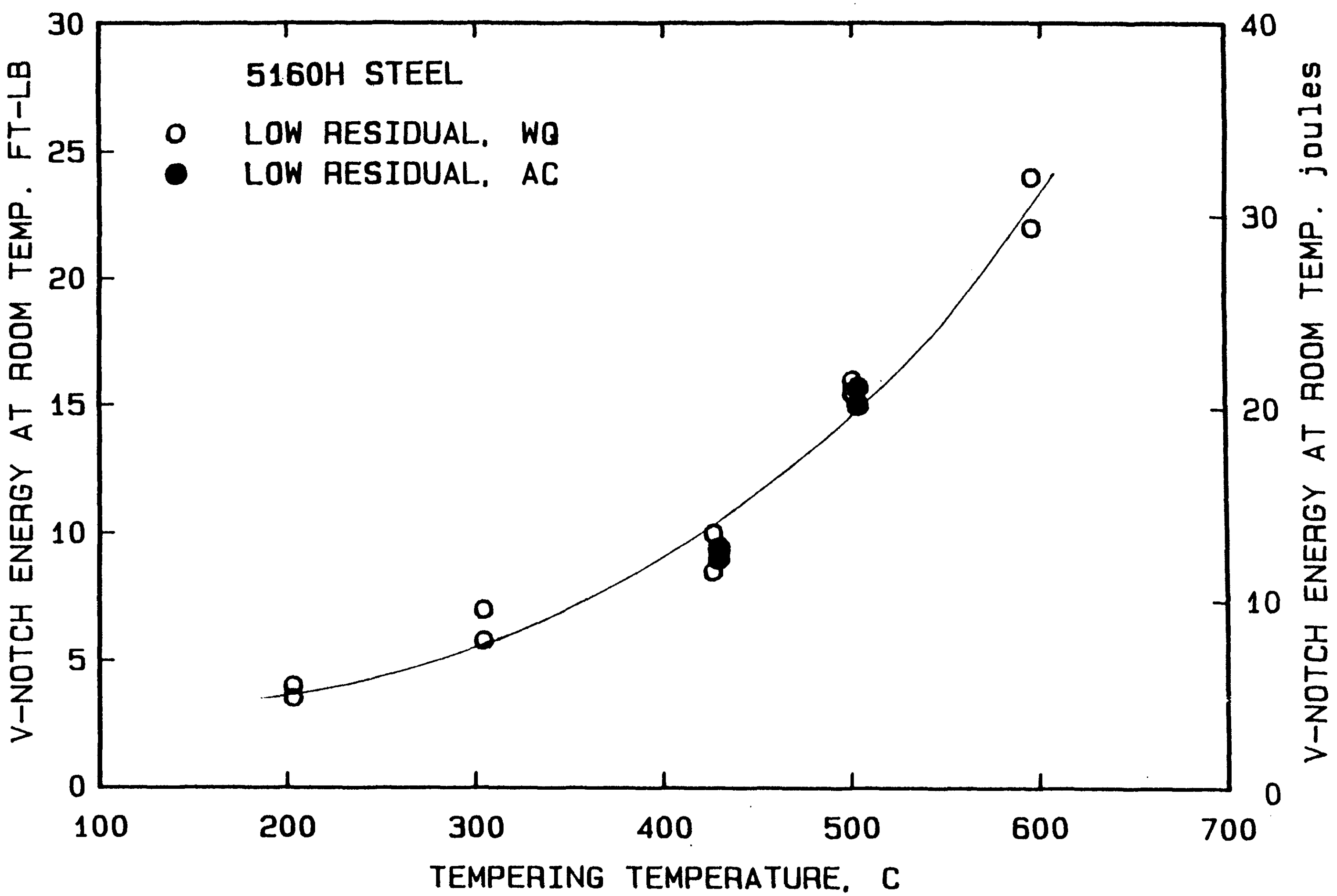

Figure 3.7 Room temperature subsize Charpy V-notch energy as a function of tempering temperature for low-residual 5160H steel.

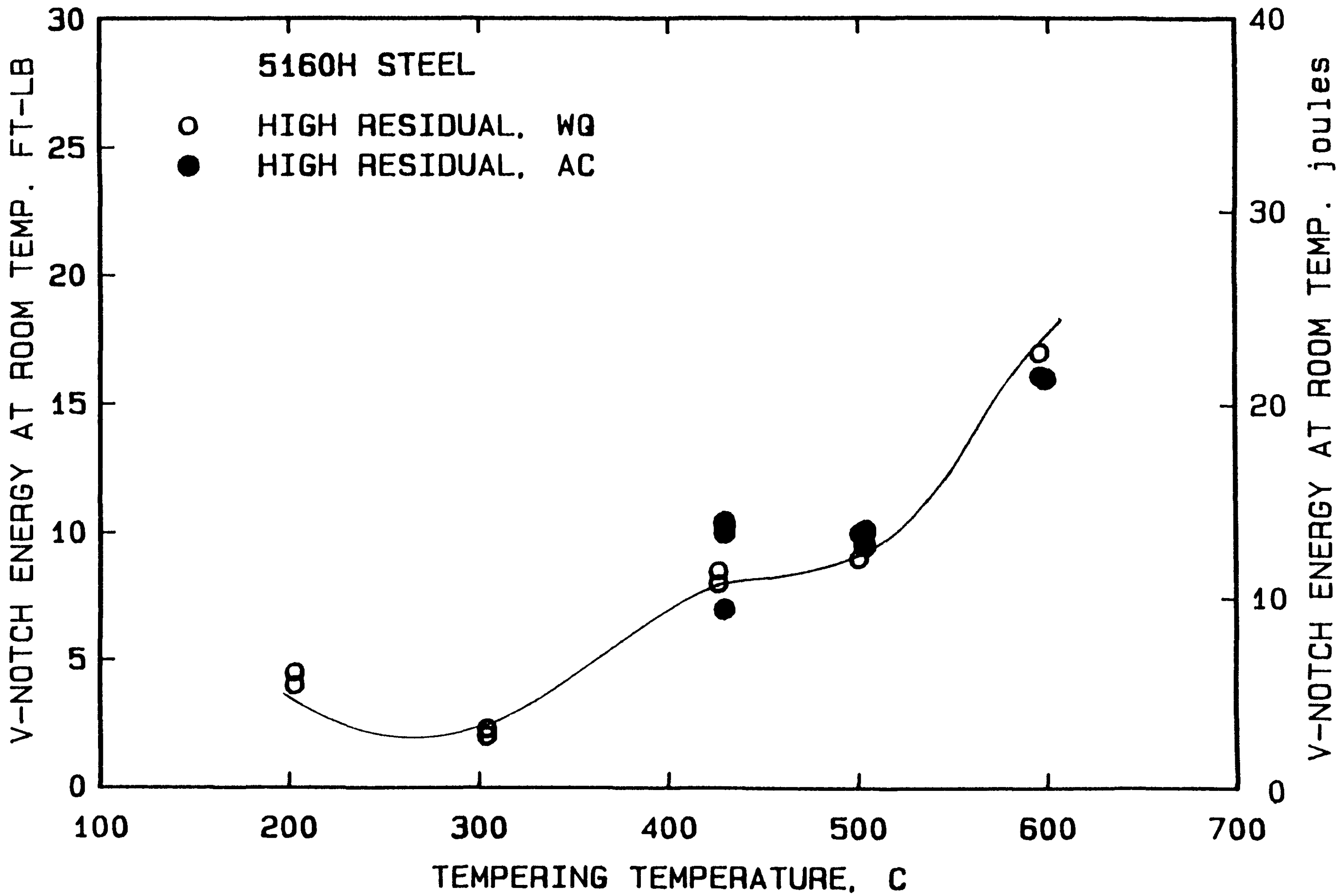

Figure 3.8 Room temperature subsize Charpy V-notch energy as a function of tempering temperature for high-residual 5160H steel.

3.6. Figures 3.9 and 3.10 show the variation of fracture toughness, at room temperature, as a function of tempering temperature for the low- and high-residual materials respectively. Fracture toughness for the low-residual material (Figure 3.9) continuously increases with an increase in tempering temperature. This is expected since as the tempering temperature increases, the ductility of the material increases, which in turn increases the resistance of the material to crack propagation and the critical crack size for final failure (28). This effect of tempering temperature on critical crack-size will be discussed in an analysis of fracture-surface appearance in section 3.2.2.

The high-residual material also exhibit an increasing trend of fracture toughness with increasing tempering temperature as shown in Figure 3.10. For all tempering temperatures the toughness of the high-residual steel is slightly lower than for the low-residual steel. This small reduction of fracture toughness contrasts with the significant reduction of impact toughness discussed previously. This observation of a small decrease in toughness, agrees with previous investigations in which it is shown that fracture toughness, at room temperature, can not be used to determine embrittlement in steels (53).

TABLE 3.5: Room-Temperature Fracture Toughness Values for Low Residual 5160H Steel.

Tempering Condition °C/Cooling	P_{max}/P_Q	$2.5(K_Q/Y_s)^2$ mm	in	K_{Ic} MPa $m^{1/2}$	Ksi $in^{1/2}$
204/WQ	1.03	.69	.027	32.3	29.4
	1.07	.56	.022	29.2	26.54
	1.06	.33	.0129	22.3	20.32
304/WQ	1.099	.43	.017	25.7	23.39
	1.13	.38	.15	25.1	22.75
	1.03	.84	.033	30.3	27.5
426/WQ	1.04	5.59	.22	78.4	71.34
	1.04	5.84	.23	79.8	72.49
	1.02	4.83	.19	72.3	65.68
	1.05	5.59	.22	78.3	71.2
426/AC	1.03	5.59	.22	78.0	70.92
	1.03	5.84	.23	78.9	71.68
	1.04	5.59	.22	78.4	71.29
500/WQ	1.07	14.99	.59	101.0	91.83
	1.04	14.99	.59	101.1	91.93
	1.09	14.48	.57	98.9	89.88
500/AC	1.09	14.48	.57	98.0	89.09
	1.105	13.72	.54	95.9	87.22
	1.08	14.22	.56	97.7	88.84
595/WQ	1.18	32.00	1.26	114.8	104.35
	1.12	26.67	1.05	112.1	101.90
	1.11	35.05	1.38	120.6	109.6
595/AC	1.12	31.24	1.23	114.3	103.9
	1.15	30.73	1.21	113.2	102.9

TABLE; 3.6 Room-Temperature Fracture-Toughness for High Residual 5160H Steel.

Tempering Condition °C/Cooling	P_{max}/P_Q	$2.5(K_Q/Y_s)^2$ mm	in	K_{Ic} MPa $m^{1/2}$	Ksi $in^{1/2}$
204/WQ	1.08	.43	.017	25.7	23.36
	1.07	.41	.016	25.0	22.4
	1.08	.38	.015	24.1	22.1
304/WQ	1.02	.33	.013	22.8	20.7
	1.05	.43	.017	21.6	19.6
	1.05	.38	.015	25.0	22.7
426/WQ	1.05	4.83	.19	72.4	65.77
	1.0	4.57	.18	70.1	63.71
	1.0	4.83	.19	72.5	65.87
	1.0	4.57	.18	69.5	63.15
426/AC	1.07	4.3	.017	67.4	61.29
	1.03	4.3	.017	68.5	62.32
	1.08	3.8	.15	65.0	59.04
500/WQ	1.19	14.99	.59	100.3	91.20
	1.098	11.43	.45	87.5	79.54
	1.08	12.19	.48	90.2	81.98
500/AC	1.108	12.19	,48	90.5	82.34
	1.07	12.19	.48	91.3	83.04
595/WQ	1.105	26.92	1.06	105.4	95.80
	1.12	26.42	1.04	104.1	94.62
595/AC	1.11	26.67	1.05	103.1	93.69
	1.13	25.38	.99	101.6	92.42

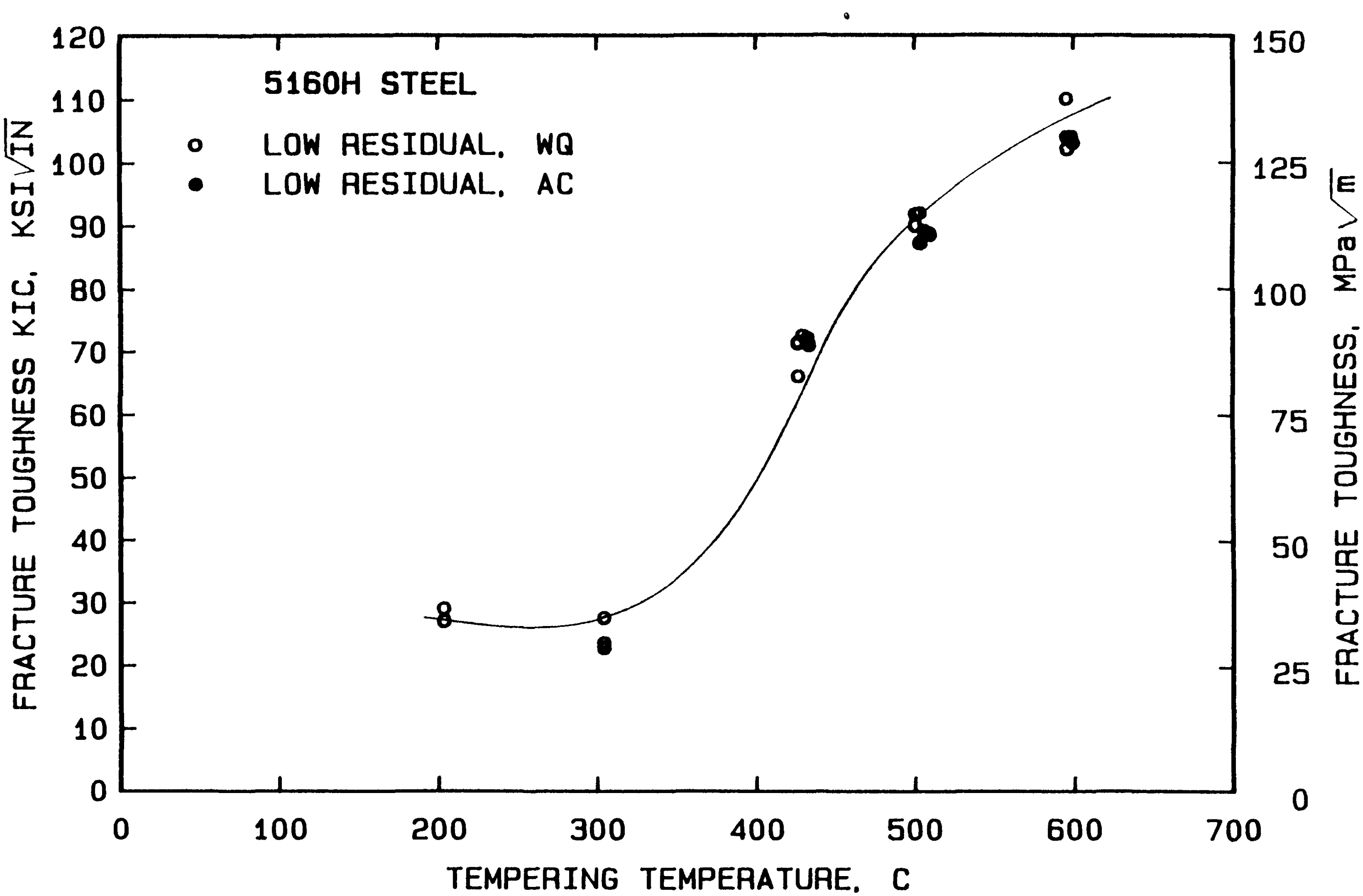

Figure 3.9 Variation of fracture toughness with tempering temperature for low-residual 5160H steel.

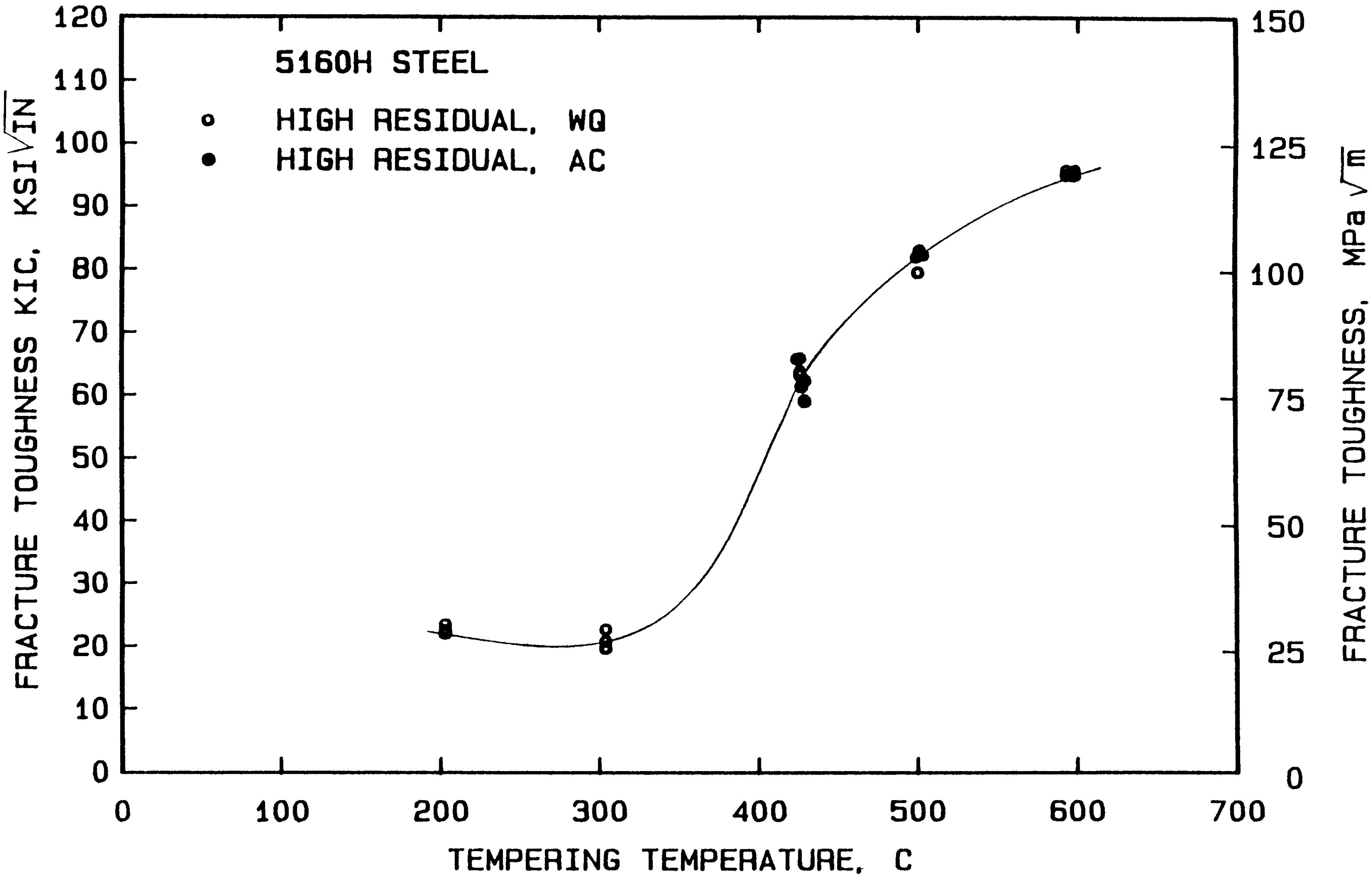

Figure 3.10 Variation of fracture toughness with tempering temperature for high-residual 5160H steel.

Materkowski (54) proposed that an increase of fracture toughness in temper-martensite-embrittled steel can be explained by the presence of a ductile region at the fracture surface of CT specimens. In his investigation of TME in 4340 steel, he observed a small region of ductile fracture at the interface between the fatigue and the overload regions. He hypothesized that during the K_{IC} static test the stress intensity factor builds up slowly and eventually causes plastic flow at the crack tip. When the K_{IC} value reaches a critical value, the material within the plastic zone at the crack tip fails by ductile rupture. Then, the material outside the plastic zone sees a sudden increase of the stress intensity factor and fails in a brittle manner. Thus, the measured K_{IC} values are those required for initial fracture at the plastic zone at the tip of the crack and are not the values for fracture at the overload region of the specimen (54).

Testing for fracture toughness at subzero temperatures gave fracture surfaces which did not show the plastic zone responsible for the high K_{IC} value at room temperature (54). It is suggested that during subzero testing the yield strength is high enough to avoid plastic deformation at the crack tip (54). Results from fracture toughness tests at -26°C with the 5160H steel evaluated in this thesis agree with the interpretation of Materkowski (54); such results are given in Table 3.7. The high-residual material at low temperature shows a larger decrease in K_{Ic} values, compared with those values for the low-residual steel. This reduction of toughness agrees with the adverse effect of sulfur, phosphorus and tin pointed out in Section 1.5.2. It is important to note that

such reduction of K_{Ic} is greater for the 500 °C/AC tempering condition, which is the condition presenting the largest reduction in endurance limit. The values in Table 3.7 are values from single-sample tests at each temperature, but they give evidence of the effect of the stretch zone on the increased K_{Ic} values at room temperature of embrittled steels. Fracture surfaces of CT specimens tested at room and subzero temperature are shown in section 3.2.2.

3.2 Microscopy

Microstructures were evaluated with light microscopes and fracture surfaces were analyzed with both light and scanning electron microscope techniques.

3.2.1 Metallography. The microstructure obtained after the different tempering conditions was the expected

TABLE 3.7: Fracture-Toughness Values for Low and High Residual5160H Steel Tested at -26 °C.

Tempering Condition °C/Cooling	Test Temperature -26°C		22°C	
	MPa $m^{1/2}$	Ksi $in^{1/2}$	MPa $m^{1/2}$	Ksi $in^{1/2}$
HIGH RESIDUAL				
426/AC	47.9	43.5	67.1	61
500/WQ	85.3	77.5	92.4	84
500/AC	76.3	69.4	91.3	83
595/WQ	80.2	80.7	104.5	95
595/AC	80.2	72.9	102.3	93
LOW RESIDUAL				
500/WQ	85.3	77.5	100.1	91
500/AC	97.6	88.7	96.8	88
595/WQ	113.6	103.3	115.5	105
595/AC	104.4	94.9	113.3	103

tempered-martensite microstructure, with hardness values between 62 and 38 HRc as shown in Figure 3.1.

The results of a special etching technique (3, 11, 12) designed to preferentially etch prior austenite grain boundaries which have been modified due to high local concentration of elements which contribute to temper embrittlement are shown in Figure 3.11. Figure 3.11 includes light micrographs of samples etched in a picric acid and water solution for 15 minutes (Figure 3.11a) and for 40 minutes (Figure 3.11b) along with an SEM micrograph (Figure 3.11c) of the same sample shown in Figure 3.11b. The high-residual material develops grooves along the prior austenite grain boundaries. This preferential attack by picric acid solution at the prior austenite grain boundaries was shown (3, 11, 12) to be a characteristic feature in tempered embrittled steels. A comparison of the micrographs in Figures 3.11a and b shows the effect of etching time on groove width; as the etching time increases the groove width increases which is a phenomena expected in temper embrittled steels (11). These grooves which appeared as dark lines in light micrographs, are readely apparent in the SEM micrograph shown in Figure 3.11c of the sample etched for 15 minutes.

A comparison of the response of the low and

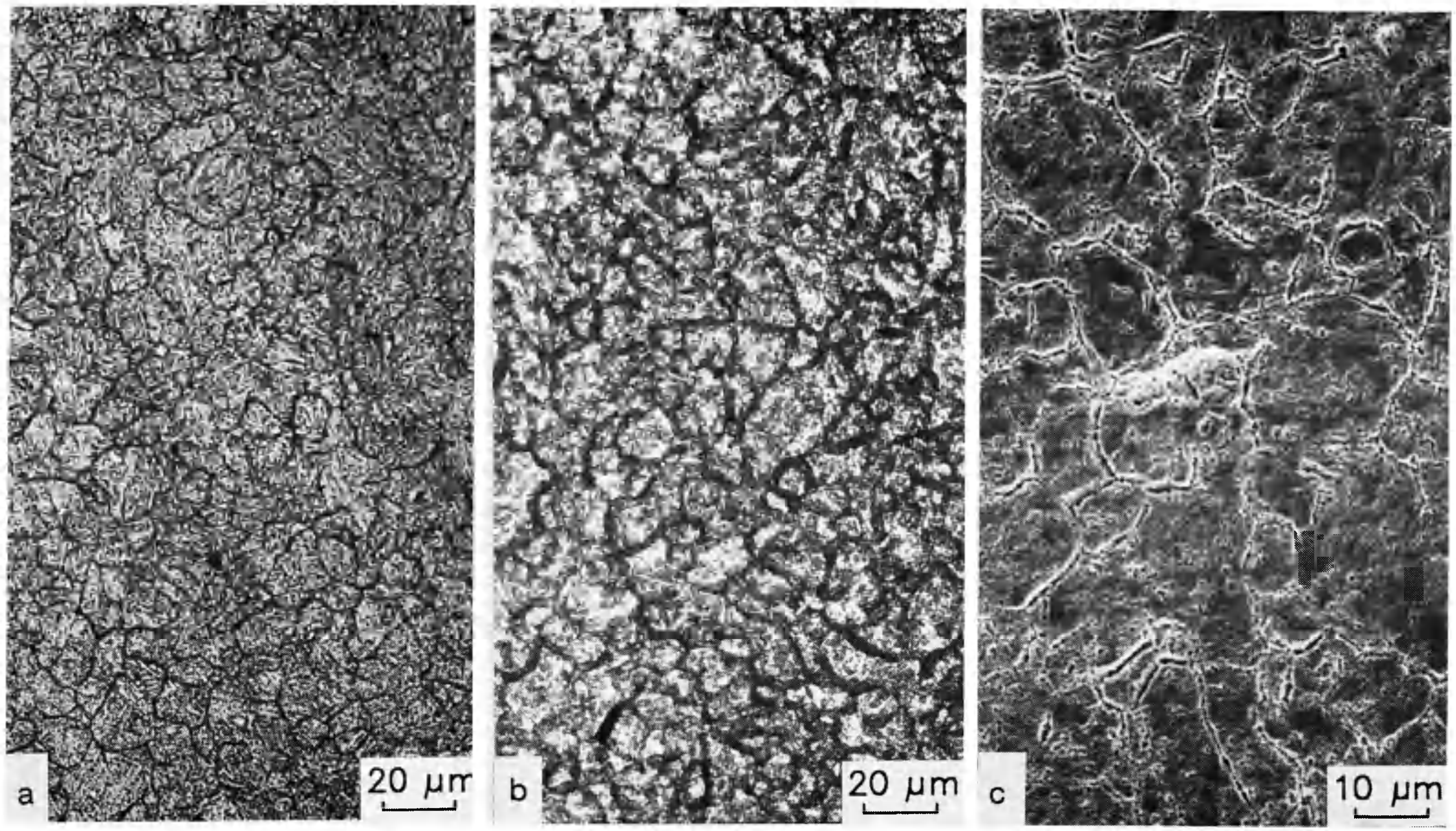

Figure 3.11 Light and SEM micrographs of high-residual 5160H steel tempered at 500°C and etched in picric acid solution. a) steel etched for 15 min., 500X, b) steel etched for 40 min., 500X, c) SEM micrograph of sample in a), 100X.

high-residual materials to the picric acid solution is shown in Figure 3.12. After the same etching time (15 minutes) the low-residual material, Figure 3.12a, does not develop grooves as did the high-residual material, Figure 3.12b. This observation agrees with the results from impact toughness and subzero fracture toughness tests discussed earlier. It seems apparent then, that susceptibility of 5160H steel to TE increases as the residual alloy content increases.

3.2.2 Fractography. The fracture surfaces of fatigue, impact, and fracture toughness samples were evaluated with fractographic techniques which utilized both light and sacnning electron microscopy. Figures 3.13 through 3.18 document fracture-surface features of specimens tested in fatigue. Macrographs of fatigue-sample fracture surfaces of low-residual steel tempered at 204, 426, and 595°C are shown in Figures 3.13a, 3.13b, and 3.13c, respectively. In both examples the fatigue cracks nucleated at the upper surface of the sample, which is the face subjected to the highest tensile stresses during the test. The crack propagation mode, however, differs between the two tempering conditions as discussed below.

In Figure 3.14 schematic representations of the fracture surfaces shown in Figure 3.13 are presented to

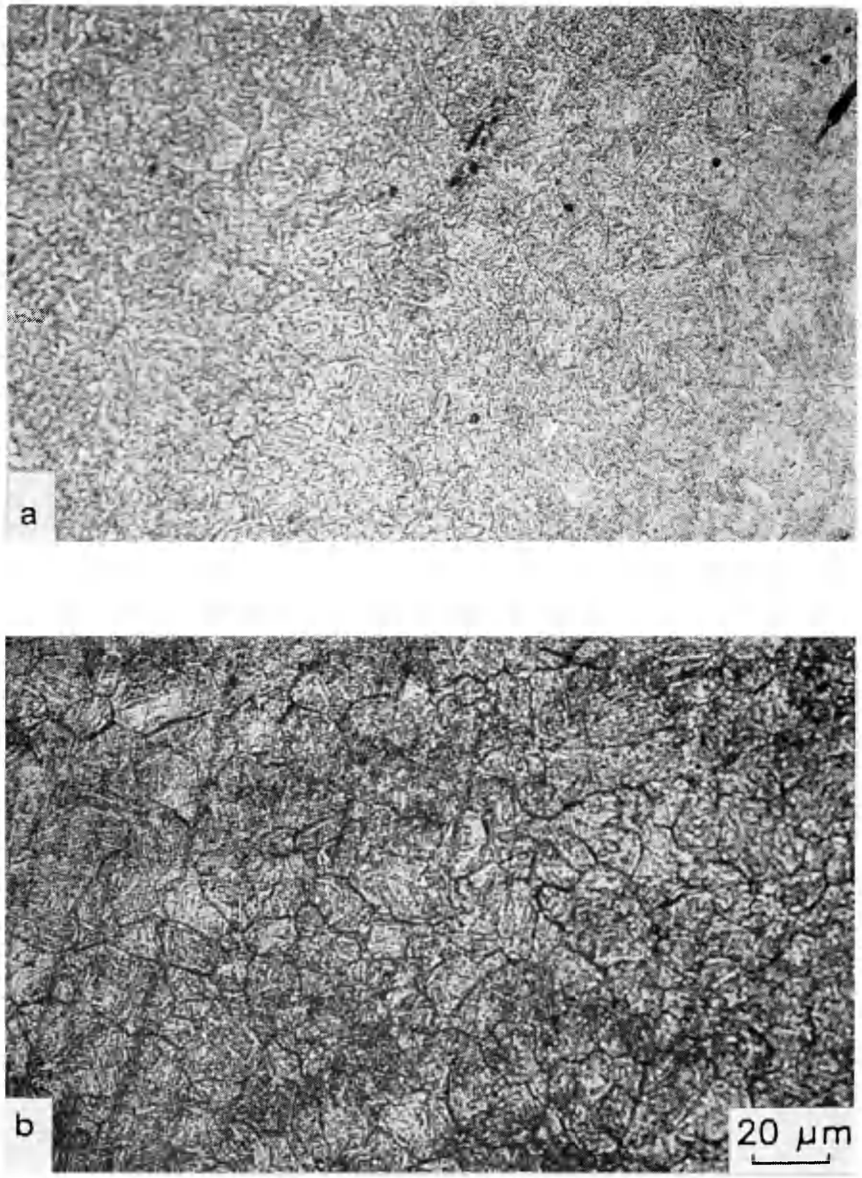

Figure 3.12 Light micrograph of steel 5160H tampered at 426°C and etched in picric acid solution for 15 min. a) low residual, 500X, b) high residual, 500X.

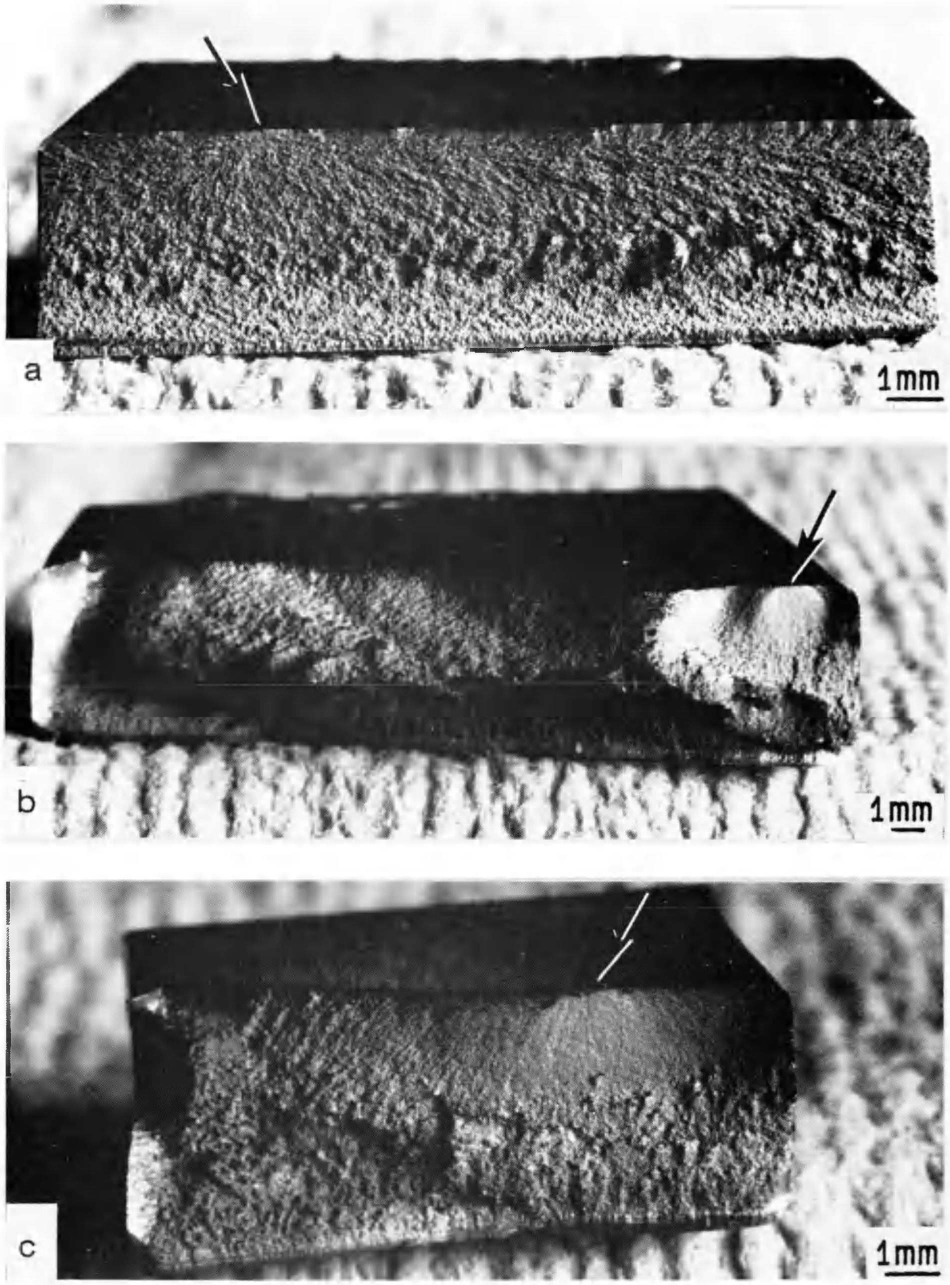

Figure 3.13 Macrographs of fracture surfaces of fatigue samples from low-residual 5160H steel tempered at: a) 204°C, b) 426°C, and c) 595°C. Initiation site indicated by arrow.

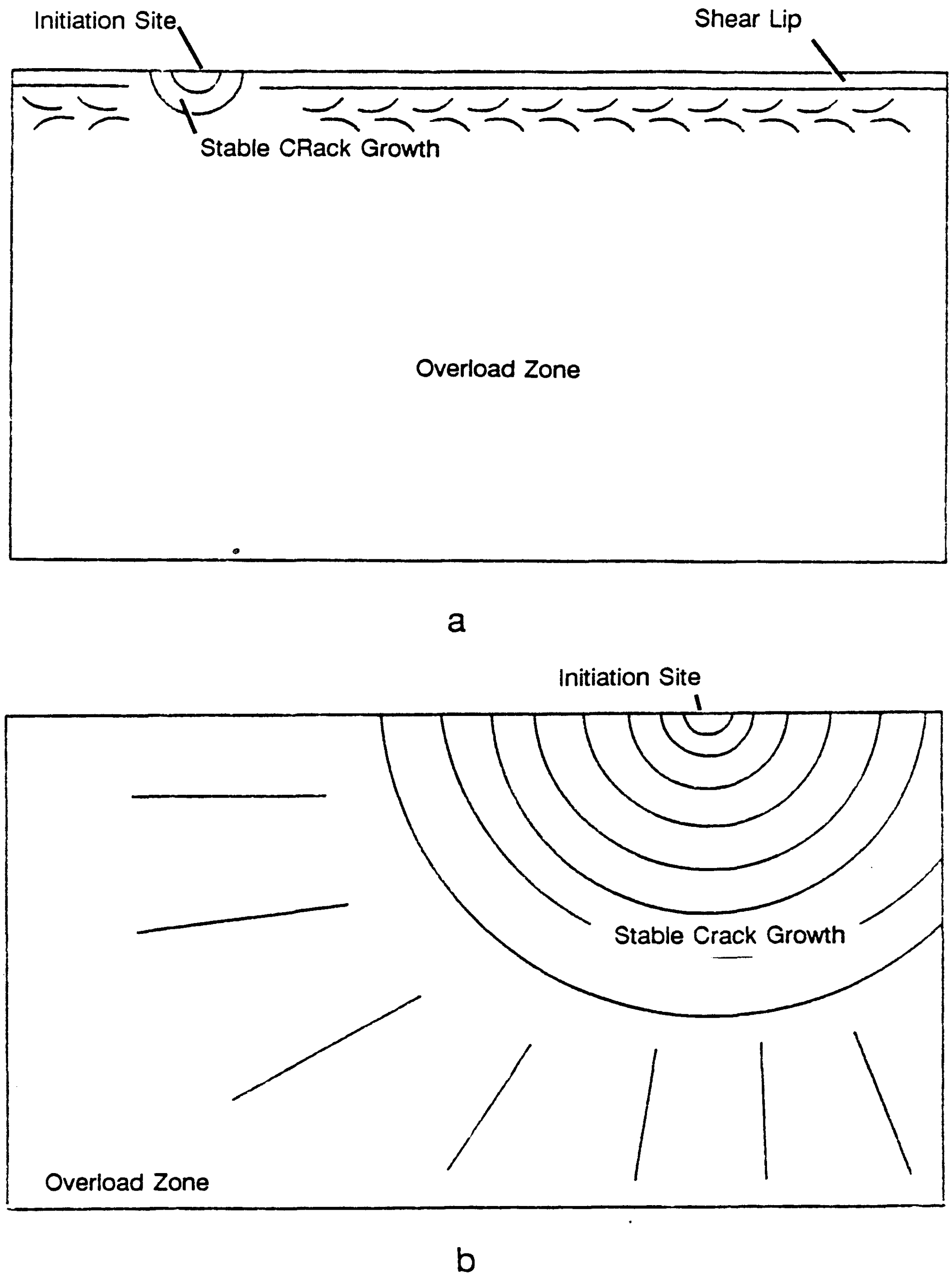

Figure 3.14 Schematic representation of fracture surfaces of a) high- and b) low-strength 5160H fatigue samples.

illustrate the effect of tempering temperature, and thus strength, on the macroscopic fracture behavior of the low-residual steel. Initiation and stable-crack-growth zone (55) are identified. In the high strength sample, a small fatigue crack nucleated a critical-size crack which first propagated parallel to the top surface (as evidenced by chevron lines shown in Figure 3.14a and evident in 3.13a). Once the crack reaches the sample edges, the crack grows unstably through the remaining section of the sample. This fracture surface appearance can be explained by considering the stress state gradient in between the surface and sub-surface layers. On bending, a maximum tensile stress develops at the surface layers of the material and then reduces its magnitude towards the center of the sample. Because of the low toughness and high strength of the sample tempered at 204°C, the surfaces layers fail in tension in a similar way in which a plate fails when loaded in tension; chevron lines, and a shear lip along the free surface develop as shown schematically in Figures 3.14a. Once the crack propagates along the surface, the remaining section fails by over load in a brittle mode.

The fracture mechanism in the lower strength material (tempered at 595 °C) is schematically shown in Figure

3.14b. The fatigue cracks in the samples tempered at 426°C and above (to produce hardness between 52-38 HRc), propagates in an stable manner, from the initiation point radially outwards producing a "half moon" crack morphology. Once the crack reaches a critical size, the remaining material fails by overload in a ductile mode as shown in Figures 3.14b and 3.13b.

The effect of tempering temperature on the size of the stable fatigue-crack growth zone, can be discerned by comparing Figures 3.13a, 3.13b and 3.13c. The size of the stable fatigue-crack zone increases as the tempering temperature increases. The increase in critical crack size agrees with the increase of toughness of the material as the tempering temperature increases as shown in Figure 3.9. It is important to note, however, that under a given constant-amplitude stress range, most of the useful cyclic life of a component is expended on growing sub-critical fatigue cracks and not during the stable growth of the crack. Thus, although the high hardness material (tempered between 204 and 426 °C) has an smaller critical crack size, it is expected to have a longer cyclic life. These observations point out the importance of surface hardness and agree with results presented previously in Figure 3.4.

Microscopic analysis, on the SEM, provides information on the crack initiation sites. Figure 3.15 shows three micrograph of initiation sites in the low and the high-residual steels. Fatigue cracks initiated, in most cases, at particles near the surface. These particles served as stress concentration points at which microcracks develop and which eventually initiated fatigue cracks. Chemical composition of the particles indicated that they were inclusions containing aluminum, silicon, magnesium, and manganese. Silicates, refractory inclusions, and hard oxides particles are known to serve as crack initiation sites (1, 38, 31, 37).

In a few of the samples fatigue cracks seemed to have initiated and propagated along grain boundaries. As an example, Figure 3.16 shows a micrograph of the fracture surface of a fatigue sample tempered at 204°C. In this micrograph, the crack may have initiated at a grain boundary on the surface and propagated intergranularly through a few grains, and then propagated in a stable manner through the grains in a transgranular manner (identified as zone II in Figure 1.5). It is important to point out that this was not the predominant mode of crack initiation and propagation in these materials.

As a complement to the analysis of fracture surface appearance of fatigue samples, micrographs from the

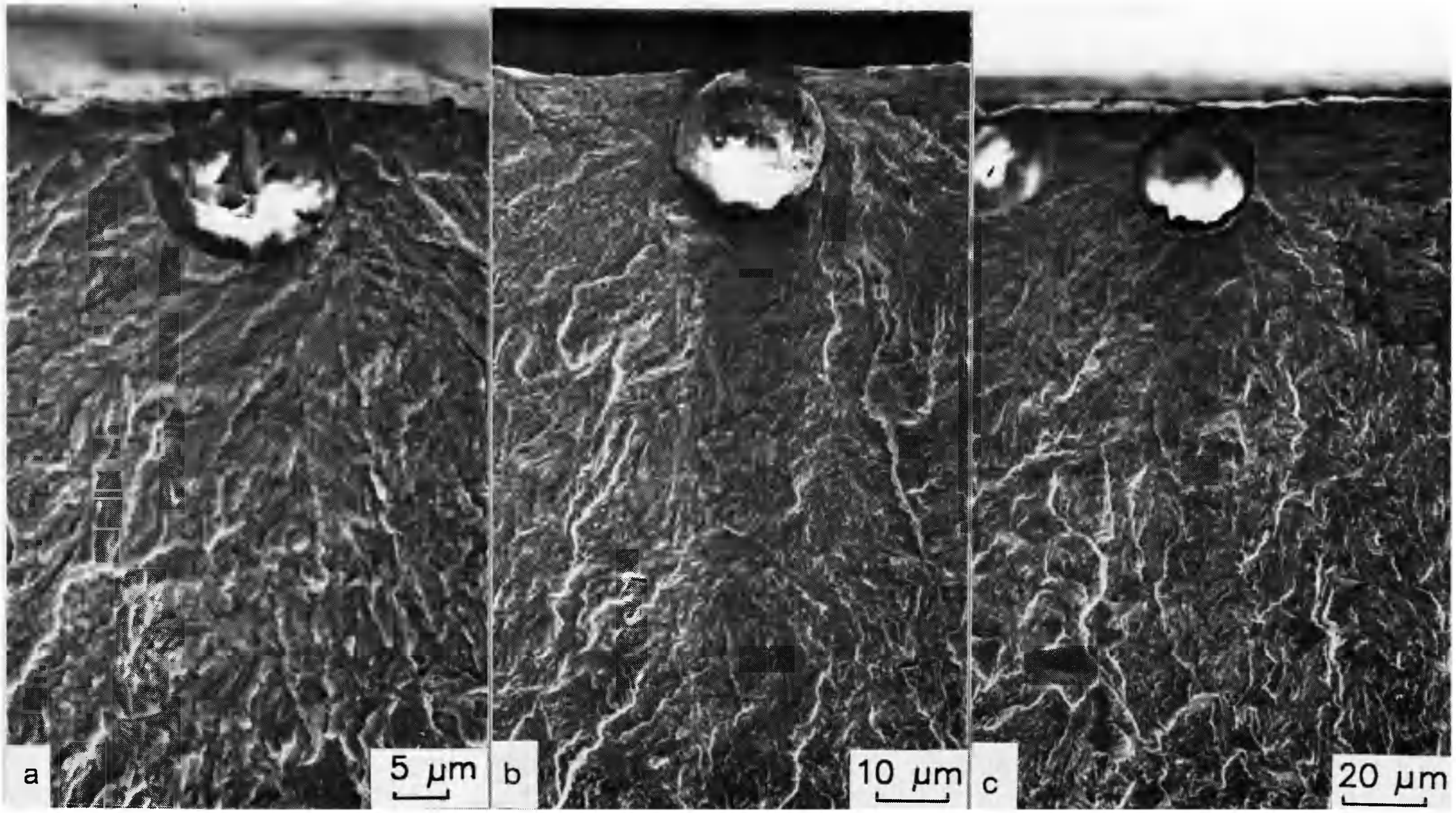

Figure 3.15 SEM micrograph of fatigue crack initiation sites in samples of 5160H steel. a) low-residual steel tempered at 595°C, 1500X, b) high-residual steel tempered at 595°C, 1200X, c) high-residual steel tempered at 480°C, 650X.

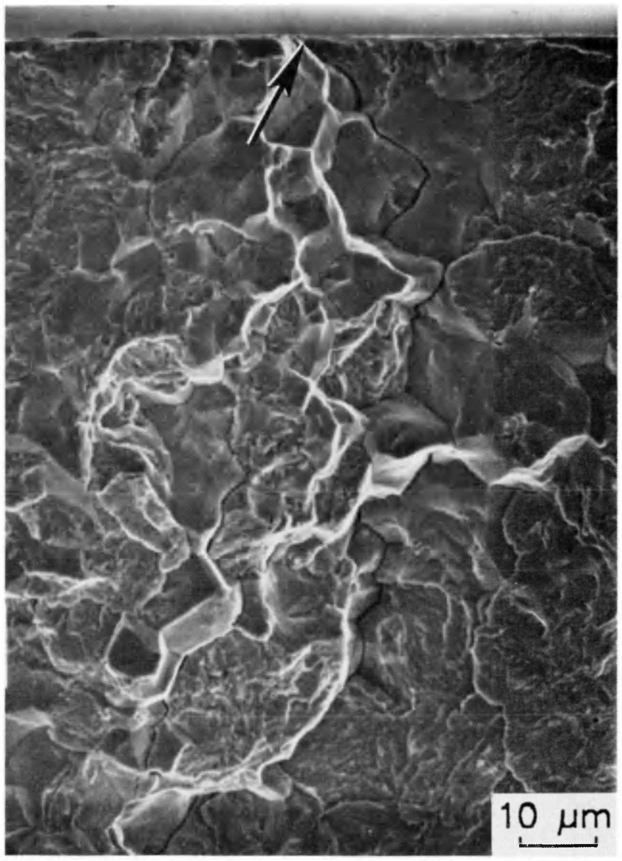

Figure 3.16 SEM micrograph of fatigue crack initiating at grain boundaries in a fatigue sample of 5160H steel tempered at 204°C, 1000X.

stable-crack growth zone and from the overload zone have been included. Figure 3.17a shows the fracture surface appearance in the stable crack growth zone (zone II). In all cases, the fracture mechanism in this zone is a transgranular fracture mode. As expected, however, the characteristic fatigue striations of this zone are not present in these steels because of their high hardness (33, 34). Figure 3.17b shows the fracture appearance at the overload zone. In this zone the material fails in a ductile manner by void nucleation and coalescence. Chemical composition on the SEM showed that particles present in these zones contained sulfur and manganese.

Fracture surface appearance of impact toughness samples are presented in Figures 3.18 through 3.21. To provide a basis for analysis, Figure 3.18 shows a schematic representation of the fracture zones in a Charpy sample of ductile material. In this figure, three zones are identified: 1) the fibrous zone which is a zone of stable fracture produced by a triaxial tensile stress state, and is characterized by a slow crack growth; 2) the radial zone which is a zone also of stable crack propagation but is characterized by a crack growth rate faster than that one in the fibrous zone; 3) the third zone is the shear lip which is an unstable-crack-growth zone, characterized by a ductile fracture involving void coalescence and a fast

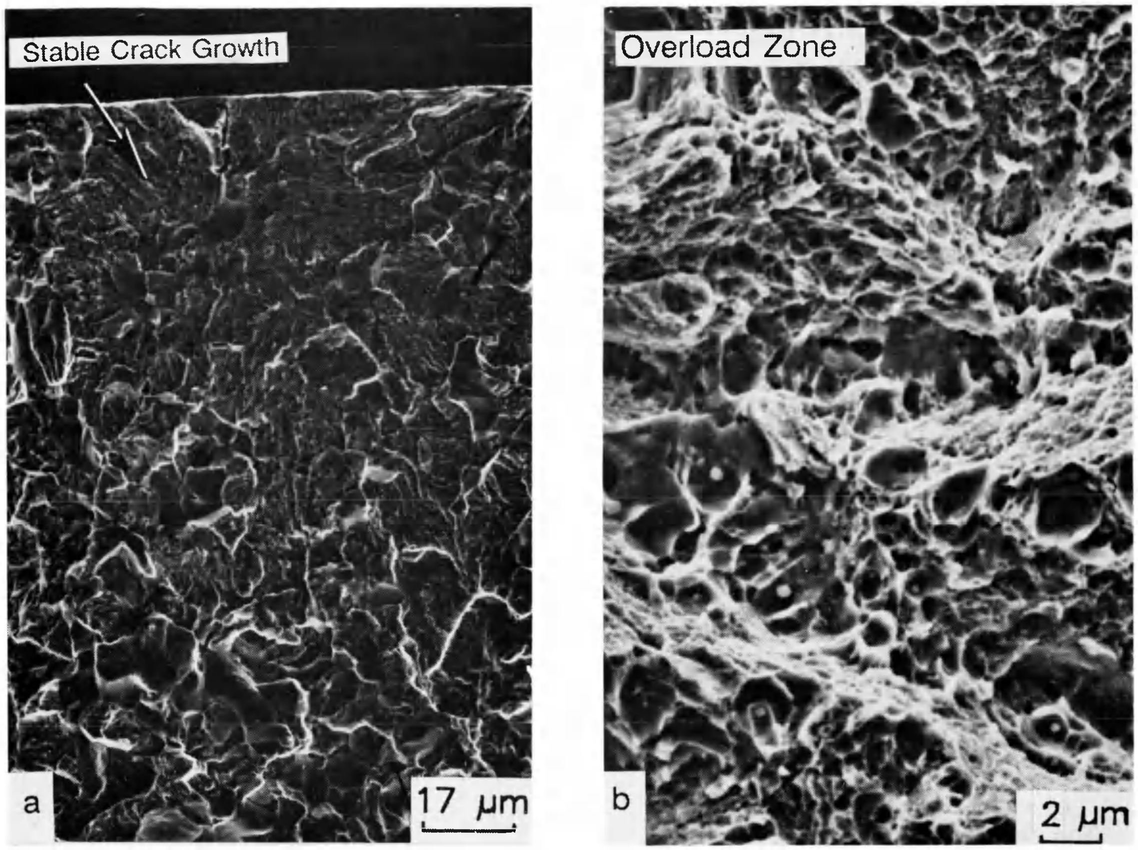

Figure 3.17 SEM micrographs of fracture appearance from fatigue samples of 5160H steel. a) stable-crack growth zone, 600X, b) overload zone, 3500X.

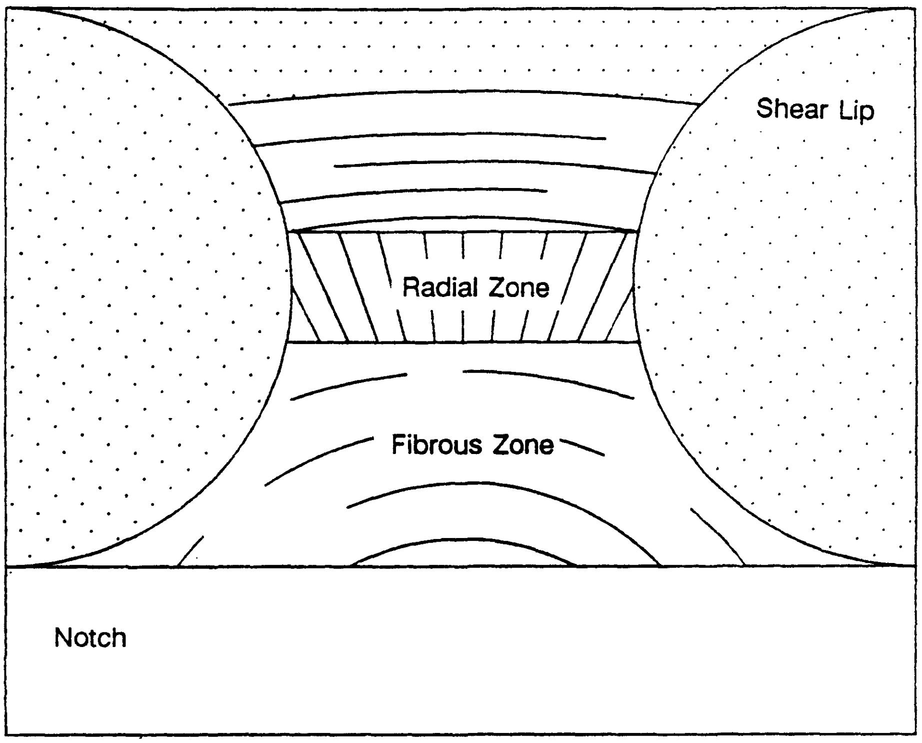

Figure 3.18 Schematic representation of fracture zones in a charpy V-notch sample of ductile material.

crack growth rate (56).

The transition curves obtained from impact toughness tests (Figures 3.5 and 3.6) can be correlated to the percent-distribution of the fracture zones described in Figure 3.18. The amount of shear lip present on the fracture surface gives an indication of the amount of absorbed energy during fracture; the amount of absorbed energy increases as the amount of shear lip increases. Figures 3.19 and 3.20 are examples of the variation of fracture surface appearance as a function of test temperature and of tempering temperature.

Figure 3.19 show fracture surface macrographs from Charpy samples of the low-residual material, in the 595 °C/WQ tempering condition, as a function of test temperature. Figure 3.19a is a macrograph of the fracture surface after testing at a low temperature (-94 °C); In this sample the fracture surface shows a very small shear lip and a basically flat-brittle fracture. This agrees with the low absorbed-impact energy at -94°C (test Temperature) in Figure 3.5. Figure 3.19c is a macrograph of the fracture surface after testing a at high temperature (100 °C); In this sample the fracture surface resembles the ductile fracture described in Figure 3.18 and agrees with a higher absorbed-impact energy at 100°C (test

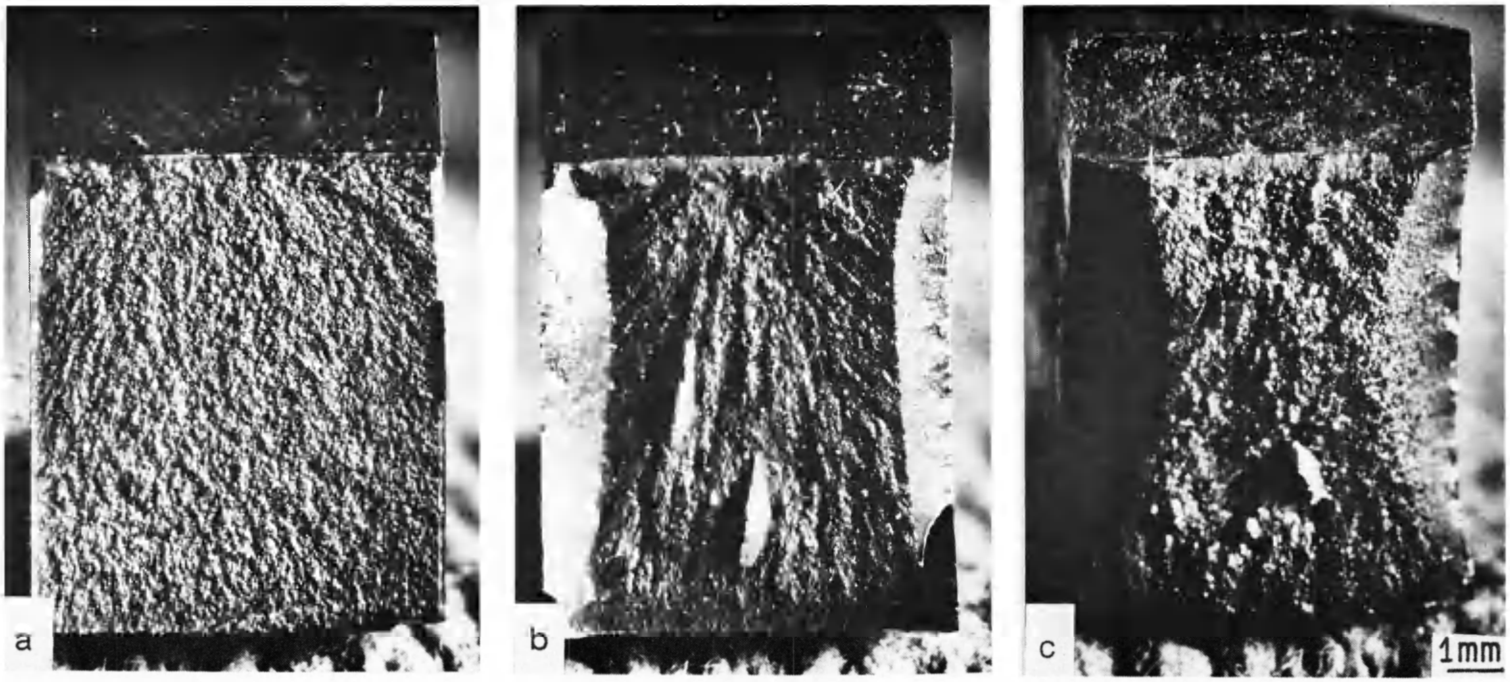

Figure 3.19 Macrographs of fracture surfaces from Charpy samples of low residual 5160H steel tempered at 595°C and tested at a)-94°C, b) 22°C, c) 100°C.

temperature) in Figure 3.5. Figure 3.19b is after testing at an intermediate temperature (22 °C) and shows a fracture surface appearance in between those shown in Figures 3.19a and 3.19c

A similar change in fracture surface appearance takes place as the tempering temperature increases. Figure 3.20 shows macrographs of fracture surface appearance from Charpy samples of the low-residual material, tested at 22°C, as a function of tempering temperature. Figure 3.20a is a macrograph of the fracture surface after tempering at a low temperature (204 °C); in this case the fracture is a brittle fracture which agrees with the low absorbed-impact energy at 204°C (tempering temperature) in Figure 3.7. Figure 3.20c is a macrograph of the fracture surface after tempering at a high temperature (595 °C); the fracture is a ductile fracture which agrees with the higher absorbed energy at 595°C (tempering temperature) in Figure 3.7.

A relative comparison of the amount of ductile fracture then, gives an indication of the embrittlement of a material. Figure 3.21 shows the percent of ductile fracture at room temperature (taken as the amount of shear lip present on the surface) as a function of tempering temperature for the low- and high-residual steels (in the

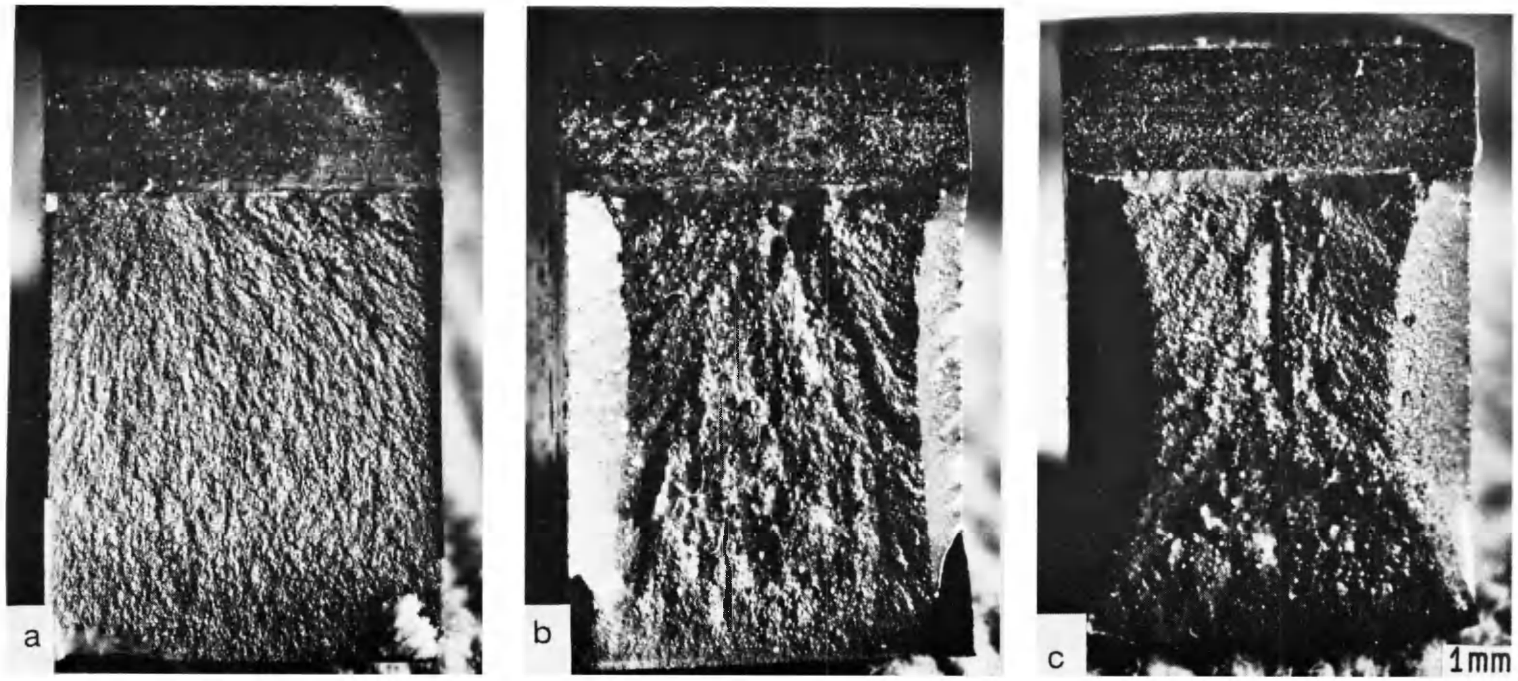

Figure 3.20 Macrographs of fracture surfaces from Charpy samples of 5160H steel tested at 22°C and tempered at a) 204°C, b) 500°C, c) 595°C.

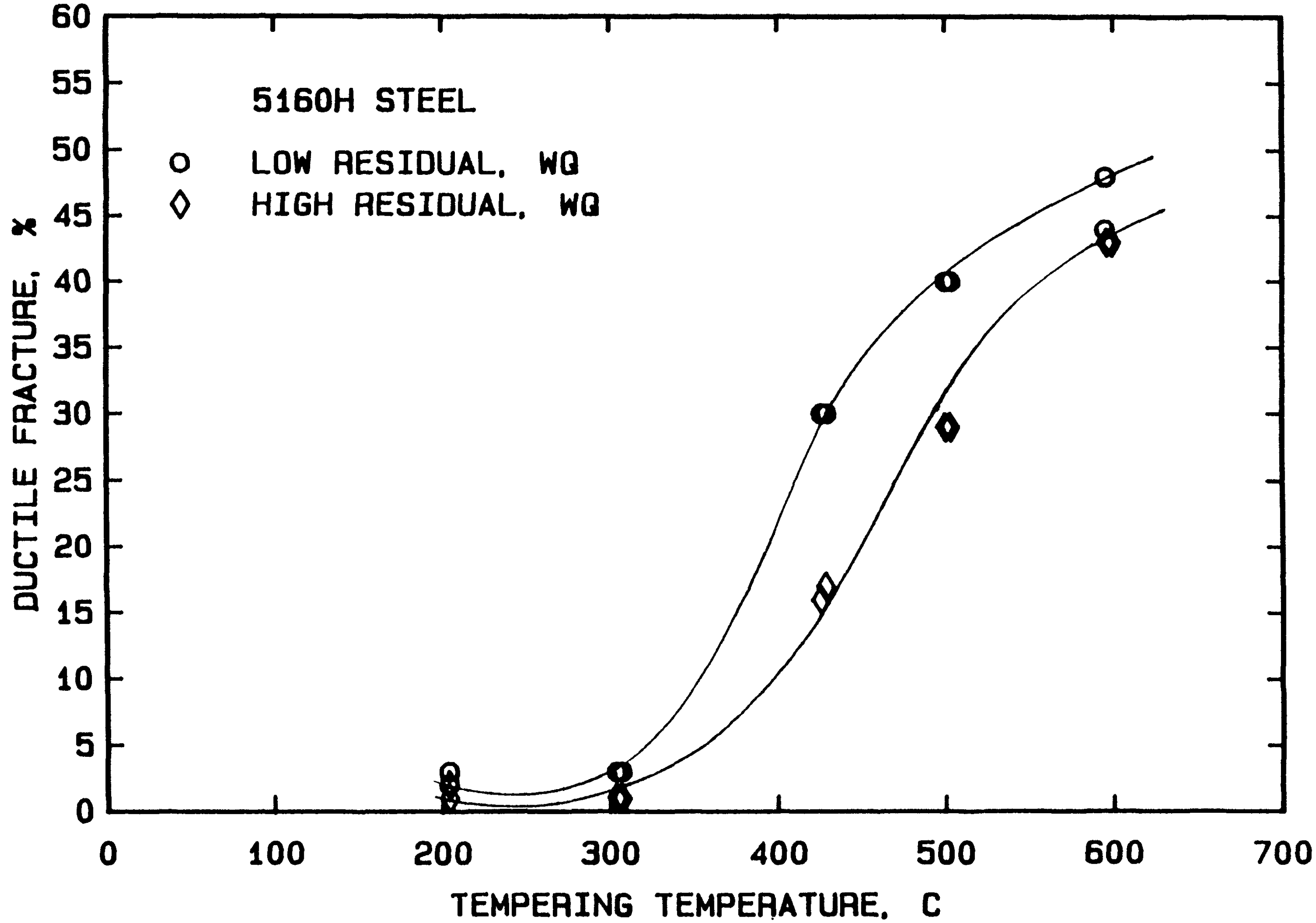

Figure 3.21 Percent ductile fracture at room temperature as a function of tempering temperature for low- and high-residual 5160H steel.

water-quenched condition). The reduction of the percent of ductile fracture agrees with the reduction of impact toughness at room temperature shown in Figures 3.7 and 3.8.

Microscopic analysis on the SEM of fracture surfaces of Charpy samples are summarized in Figure 3.22. The micrographs are taken from the middle section of the fracture zone, of samples tested at room temperature. These micrographs are presented by pairs. That is, micrographs from the low and the high residual material tempered at a give temperature correspond to a pair. For example, Figure 3.22a shows micrographs for the low- and high-residual material tempered at 304°C.

Analysis of fracture surface appearance of the low-residual material as a function of tempering temperature, indicates a significant increase of ductile fracture as the tempering temperature increases. Figure 3.22a, for the low-residual material, shows large amounts of brittle fracture. This brittle fracture is a mixed mode between transgranular quasi-cleavage and intergranular fracture with some amount of ductile tearing. The amount of ductile fracture increases as the tempering temperature increases as is shown in Figures 3.22a through 3.22d for the low-residual material. In Figure 3.22d, the low-residual material shows a ductile fracture by void

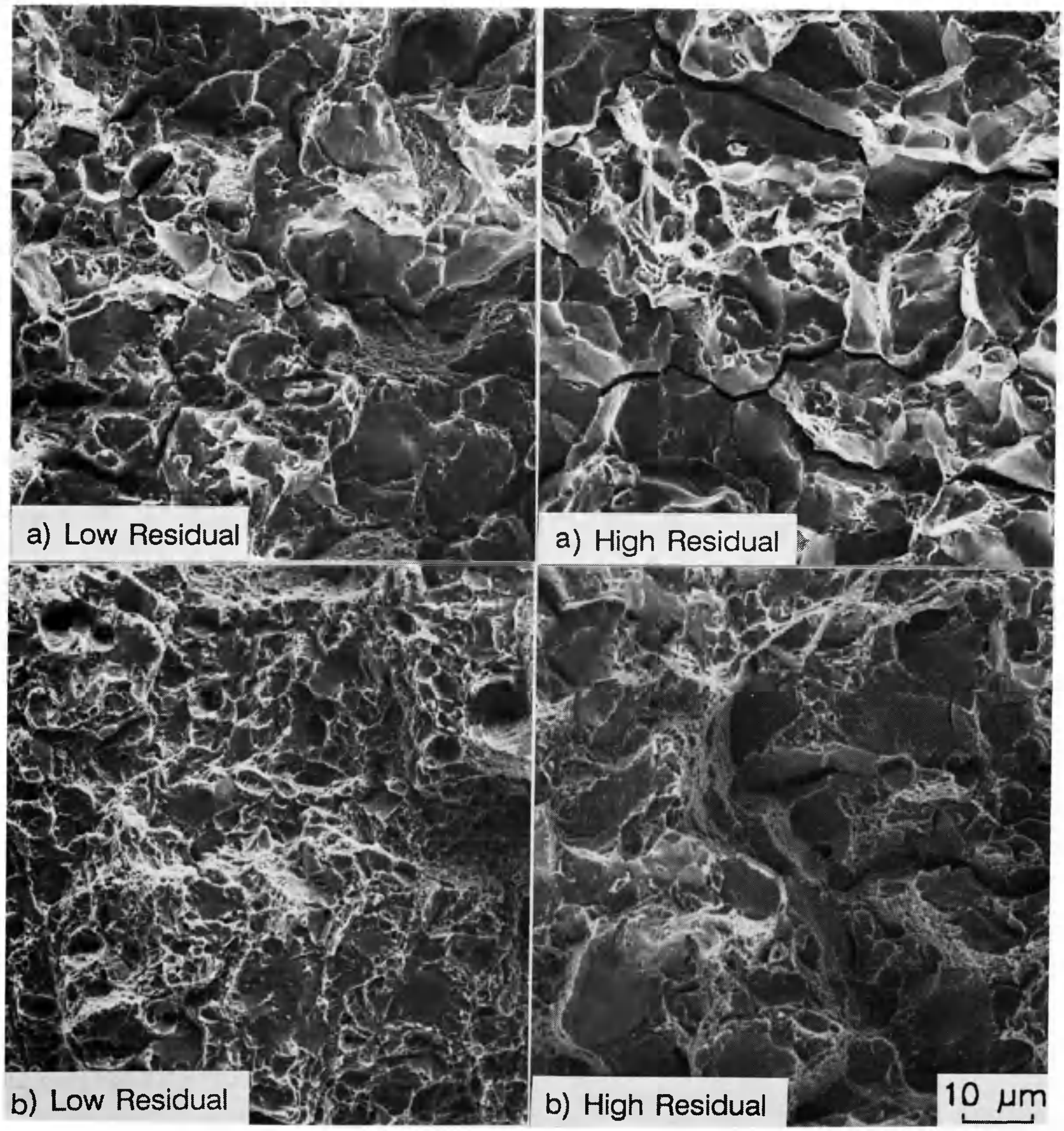

Figure 3.22 SEM micrograph pairs which compare the fracture surfaces of Charpy samples of low- and high-residual 5160H steel tested at room temperature and tempered at a) 304°C, b) 426°C, c) 500°C, and d) 595°C, 1000X.

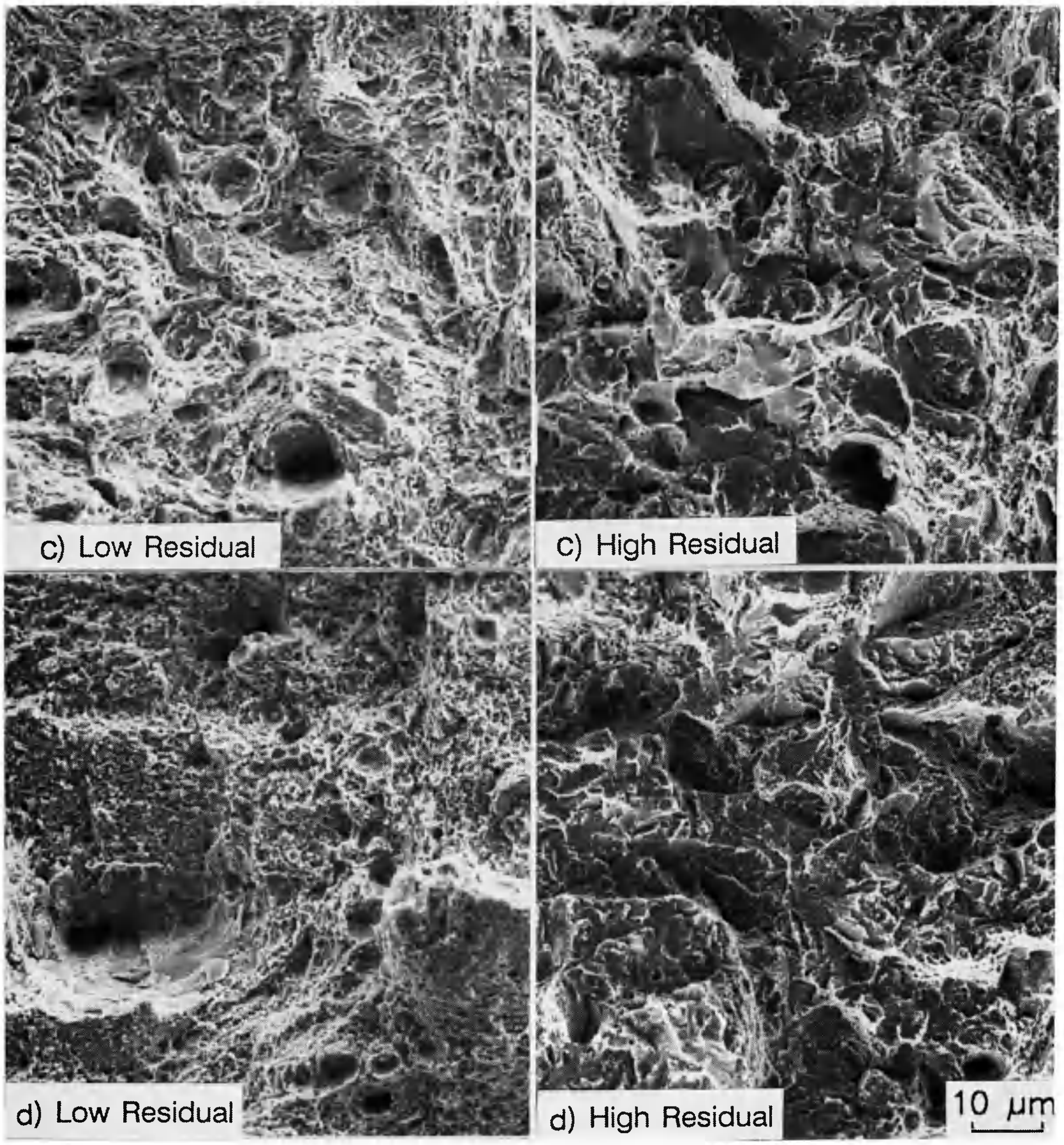

Figure 3.22 (Continued) SEM micrograph pairs which compare the fracture surfaces of Charpy samples of low- and high-residual 5160H steel tested at room temperature and tempered at a) 304°C, b) 426 °C, c) 500°C, and d) 595°C, 1000X.

coalescence.

A similar analysis of the fracture surface appearance of the high-residual material indicates that this material exhibits a larger amount of brittle fracture for the different tempering temperatures. In Figure 3.22a, for the high-residual material, an intergranular type of fracture is more apparent than in the case for the low-residual steel. The high-residual material also exhibits a higher degree of brittle fracture after tempering at 500 and 595°C in comparison to the samples of the low-residual steel after tempering at the same conditions as shown in Figures 3.22c and 3.22d. Contrary to what was expected, the type of fracture mechanism in these cases is a mixed fracture mode between transgranular quasi-cleavage and intergranular type of fracture with some ductile tearing. Temper embrittled materials, as is believed to be the case for the high-residual steel tempered at 500°C, are expected to fail by a intergranular type of fracture (1, 10, 3, 11).

A micrograph at a higher magnification from the fracture surface of the high-residual material tempered at 500°C is shown in Figure 3.23. In this micrograph, an intergranular type of fracture is evident which confirms the presence of temper embrittlement in the high-residual

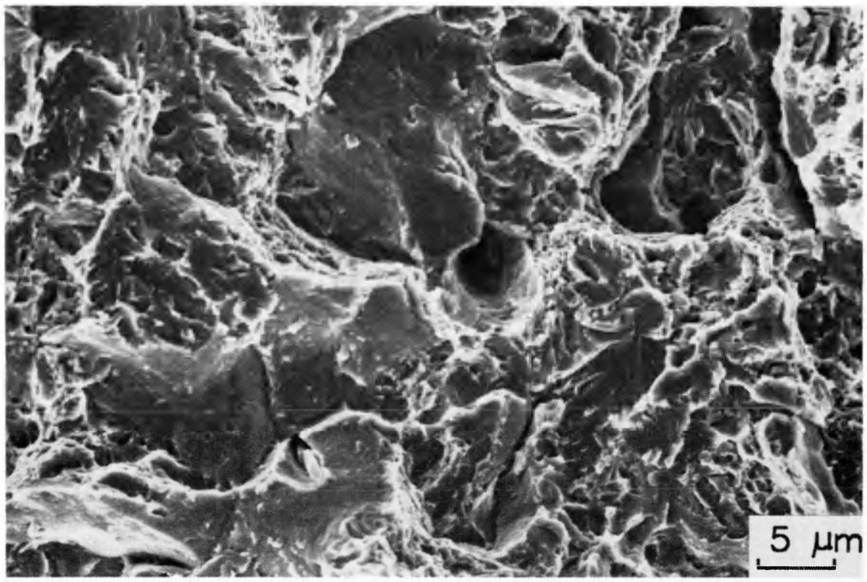

Figure 3.23 SEM micrograph of fracture surface from a Charpy sample of high-residual 5160H steel tested at room temperature and tempered at 500°C, 2000X.

material. However, a transgranular fracture, resembling a quasi-cleavage type of fracture, is also observed. It is important to point out that quasi-cleavage type of fracture is a characteristic of temper martensite embrittlement (TME) in low phosphorus steels (1). This aspect will be further discussed in Section 3.3.

Intergranular type of fracture is also observed in fatigue and fracture toughness samples. As an example of fracture surface appearance in these samples, micrographs of fatigue samples (Figure 3.24a) and fracture toughness samples (Figure 3.24b) of the high-residual material tempered at low temperatures are included. These fracture surfaces show a large degree of intergranular fracture, when high-strength materials are expected to fail by a quasi-cleavage fracture mechanism (56). Thus, the micrographs of fracture surface appearance presented in Figures 3.22, 3.23, and 3.24, indicate a general deterioration of the mechanical properties of 5160H steel as the residual alloy content increases; however, the fracture mode does not agree, in a strict way, with the expected fracture mode for TE.

Temper embrittlement of the low-residual material is not evident. The fracture surface for the impact samples tempered at 500°C (Figure 3.22c) exhibits only ductile

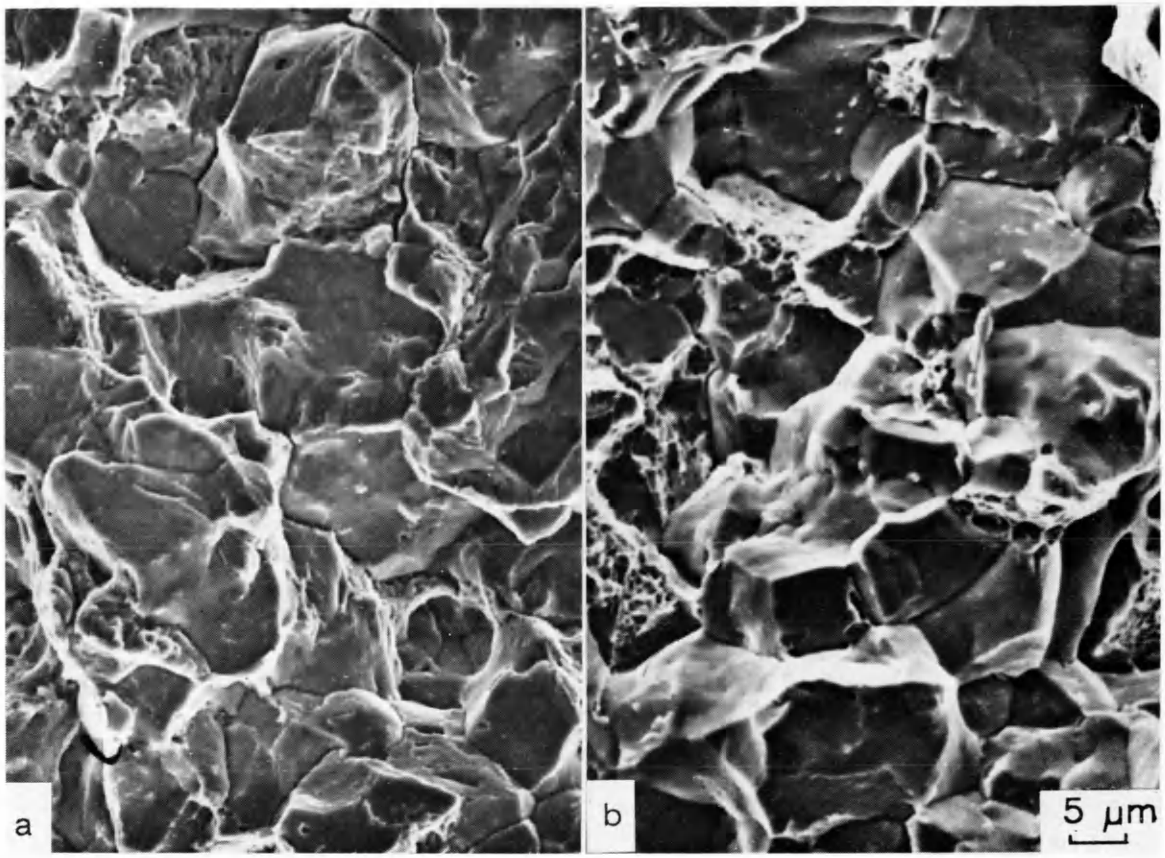

Figure 3.24 SEM micrograph of the overload zone in a) fatigue and b) CT samples of high residual 5160H steel tempered at 203 and 304°C, respectively, 1500X.

fracture, which agrees with the smooth increasing trend of impact energy at room temperature shown in Figure 3.7.

Fracture surface analysis of fracture toughness samples is presented in Figures 3.25 through 3.27. Macrographs of fracture surfaces for the low and high materials are presented in Figures 3.25a and 3.25b, respectively. In Figure 3.25b split-radial lines, which are larger in the high-residual steel, are observed on the fracture surface.

Split radial lines are common features in fracture surfaces of embrittled materials (56, 14). Split radial lines develop due to a lack of constraint at the center of the cross section of the embrittled sample. A triaxial tensile stress state develops at the mid-section of of the fatigue precrack when a CT sample is loaded in tension. This triaxial stress state is more severe than the biaxial stress state developed at the free surfaces of the sample. When the stress reaches certain value, a non-embrittled material fails and fractures in an unstable manner. But when the material is embrittled, the stress developed at the center of the sample is high enough to cause a decohesion of the material at this center point. This generates two new free surfaces within the specimens. These new free surfaces change the stress state at the

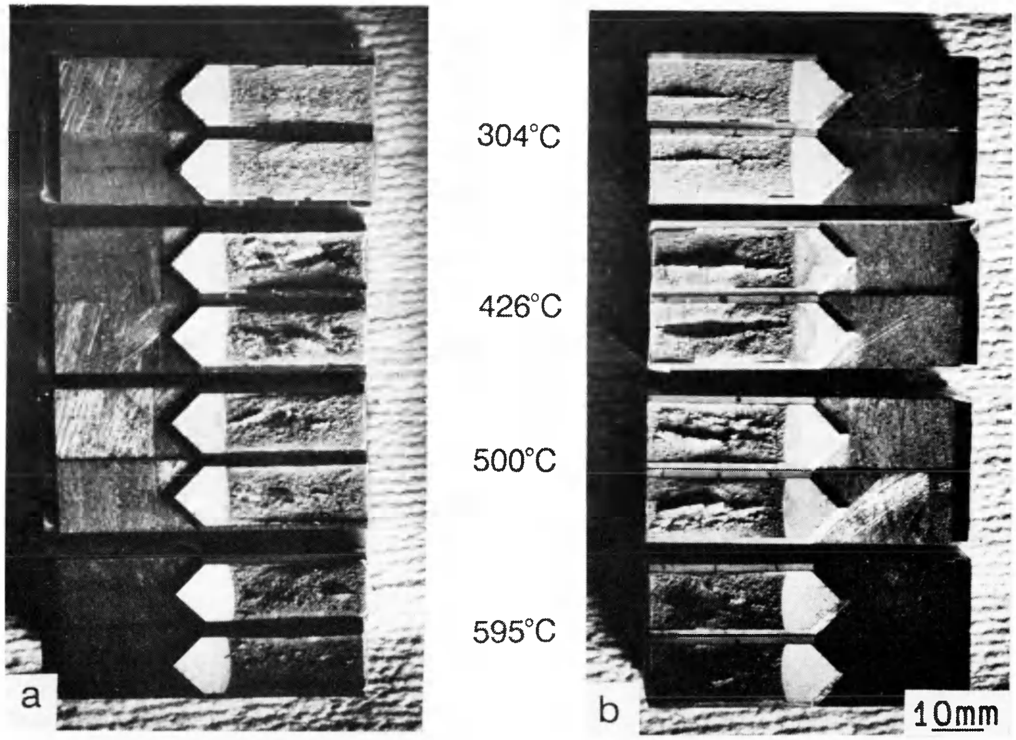

Figure 3.25 Macrographs of fracture surfaces from CT samples for the a) low- and b) high-residual 5160H steel tested at room temperature.

center, from one of triaxiality, to one of biaxiality, which, in ,turn causes the development of two shear lips at the center of the broken sample. These two extra shear lips conform the split radial line (56, 14).

Figures 3.26 and 3.27 are micrographs from fracture surfaces of fracture toughness samples. Figures 3.26a and 3.26b are micrographs of CT specimens tested at room temperature taken from the low- and the high-residual materials, respectively. These Figures illustrate the ductile transition zone referred to in Section 3.1. The ductile transition zone is the small-ductile tearing region, developed between the fatigue pre-crack zone and the overload zone as shown in the micrographs. Figures 3.27a and 3.27b include micrographs of CT samples in the same condition than those in Figure 3.26, but tested at subzero temperature. In this case, the ductile transition zone did not develop which agrees with the lower values of fracture toughness for the high-residual material tested at -26°C, values given in Table 3.7 and discussed in Section 3.1.

It is important to compare the overload zones in the low- and high-residual samples in Figures 3.26 and 3.27. While the low-residual sample presents a ductile type of fracture, the high-residual sample presents a brittle type

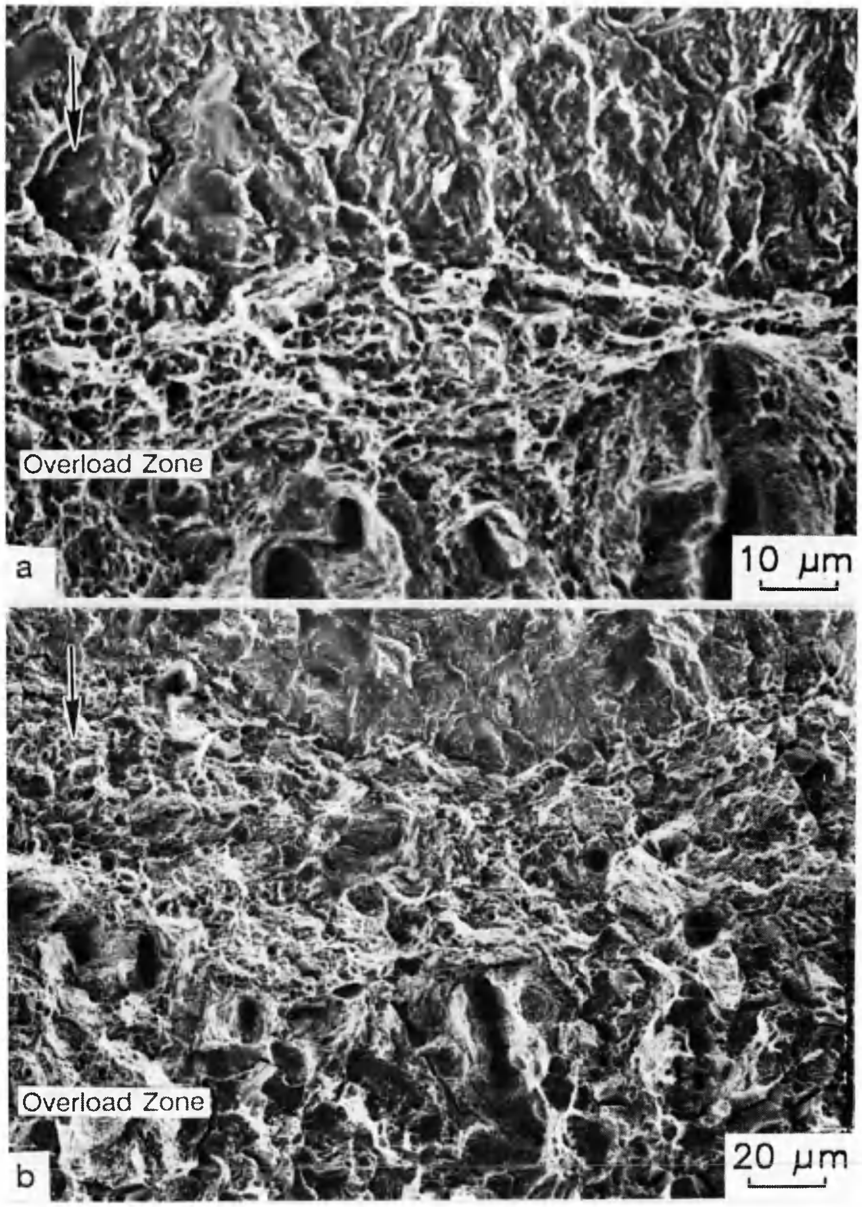

Figure 3.26 SEM micrographs showing ductile transition zones on fracture surfaces of CT samples of 5160H steel tested at room temperature. a) low residual, 1000X, b) high residual, 500X. Direction of crack propagation indicated by arrow.

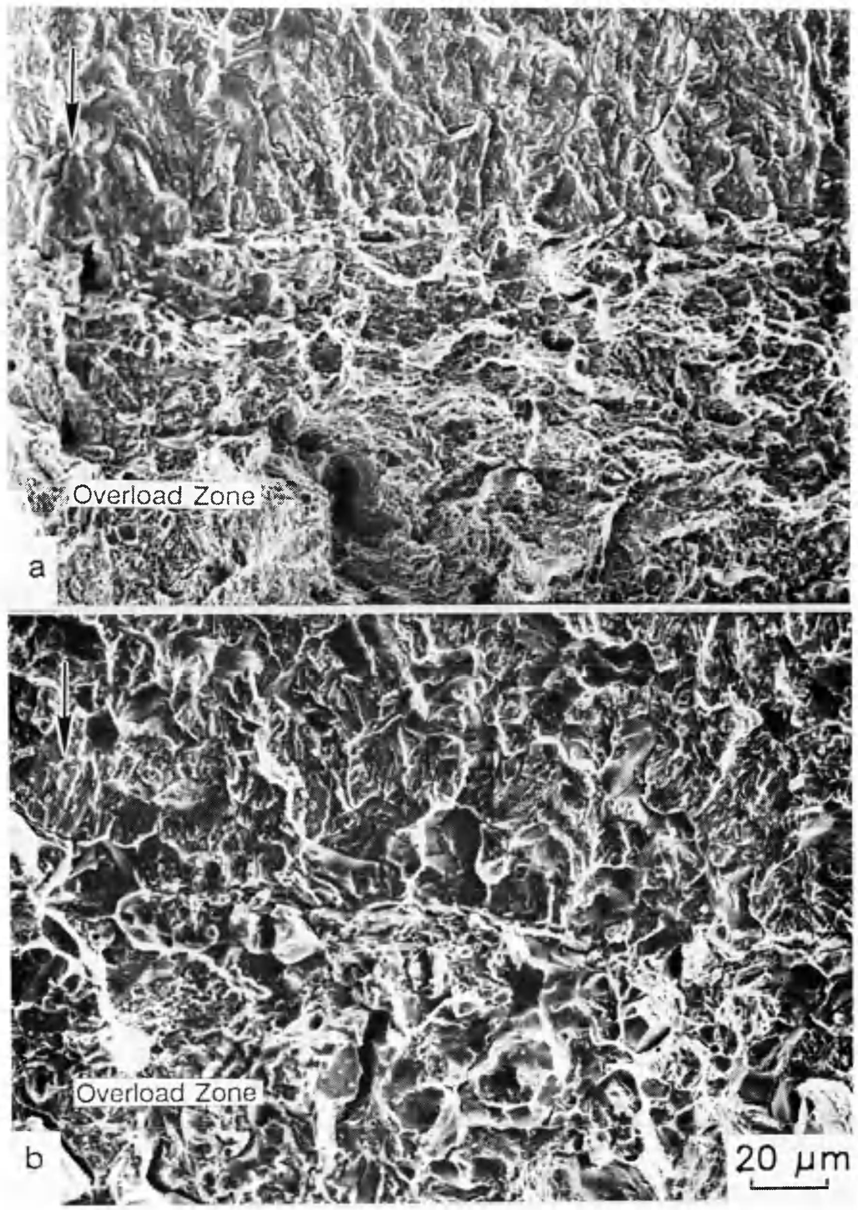

Figure 3.27 SEM micrographs of fracture surfaces of CT samples of 5160H steel tested at -26°C. a) low residual, b) high residual, 500X. Direction of crack propagation indicated by arrow.

of fracture. Again confirming a deterioration of mechanical properties in the high- residual material.

3.3 Effect of Tempering Conditions and Residual Content on the mechanical properties of 5160H steel

A summary and a correlation of the experimental results on the effect of tempering conditions, and of composition on fatigue and toughness of the material is presented. Fatigue properties of the material are not significantly affected by tempering temperature, post-tempering cooling rate, and residual alloy content, except at a tempering temperature of 500°C. At this tempering temperature the endurance limit is significantly reduced as the residual content increases. The air-cool post-tempering cooling rate further reduces such endurance limit of the high- residual material.

Transition temperature, upper shelf energy, and impact energy at room temperature are not affected by post-tempering cooling rate. These properties, however, are significantly affected by residual content. As the residual content increases, the transition temperature is shifted to higher temperatures, the upper shelf energy is reduced, and the the room-temperature impact energy is significantly reduced at tempering temperatures of of 304°C and 500°C. This reduction of impact toughness indicates embrittlement by TME and TE embrittling mechanisms. This embrittlement in the high-residual material indicates that diffusion of embrittling elements (as discussed in Sections 1.3.2 and 1.3.3) takes place in the material, and that temper embrittlement can take place on initial tempering, so that the term "non-embrittled steel" should be regarded as a relative and not as an absolute term (10).

Impact toughness values are not significantly affected by the post-tempering cooling rate. this agrees with observations in Section 1.3.1 in which it is stated that TE may be independent of cooling rate in some cases.

Fracture toughness values, taken at room temperature, can not be use to determine embrittlement in the steel. Development of a ductile transition zone during testing masks the real resistance of the material to crack propagation. Fracture toughness testing at subzero temperature, however, shows a significant reduction of K_{Ic} values as the residual content increases. This reduction of fracture toughness at subzero temperatures correlates well with the reduction of impact toughness.

This reduction in K_{Ic} with a decrease of temperature in the embrittled material implies a reduction of the critical crack size to cause final failure. This reduction of critical crack size, coupled with a possible increase of the crack growth rate, may contribute to the reduction of fatigue life of the high-residual material tempered at 500°C. This reduction of fatigue life of specimens tempered at 500°C may even be more significant if the samples were tested in fatigue at low temperatures. (It is important to point out that the effect of crack growth rate, in such a small section as the one of the fatigue sample, should not be as significant as the effect of the reduction of the critical crack length on the fatigue life of the sample).

There is then a general deterioration of mechanical properties of the high-residual material. Observations on the mechanical properties of this material suggests that such deterioration of mechanical properties is related to a temper embrittlement. Temper embrittlement is not evident in the low-residual steel. However, the important reduction of endurance limit of the low-residual material, when tempered at 500°C, may be related to TE.

Temper embrittlement has been shown to affect fatigue properties of a steel (15). There is no available information to explain the reduction of endurance limit in the low-residual material at 500°C. A hypothesis, mixing the effect of stress concentration at hard-surface particles with a segregation of embrittling elements to the particle-matrix interface, could be based on co-segregation of embrittling elements to the inclusion-matrix interface. An explanation could be as follows:

Embrittling elements are thought to segregate to interfaces in temper embrittled materials (18, 19, 20). Steel 5160H has shown to be susceptible to embrittlement; this susceptibility to temper embrittlement suggests that diffusion of such embrittling elements actually take place in this steel. The low-residual material does not show evidence of TE but the reduction of endurance limit in this material takes place at a tempering temperature (500°C) close to 550°C, the temperature at which maximum temper embrittlement develops in hardenable steels (10, 3, 11).

There is then a possibility that some embrittling elements segregate to inclusion-matrix interfaces during initial tempering at 500°C. This observation would agree with the concept stated previously on embrittlement developing during initial tempering, and on "non-embrittled material" being a relative and not an absolute term (10).

Thus, embrittled inclusion-matrix interfaces, in the presence of the stress concentration caused by the inclusion, lose coherency and produce free-surface regions where plastic deformation by dislocation motion (Section 1.4.1.1) can proceed. (Figure 3.15a shows a well defined inclusion-particle interface). This plastic deformation produces extrusions and intrusions, which in turn generates microcracks and eventually a fatigue crack will be formed (11, 33, 35). Thus, the presence of the embrittled interfaces reduces the number of cycles required to initiate a crack, thus reducing fatigue life.

Fracture surface appearances confirm a general deterioration of the mechanical properties of the material as the residual alloy content increases. Fatigue, impact, and fracture toughness samples of the high-residual material present a brittle type of fracture. However, the fracture surface appearance of samples tempered at 500°C do not correspond to the expected fracture mechanism in TE; instead the fracture mechanism is a mixture of the expected fracture mode in TME and TE. It appears then, that the material has generally been embrittled by the diffusion of embrittling elements to interfaces, and that the type of fracture is just a response of the specific material to the embrittlement. This observation would agree with a suggestion brought up by McMahon (15), in which it is proposed TME and TE to be a related phenomena, and not different embrittling mechanisms.

4 CONCLUSIONS

From the experimental data gathered in this thesis it can be concluded:

1- Susceptibility to temper embrittlement in thin-section 5160H steel increases as the residual alloy content increases.

2- Impact toughness and fracture toughness decrease with an increase in residual content.

3- Fatigue endurance limits in both the low-residual and the high-residual materials are significantly reduced when the material is tempered at 500°C. The magnitude of the reduction in the endurance limit is greater for the high-residual material.

4- The only effect of variation in post-tempering cooling rate was observed in the endurance limits for samples tempered at 500°C. When air cooling produced a greater reduction in endurance limit.

5- Optimal conditions of fatigue and fracture properties is obtained in 5160H steel by tempering at 426°C.

5 RECOMMENDATIONS

The combination of elements such as manganese, nickel and chromium enhances the susceptibility of the steel to TE in the presence of phosphorus and tin. Thus, reductions of nickel, phosphorus and tin contents below 0.058, 0.008, and 0.008, respectively, may improve properties of the material. Small additions of molybdenum (below 0.4%) may have the same effect as the reduction of residual content referred to above. In addition, development of small austenite grain sizes may also improve the properties of the material.

REFERENCES

1. G. Krauss, Principles of heat treatment of steel, 4th ed., American Society of Metals, 1987, pp. 212-219.

2. R.H. Greaves, "Temper-brittleness of nickel-chrome steels", ISI, No II, Vol. C, 1919, pp 329-347.

3. B.C. Woodfine, "Temper-Brittleness: a Critical Review Literature", JISI, Vol. 173, 1953, pp 229-240.

4. W. Steve, and Balajiva, "The Influence of Minor Elements on the Isothermal Embrittlement of Steels", JISI, Oct. 1959, pp141-147.

5. J.R. Low, Jr., "Temper Brittleness- A Review of Recent Work", in Fracture of Engineering Materials, American Society of Metals, 1964, pp. 127-142.

6. A.S. Heh, and W.C. Porr, "Effect of Cold Work on Temper Brittleness", Trans ASM, Vol 52, Apr. 1959, pp. 81-94.

7. W.F. Smith, Structure and Properties of engineering Alloys, McGraw-Hill, New York, NY, 1981.

8. V.V. Kalmykov, "Temper Embrittlement of Carbon Steels Containing Phosphorus and Arsenic", STAL, Feb. 1969, pp 152-155.

9. F.L. Carr, M. Goldman, et al., "Isothermal Temper Embrittlement of SAE 3140 Steel", Trans. AIME, Aug. 1953.

10. J.H. Hollomon, "Temper Brittleness", Trans ASM, Vol. 36, 1946. pp 473-541.

11. B.C. Woodfine, "Some Aspects of Temper-brittleness", JISI. Vol. 173, 1953, pp. 240-255.

12. J.M. Capus, "Austenite Grain Size and Temper-Brittleness", JISI, Nov. 1962, pp. 922-927.

13. H.L. Marcus, L.H. Hackett,jr., et al., "Effect of Solute Elements on Temper Ebrittlement of Low Alloy Steels", in Temper Embrittlement of Alloy Steels, ASTM STP 499, American Society for Testing and Materials, 1972, pp. 90-103

14. F.L. Carr, J. Nunes, and F.R. Larson, "Mechanical Properties and Fracture Surface Topography of a Thermally Embrittled Steel", in Temper Embrittlement in Steel, ASTM STP 407, American Society For Testing and Materials, 1968, pp. 203-236.

15. C.J. McMahon,jr., "Temper Brittleness- An Interpretative Review", in Temper Embrittlement in Steel, ASTM STP 407, American Society for Testing and Materials, 1968, pp. 127-167.

16. B.Z. Weiss, S. Niedzwiedz, and M. Breuer, "Influence of Temper Brittleness on Fatigue Properties and the Initiation and Propagation of Fatigue Cracks in Silicon Steels", JISI, Feb. 1966, pp. 152-156.

17. Z. Qu, and C.J. McMahon,jr., "The Effects of Tempering Reactions on Temper Embrittlement of Alloy Steels", Met. Trans. A, Vol. 14A, Jun. 1983, pp. 1101-1108.

18 A. Joshi, "Segregation at Selective Grain Boundaries and Its Role in Temper Embrittlement of Low Alloy Steels", Scripta Metallurgica, Vol. 9, 1975, pp. 251-260.

19. P.A. Restiano, and C.J. McMahon,jr., "The Role of Antimony in Temper Brittleness", Trans. ASM, Vol. 60, 1967, pp. 699-706.

20. T. Ando, and G. Krauss, "The Effect of Phosphorus Content on Grain Boundary Cementite Formation in AISI 52100 Steel", Met. Trans. A, Vol. 12A, Jul. 981, pp. 1283-1289

21. J. Yu, and C.J. McMahon,jr., "The effects of Composition and Carbide Precipitation on Temper Embrittlement of 2.25 Cr-1 Mo Steel: Part I and II. Effects of P, Sn, Mn, and Si", Met. Trans. A, Vol. 11a, Feb.1980, pp. 277-300.

22. J.R. Low,jr., et al., "Alloy and Impurity Effects on Temper Embrittlement of Steel", Trans AIME, Vol. 242, 1968, pp. 14.

23. J.M. Capus, "The Mechanism of Temper Britleness", in Temper Embrittlement in Steel, ASTM STP 407, American Society for Testing and Materials, 1968, pp. 3-19.

24. J. Kameda, and C.J. McMahon, "Solute Segregation and Brittle Fracture in an Alloy Steel", Met. Trans. A, Vol. 11A, Jan 1980, pp.91-101.

25. A. Joshi,and D.F. Stein, "Temper Embrittlement of Low Alloy Steels", in Temper Embrittlement of Alloy Steels, ASTM STP 499, American Society for Testing and Materials, 1972, pp. 59-89.

26. R. Viswanathan, and A. Joshi, "Effect of Microstructure on the Temper Embrittlement of Cr-Mo-V Steels", Met. Trans A, Vol 6A, Dec. 1975, pp. 2289-2297.

27. M. Guttmann, Dumoulin, and Wayman, "The Thermodynamics of Interactive Co-Segregation of Phosphorus and Alloying Elements in Iron and Temper-Brittle Steels", Met. Trans. A, Vol. 13A, 1982, pp. 1693-1710.

28. J. Barsom, and S. Rolfe, Fracture and Fatigue Control in Structures, 2nd Ed. Prentice-Hall Inc. Englewood Cliffs, NY, 1987.

29. R.F. Thomson, "Fatigue Behavior of High-Carbon High-Hardness Steels", Trans ASM, Vol. 56, 1963, pp. 803-833.

30. G. Dieter, Mechanical Metallurgy, McGraw-Hill, New York, NY, 1986.

31. H.O. Fuchs, and S.R. Stephens, Metal Fatigue in engineering, John Wily and Sons, 1980.

32. M.E Fine, "Fatigue Resistance of Metals", Met. Trans. A, Vol. 11A, March. 1980, pp. 365-379.

33. W.J. Plumbridge, and D.A. Ryder, "The Metallography of Fatigue", Metallurgical Reviews, Review 136 (The Metals and Metallurgy Trust),1969, pp. 119-142.

34. S.S. Manson, "Fatigue: A Complex Subject- Some Simple Approximations", Experimental Mechanics, Jul. 1965, pp. 193-226.

35. P.J. Forsyth, The Physical Basis of Metal Fatigue, Blackie, London, 1969.

36. H.K. Obermeyer, "The Effect of Phosphorus Content and Heat Treatment on the Fracture of 0.85% Carbon Steel", M.S. Thesis, Department of Metallurgical engineering, Colorado School of Mines, Golden, Colorado, Aug. 1978.

37. F. Borik, and R.D. Chapman, "The Effect of Microstructure on the Fatigue Strength of A High Carbon Steel", Trans. ASM, Vol. 53, 1961, pp. 447-463.

38. R.F Thomson, "Fatigue Behavior of High Carbon Steel High Hardness Steels", Trans. ASM, Vol. 56, 1963, pp. 802-833.

39. F. Borik. R.D. Chapman, and W.E. Jominy, "The Effect of Per Cent Tempered Martensite on Endurance Limit", Trans. ASM, Vol. 50, 1958, pp. 242-257.

40. T. Takemoto, K.L. Tsakalakos, ,et al., "The Importance of Surface Layer on Fatigue Behavior of a Ti-6Al-4V Alloy", Met. Trans. A, Vol. 14A, Jan. 1983, pp.127-132.

41. H.E. Frankel, J.A. Bennett and, W.A. Pennington, "Fatigue Properties of High Strength Steels", Trans. ASM, Vol 52, 1960, pp. 257-275.

42. V.M. Hauk, R.W. Oudelhoven, et al., "The State of Residual Stress in the Near Surface Region of Homogeneous and Heterogeneous Materials After Grinding", Met. Trans. A, Vol. 13A, Jul. 1982, pp. 1239-1244.

43. ASTM E23-86, Philadelphia, American Society for Testing and Materials, 1986.

44. ASTM E399-83, Philadelphia, American Society for Testing and Materials, 1983.

45. P.K. Poulose, "Determination of Fracture Toughness From Thin Side-Grooved Specimens", Engineering Fracture Mechanics, Vol. 26, 1987, pp. 203-211.

46. C.N. Freed, "Application of Side Grooves in the Determination of Fracture Toughness of High Strength Metals", in Fracture Toughness of High Strength Materials, Iron and Steel Institute, 1970, pp. 29-34.

47. F.J. Loss, et al., "Effect of Side Grooves on the R Curve: An Experimental View Point", Naval Research Laboratory, October 1980.

48. Private Communication, Pat Purtscher, NIST, 1989.

49. C.M. Carman, "Influence of Purity on the Fracture Properties of High Strength Aluminum, Titanium, and Steel", Met. Trans. A, PP. 116-127.

50. C.L. Cottrell, "Effect of Impurities on Fracture Toughness of High Strength Steel", Met. Trans. A, pp. 112-115.

51. Bethlehem Steel Corporation, Modern Steels and Their Properties, Bethlehem, PA, 1978.

52. D.I. Bron, I.I. Levites, and V.I. Pustovalov, "Effect of Tempering and Surface Condition on the Fatigue Strength of Steel 55S2", Translated From: Metallovedenie i Termiches-kaya Obrabotka Metallov, No 10, pp. 68-70. Oct. 1968.

53. J.P. Materkowski, and G. Krauss, "Tempered Martensite Embrittlement in SAE 4340 Steel", Met. Trans. A, Vol. 10A, Nov 1979, pp. 1643-1651.

54. J.P. Materkowski, "Tempered Martensite Embrittlement in 4340 Steels as Related to Phosphorus Content and Carbide Morphology", M.S. Thesis, Department of Metallurgical engineering, Colorado School of Mines, Golden, CO., Oct. 1978.

55. ASM, Metals Handbook, 8th ed., Vol. 10, American Society for Metals, Metals Park, Ohio, 1975.

56. ASM, Metals Handbook, 9th ed. Vol 11, American Society for Metals, Metals Park, Ohio, 1986.

57. K. Bruce, "The Effect of Chromium on the Microstructure and Bending Fatigue Behavior of 0.82% Carbon, 1,75% Nickel, and 0.57% Molybdenum Steels", M.S. Thesis, Department of Metallurgical engineering, Colorado school of Mines, Golden, Colorado, 1984.

58. B.J. Schulz, and C.J. McMahon,jr., "Alloy Effects in Temper Embrittlement", in Temper Embrittlement of Alloy Steels, ASTM STP 499, American Society for Testing and Materials, 1972, pp. 104-135.

APPENDIX A

S-N CURVES

Figures 1A through 7A show the cycles to failure as a function of maximum stress for tests performed with a constant minimum stress for all samples from the fatigue test program of 5160H steel. Data are presented for two levels of residual alloy content, and for the different tempering conditions described in table 2.2. In each figure, the curve reflects the fatigue behavior of the low-residual steel, for which extensive fatigue data was obtained. Also shown in each figure are the limited data obtained on the high-residual steel. The endurance limit is defined as the highest stress level at which samples did not fail, and sample survival is indicated by an horizontal arrow attached to data points where the tests were terminated.

A complete S-N curve was first obtained for samples tempered at 500°C in the water quenched condition (Figure 6A). From this S-N curve an endurance limit was determined and further fatigue testing for the other tempering conditions was performed at stress levels in the vicinity of this endurance limit.

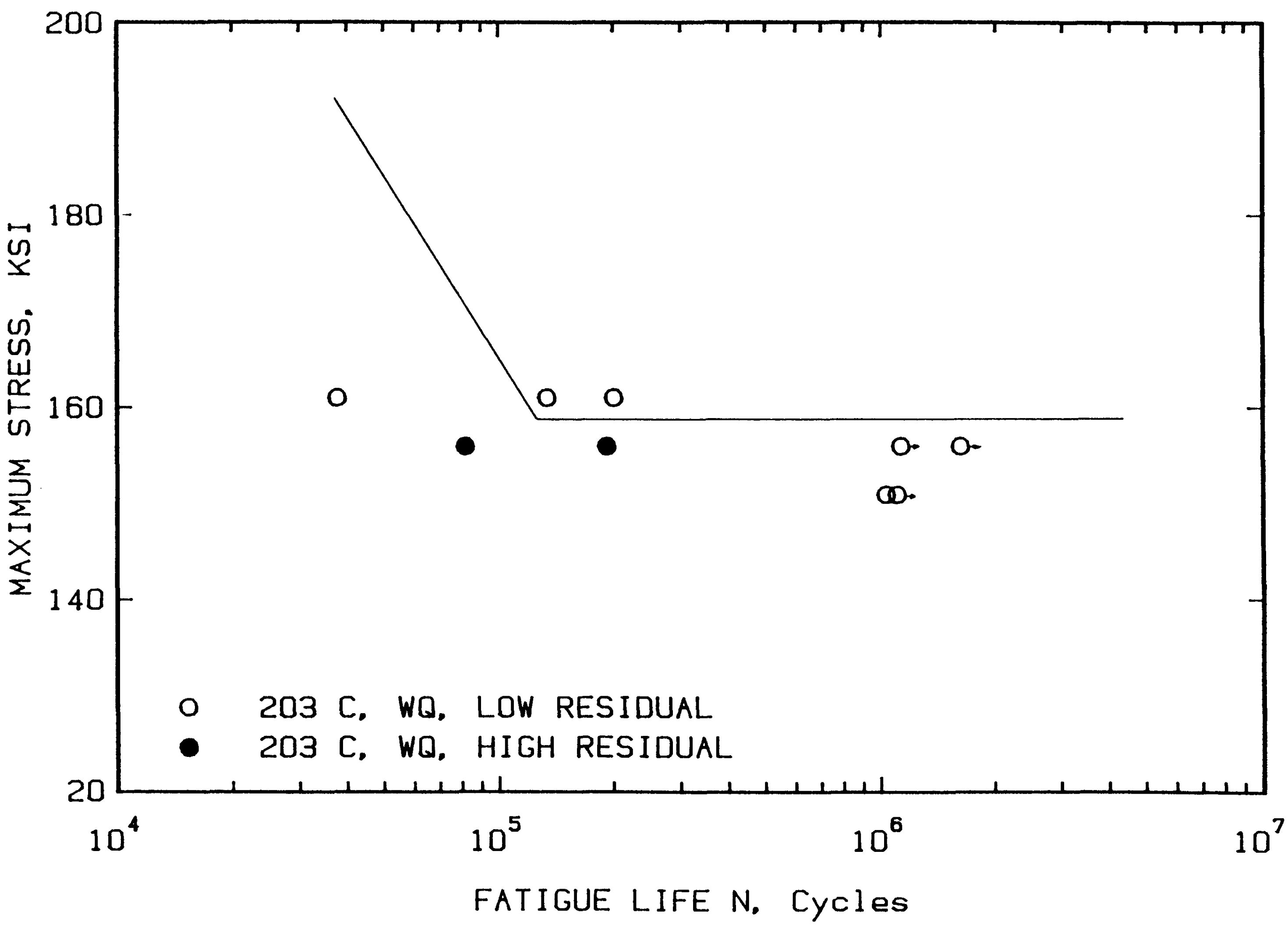

Figure A1 S-N curve for low- and high-residual 5160H steel water quenched after tempering at 203°C.

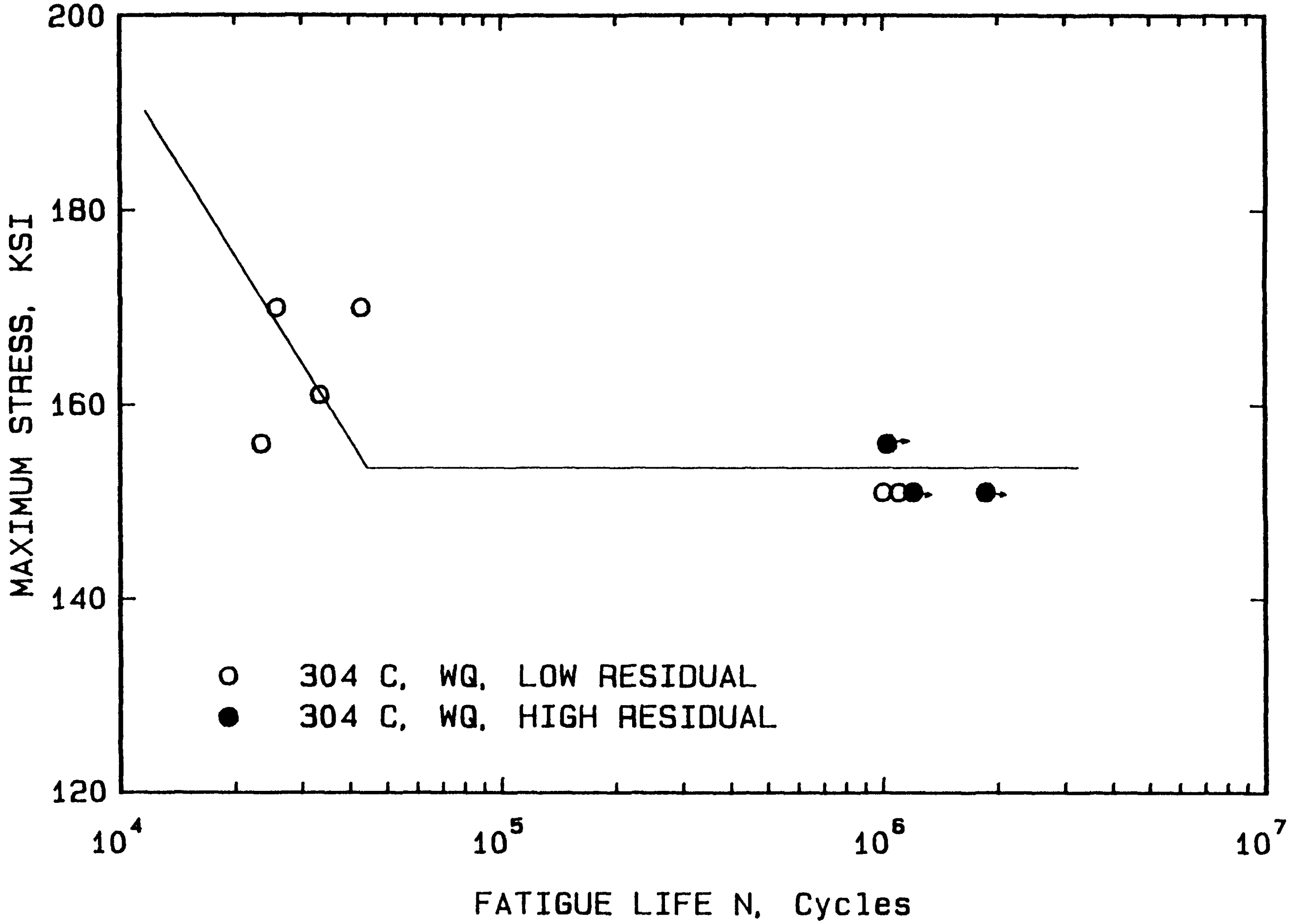

Figure A2 S-N curve for low- and high-residual 5160H steel water quenched after tempering at 304°C.

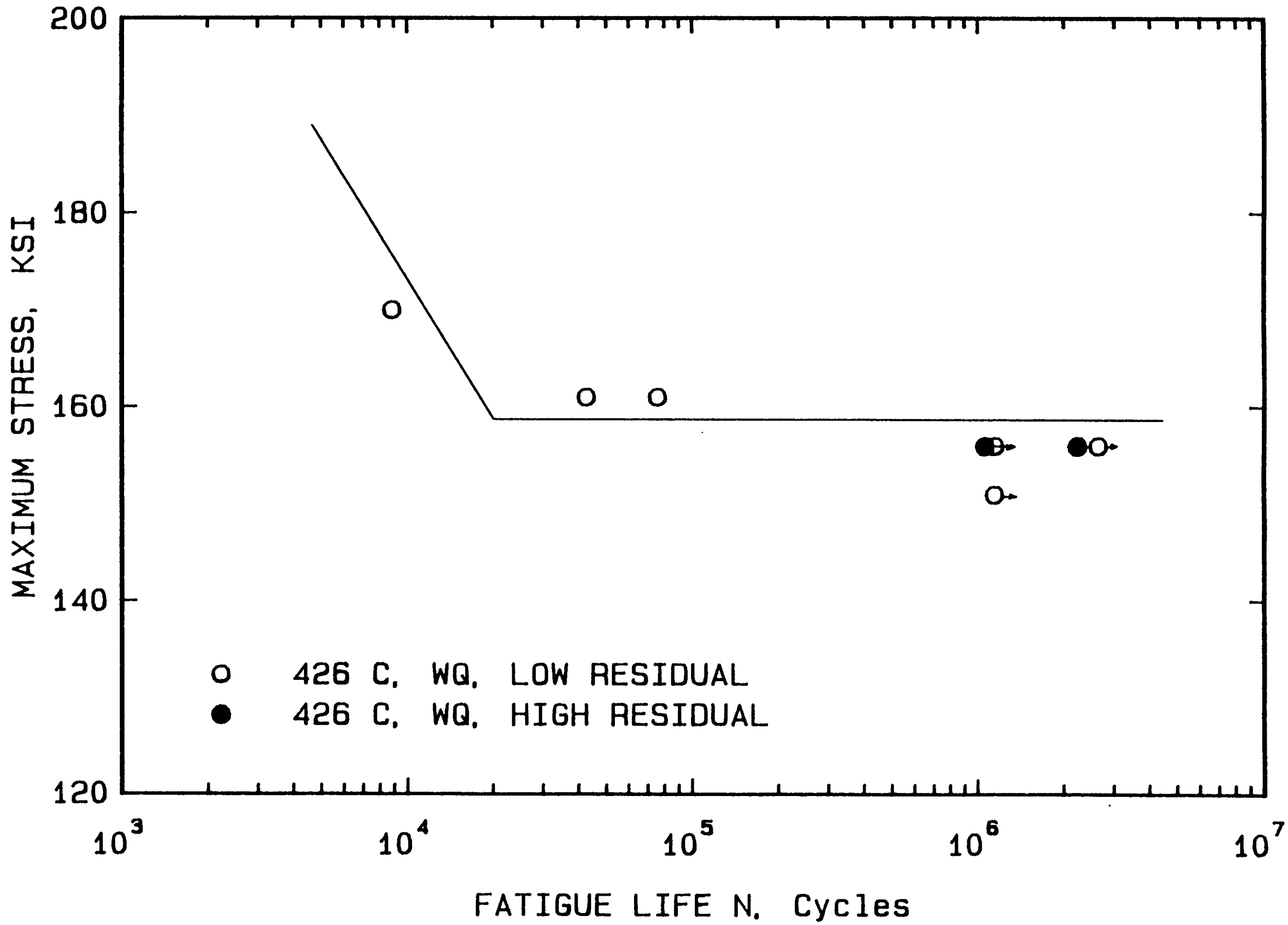

Figure A3   S-N curve for low- and high-residual 5160H steel water quenched after tempering at 426°C.

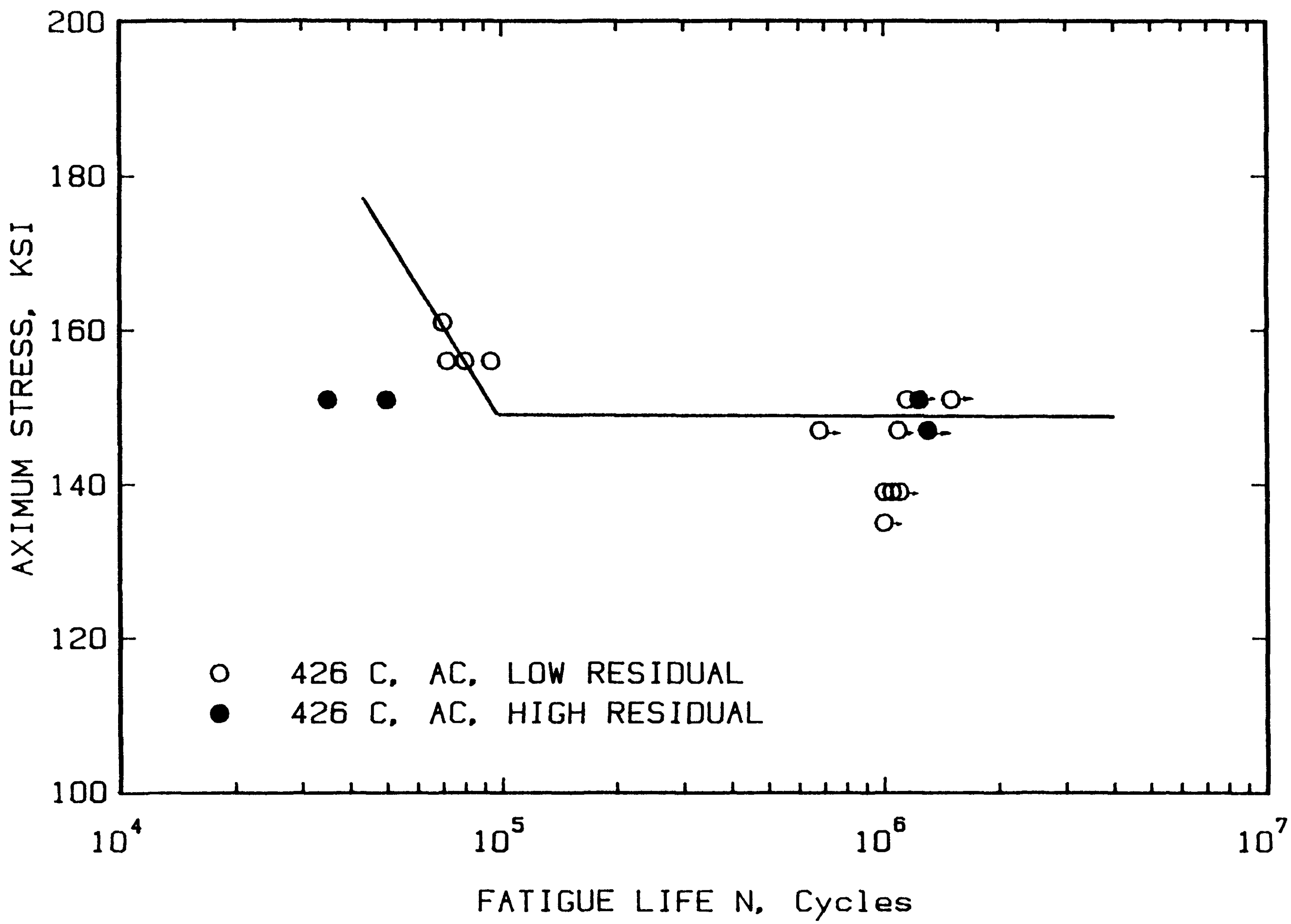

Figure A4 S-N curve for low- and high-residual 5160H steel air cooled after tempering at 426°C.

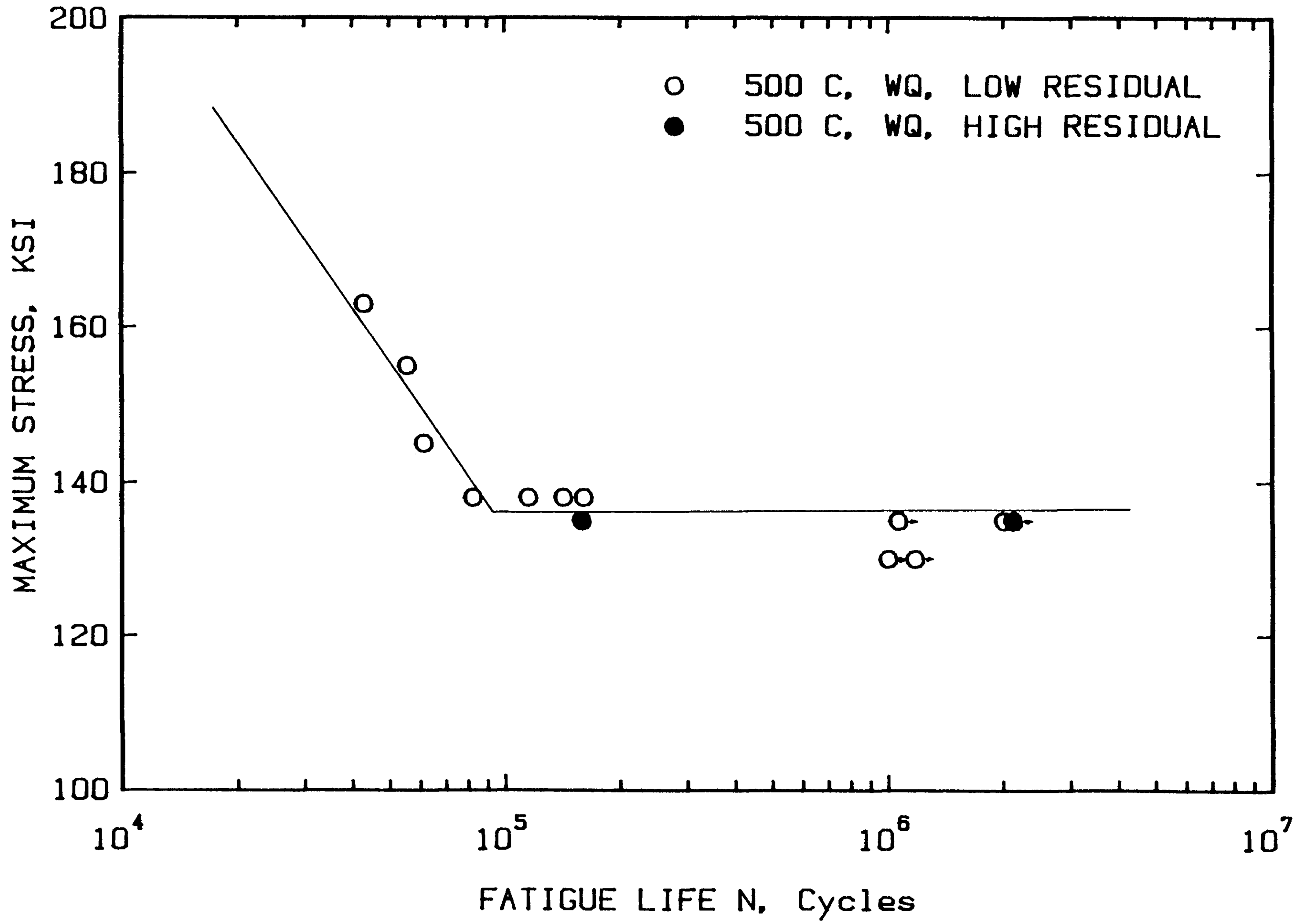

Figure A5 S-N curve for low- and high-residual 5160H steel water quenched after tempering at 500°C.

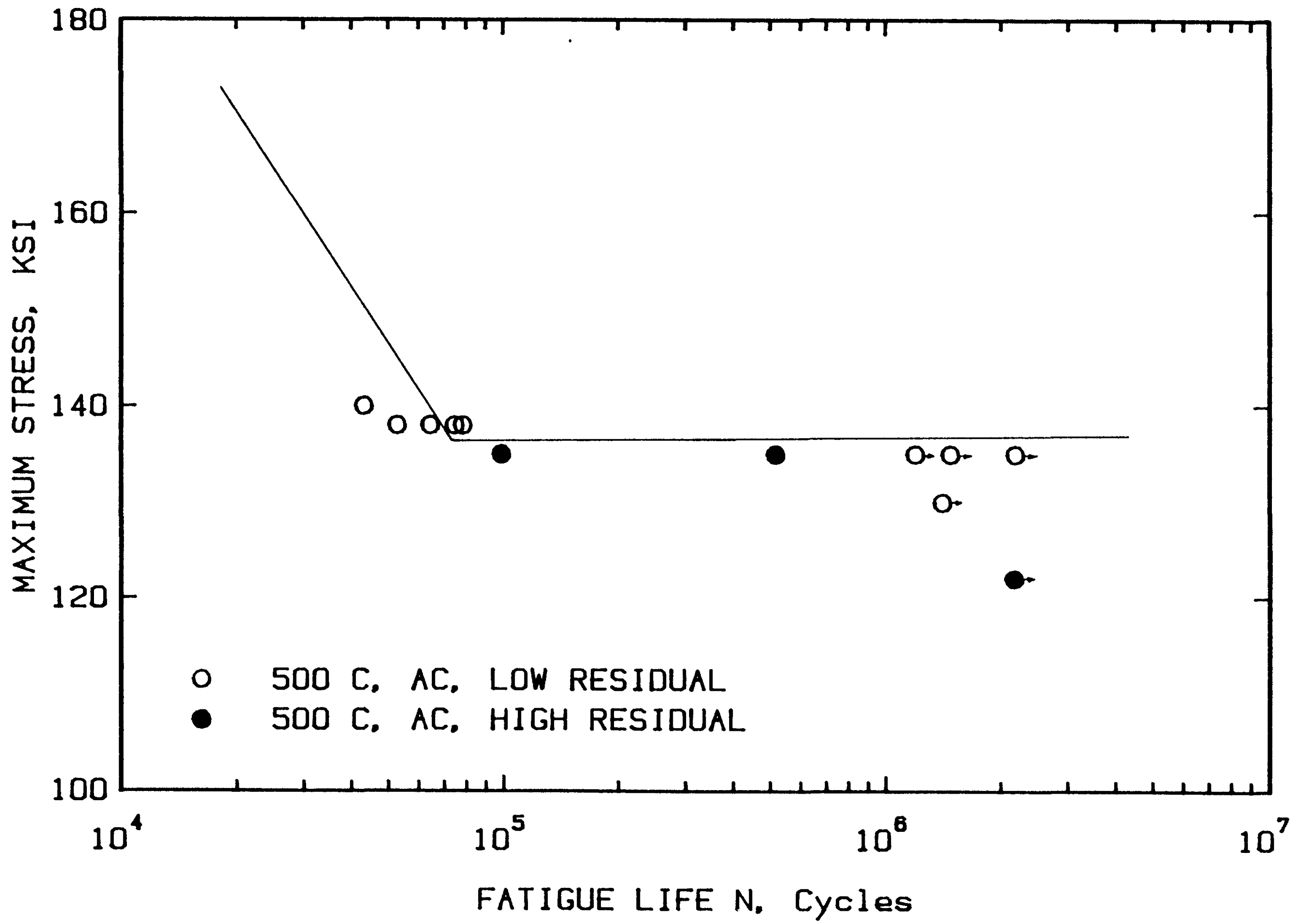

Figure A6 S-N curve for low- and high-residual 5160H steel air cooled after tempering at 500°C.

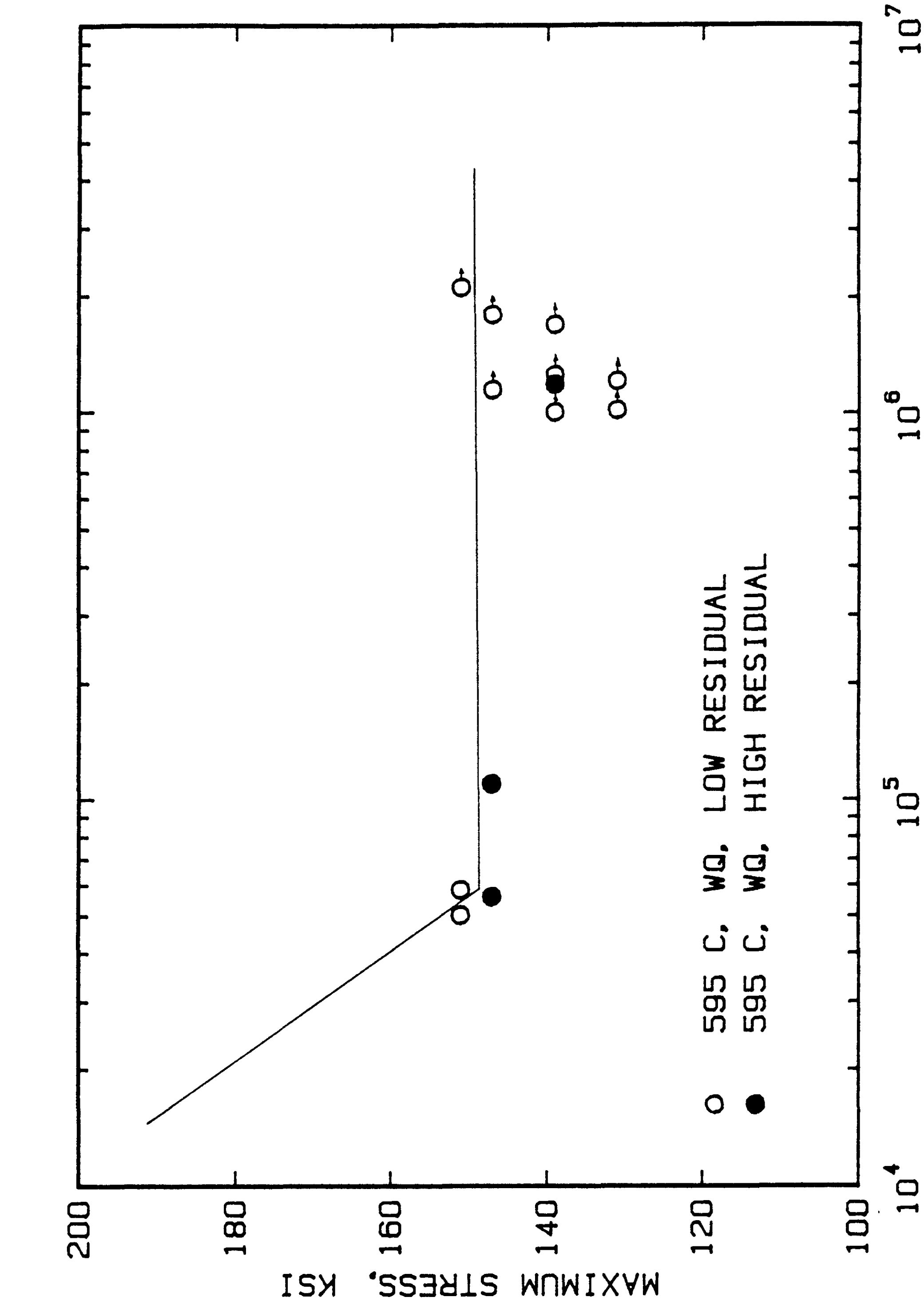

Figure A7 S-N curve for low- and high-residual 5160H steel water quenched after tempering at 595°C. It is also included fatigue data for the high-residual steel air cooled after tempering at 595°C.